Reconstructing the Behavior of Turbidity Currents From Turbidites-Reference to Anno Formation and Japan Trench

Zhirong Cai

Doctoral Thesis

Department of Geology and Mineralogy
Division of Earth and Planetary Sciences
Graduate School of Science
Kyoto University

2022

Abstract

Turbidity current has been a popular subject of study due to its contributions in carrying sediments from shallow to deep waters and the potential of its deposit, turbidite, as petroleum reservoir. Recently, turbidite as a record for mega-earthquakes and other geohazards made it a subject of interest in the field of hazard prevention. Despite its importance, observations of turbidites are limited to the partially exposed outcrops in the field and the drilling cores obtained from the ocean floor or on land. This study verifies and implements a novel deep neural network (DNN) inverse method that reconstructs the behavior of turbidity current from measurements of a turbidite at selected locations. The reconstructed turbidity current was then used to quantitatively reconstruct the unexposed region within the same turbidite. The DNN model implemented was first verified with five one-dimensional flume experiments. The reconstructed flow conditions and deposit profiles were compared with the measured ones to evaluate the performance of the DNN inverse method. The model performed well for the reconstruction of flume experiment datasets for deposit profiles, flow velocity, and flow height, but showed great deviation for flow concentration. The model was then applied to nine outcrop samples from a single turbidite bed in Anno Formation, Boso Peninsula, Chiba, Japan under a two-dimensional channel-basin setting, where the flow conditions and deposit characteristics in the basin were reconstructed. The total deposit thickness was reconstructed away from the channel with less than 0.10 m deviation from measured values, but close to the channel deviations went up to more than 0.20 m. The reconstructed peak flow velocity, flow depth, and total flow concentration were around 15 m, 15 m/s, 0.08, respectively. A preliminary test of the DNN model application to ar-

tificial core datasets from Japan Trench was conducted to explore the potential of DNN when applied to actual topographic data and core datasets. There had been no means of examining an entire turbidite deposited in nature due to limited exposure of outcrops. Instead of making inferences on the unexposed portion of ancient turbidites solely based on direct measurements of the exposed region, this study established a method directly reconstructing the flow behaviors and the entire distribution of turbidite deposits using a limited number of measurements from the exposed region.

Table of Contents

Chapter 1

Introduction

1.1 Introduction to Turbidity Currents

A turbidity current is a process of sediment transport into subaqueous environments such as deep lakes and oceans (Figure 1.1A) [*Daly*, 1936; *Johnson*, 1939]. Turbidites, the deposits of turbidity currents, are often characterized by graded bedding and sedimentary successions called the Bouma sequence [e.g., *Kuenen and Migliorini*, 1950; *Bouma*, 1962; *Talling et al.*, 2012]. Turbidites have been an active area of study due to their close association with petroleum resources and their role in the destruction of sea-floor equipment, such as submarine cables [*Weimer and Slatt*, 2007; *Talling et al.*, 2015]. Furthermore, turbidites are often deposited as a result of tsunami-triggered turbidity currents [*Arai et al.*, 2013; *Ikehara et al.*, 2016] and thus can contribute to determining the recurrence intervals of geohazards.

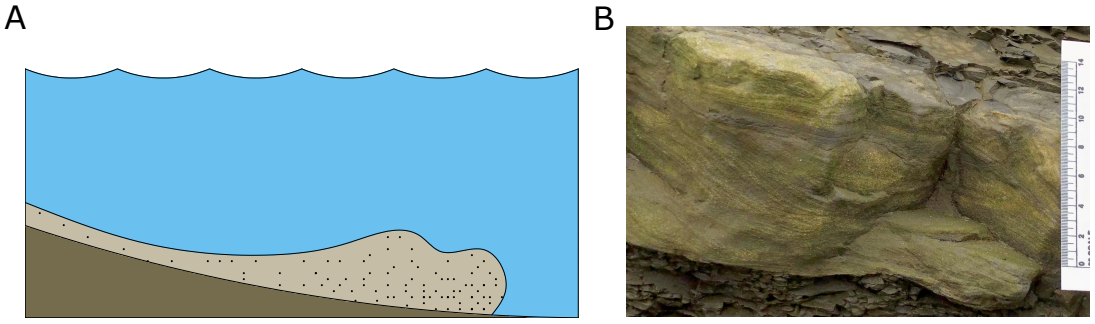

Figure 1.1: A. Schematic diagram of turbidity current. B. Outcrop photo of turbidite sandstone from the Akkeshi Formation of Nemuro Group, located in Hokkaido, Japan

The main methods for studying natural turbidites include field surveys and core drilling. During field surveys, ancient turbidites exposed in outcrops were observed (Figure 1.1B). Sedimentary structures were described, measured, and sampled for analysis. Core drilling involved cutting into the unexposed strata on land or underwater using a metal pipe. Long columnar samples of strata were collected for observation and measurements. The two methods provided a direct understanding of the characteristics of turbidites, but can only be conducted at limited locations within an entire turbidite due to very restricted exposure of deposits. To better understand a turbidite as a whole including the unexposed regions, understanding the flow behavior of turbidity currents and its relation to characteristics of turbidites were considered indispensable [*Talling et al.*, 2007].

The most straightforward method of examining the flow behavior of turbidity currents would be direct observation. Yet, studies in this area remain limited due to difficulties in the surveying of turbidity currents in nature [*Talling et al.*, 2013]. Several in-situ measurements have been conducted [e.g., *Xu et al.*, 2004; *Vangriesheim et al.*, 2009; *Arai et al.*, 2013; *Paull et al.*, 2018] and extensive research detailing the dynamics of the measured flows was conducted [e.g., *Chikita*, 1989; *Dorrell et al.*, 2016; *Azpiroz-Zabala et al.*, 2017a; *Heerema et al.*, 2020; *Simmons et al.*, 2020]. Especially well studied turbidity currents include the ones measured in the Congo Canyon offshore Congo in Africa and the Monterey Canyon offshore California, USA. At the Congo Canyon, measurements were conducted during a three-month period for two times, first from December 2009 to March 2010, and then from January to March 2013 [*Cooper et al.*, 2016]. Measurements were made at a single site with acoustic Doppler current profiler (ADCP) at 5 second intervals, the highest resolution dataset of direct turbidity current measurement as of now [*Azpiroz-Zabala et al.*, 2017b]. At the Monterey Canyon, the velocity structure of turbidity current was first measured with ADCP attached to moorings deployed at 1-hour intervals. The change in velocity structure over time was calculated and reported in *Xu et al.* [2004]. Measurements using ADCP at 30 s intervals were conducted at the Monterey Canyon in *Paull et al.* [2018], where

the flow structure of turbidity current was monitored between sites for over 50 km and their impact on the seafloor morphology was monitored for 18 months using more than 50 sensors deployed on the seafloor.

With detailed measurements conducted at Congo and Monterey Canyons, however, measurements of hydraulic conditions, such as sediment concentration, were difficult because of the destructive nature and unpredictable occurrences of turbidity currents [*Naruse and Olariu*, 2008; *Falcini et al.*, 2009; *Lesshafft et al.*, 2011; *Talling et al.*, 2015]. As indicated by *Xu et al.* [2004]; *Azpiroz-Zabala et al.* [2017b]; *Paull et al.* [2018], ADCP provides relatively reliable measurements of flow velocity structure but does not provide direct measurements of flow concentration. A rough estimate of flow concentration was conducted based on the flow velocity structures and other measurements and past experimental studies of turbidity currents [*Paull et al.*, 2018]. Recently, *Simmons et al.* [2020] proposed a novel acoustic method for measuring the concentration structure within submarine turbidity currents. The method was able to extract the sediment concentration data from ADCP measurements but did not perform well at high concentrations. The method also assumed a single grain-size class inflow, which is not consistent with the actual flow in nature.

Considering the instabilities indirect measurement of turbidity currents, alternatives such as flume experiments and numerical forward modeling became essential in exploring the flow behaviors of turbidity currents and characteristics of turbidites deposited. Flume experiments produce turbidites in different combinations of flow conditions of turbidity currents in a controlled laboratory setting. The flow conditions and characteristics of turbidites produced were examined and the relationship between the two is identified. Numerical forward modeling uses hydrodynamics-based mathematical calculations to reconstruct characteristics of turbidity currents and turbidites found in nature. A set of parameters characterizing the turbidity currents were usually adjusted to produce different types of flow and matching deposits numerically so that correlations between input flow parameters and deposit parameters can be explored. Methods such as flume experiments and numer-

ical modeling, where the change in deposit characteristics was examined by changing the flow conditions, were considered forward methods. In forward methods, relations between flow conditions and deposits identified by flume experiments or numerical modeling were applied to turbidites observed in outcrops or cores. Flow conditions of turbidity currents that deposited the observed stata were estimated, and the estimated flow conditions were used to infer the unexposed regions of the observed strata. Differing from forward methods, the reconstruction of flow conditions of turbidity currents directly from measurements of exposed turbidites in the field or core was called inverse modeling (Figure 1.2). The representative methods for understanding the dynamics of turbidity currents are briefly described in the following sections.

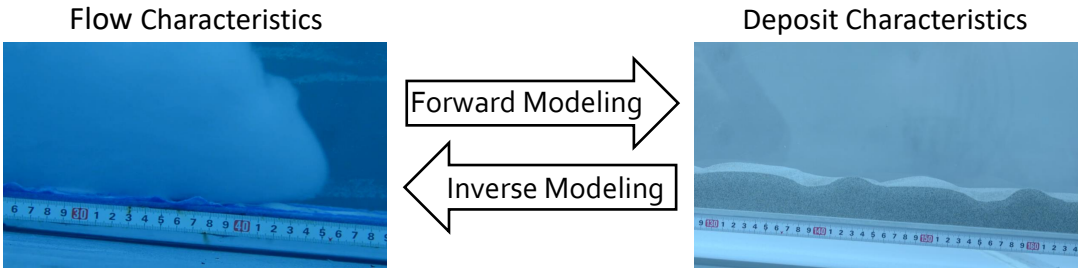

Figure 1.2: A diagram illustrating the general idea of forward and inverse modeling of turbidity currents using photos of turbidity current (left) and turbidite (right) from one-dimensional flume experiments.

1.2 Flume Experiment of Turbidity Currents

Flume experiments examining the mechanisms of sediment transport were first conducted in the early twentieth century [*Gilbert*, 1914] using water and sand of various sizes, where observations of change in bedforms with change in flow conditions were recorded. Into the mid-twentieth century, flume experiments incorporating hydraulics theories started to appear [*Kuenen and Migliorini*, 1950]. Experiments became scaled and the head and body

of turbidity currents were examined separately considering their differences in flow dynamics [*Middleton*, 1966a]. Turbidity currents with different properties were categorized and examined separately in flume experiments [*Bagnold*, 1954; *Middleton*, 1966b]. Attention was also given to saline flow, where experiments were conducted with saltwater and fine sediments such as fine silt and clay [*Einstein and Krone*, 1962; *Kuenen*, 1966]. The relationship between flow and deposit characteristics was discussed in multiple experimental studies using sand particles [*Kuenen and Migliorini*, 1950; *Kuenen and Menard*, 1952; *Riddell*, 1969; *Lüthi*, 1981; *Laval et al.*, 1988], which was sufficient for building the early models but was found to be too high in density for experimental scale flows. To solve the problem and produce more realistic flows in experiments, coal particles were used in flume experiments by *Garcia and Parker* [1991], which was soon substituted by plastic particles, a popular material used in flume experiments since the late twentieth century [*Garcia and Parker*, 1989; *Sequeiros et al.*, 2009].

To produce turbidite from turbidity currents in a laboratory setting, flume experiments of turbidity current were conducted by letting a dense mixture flow into a tank filled with fluid that is less dense than the incoming mixture. Water and particles with grain sizes ranging from sand to clay were the commonly used dense mixture in experiments. The ambient fluid in tank was usually water. For some experiments, salt was added to either the dense mixture [*Sequeiros et al.*, 2010] or the ambient fluid [*Einstein and Krone*, 1962; *Kuenen*, 1966] to increase the fluid density and facilitate suspension. Flume experiments for turbidity currents were conducted in both one-dimensional and two-dimensional settings, where flow propagates in a uniform direction downstream for one-dimensional and in a longitudinal and a lateral direction for two-dimensional settings.

In a one-dimensional experiment, the dense mixture was released into a flume that is thin in width and spanned a long distance from the upstream to the downstream direction (Figure 1.3A). The length of the tank was usually more than ten times the width. The thin width of the flume limited the sideway spreading of flow and direct it to flow in a straight

line from the upstream end to the downstream end, significantly reducing the complexity of measuring and analyzing the flow and deposits in comparison to two-dimensional experiments. The simplicity of one-dimensional experiments made them more accurately reproducible, a feature very important for testing certain controlled parameters and for verifying numerical models. Experimentally verified numerical model by *Parker et al.* [1987] was one of the most commonly used models for turbidity currents. Parameters related to sediment transport mechanisms, such as bedload and entrainment, were empirically determined from flume experiment datasets [*van Rijn*, 1984a,b; *Garcia and Parker*, 1993]

In a two-dimensional experiment, the dense mixture was released into a tank with similar width and length, where the flow can expand both downstream and in lateral directions (Figure 1.3B). Measuring and analysis were conducted in both downstream and sideways directions [*Imran et al.*, 2002; *Keevil et al.*, 2006; *Straub et al.*, 2008; *Rowland et al.*, 2010; *Abad et al.*, 2010; *de Leeuw et al.*, 2016; *Miramontes et al.*, 2020]. Two-dimensional experiments usually involve a more complex experimental setting and are very susceptible to the slight change in the experiment setting and surrounding environment, making their results be reproduced accurately. The complexity of Two-dimensional experiments was useful for examining the change in topography and depositional features but made them less useful in theoretical studies. For verification of a new inverse model, a one-dimensional flume experiment was chosen over the two-dimensional experiments for simplicity and more control over the flow and deposits created.

1.3 Numerical Experiments of Turbidity Currents

Numerical models based on fluid dynamics were used to simulate the behavior of fluids in many areas of study. The three-dimensional numerical experiments provide the most accurate illustrations of internal structures and dynamics of turbidity currents. *Cantero et al.* [2009] conducted a numerical experiment using the direct numerical simulation (DNS) on a

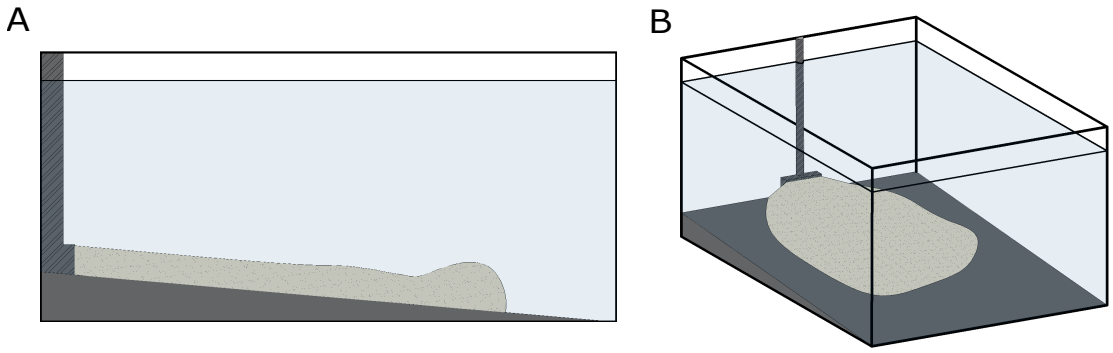

Figure 1.3: A. Schematic diagram of one-dimensional flume experiment. B. Schematic diagram of two-dimensional flume experiment.

self-stratified turbulent channel flow driven by suspended sediment, during which features such as self-stratification were precisely calculated and visualized. A particle to partial collision model that accounts for flow around particles and within pore spaces of sediment was implemented using DNS in *Biegert et al.* [2017], where the interaction between a particle and ambient water was examined in detail. The DNS models are great for modeling detailed movement within flow but were extremely high in calculation cost. The computational cost of DNS was scaled to Reynolds number cubed (Re^3), which limits the application of DNS to experimental scale flows [*Biegert et al.*, 2017]. Other more simplified three-dimensional models such as the Reynolds-averaged Navier-Stokes (RANS) model and the large eddy simulation (LES) model were lighter in terms of calculation load but too heavy for natural scale flow [*Yeh et al.*, 2013; *Meiburg et al.*, 2015; *Kneller et al.*, 2016]. Due to the calculation load problem of the three-dimensional models, the more simplified one or two-dimensional models based on the shallow-water equation, which is layer-averaged but accounts for sediment entrainment and settling, was the more popular choice of model for simulations of turbidity currents[e.g., *Parker et al.*, 1986]. Models more simple than the shallow-water models, such as the box model [*Huppert*, 1998], also exist, but an oversimplified model does not work well in capturing the flow characteristics of flow in nature. In this study, we chose to use a model based on the shallow-water equation for the balance be-

tween calculation load and the reasonable amount of details considered during calculation.

The most commonly used models for numerical simulations of turbidity currents based on the shallow-water model include the three-equation and four-equation models developed by *Parker et al.* [1986], who first constructed and experimentally verified a numerical model that can be directly applied to turbidity currents measured in experiments or the field. In a numerical simulation of a turbidity current, initiating conditions of flow were inputted into the numerical model. The model then calculated the time evolution of flow and deposit characteristics based on the initiating conditions. Same with flume experiments, numerical simulations of turbidity currents were conducted in one-dimensional [*Parker et al.*, 1986; *Choi and Garcia*, 1995; *Kostic and Parker*, 2006] and two-dimensional settings [*Choi*, 1999; *Lai et al.*, 2015].

A one-dimensional numerical model simulated a turbidity current that flows from the upstream to the downstream direction in a straight line. One-dimensional numerical models were much lighter in calculation load in comparison to two-dimensional models, making them useful for studies that require repetitive or large-scale calculations. They were often used in combination with flume experiments to explore the theoretical aspects of numerical models. The two-dimensional numerical model simulated flow in both the horizontal and the lateral directions (Figure 1.4). Two-dimensional models were high in calculation load, making large-scale or repetitive simulations difficult, but provided more insights into the effect of topographical settings.

Other than dimension, another important factor in the numerical simulation of turbidity current is the grain size of sediment. Uniform grain-size models use one representative grain size for all sediments in flow, while mixed grain-size models use multiple representative grain-size. Considering turbidity current in nature consists of a range of different sized sediments [*Dorrell and Hogg*, 2010; *Dorrell et al.*, 2011], mixed grain-size models better mimic the flow in nature. However, uniform grain-size models were more commonly used due to their simplicity and lighter calculation load [*Traer et al.*, 2018; *Pirmez and Im-*

ran, 2003]. Also, closure functions, which were often empirically determined from flume experiments, were rare for mixed grain-size models.

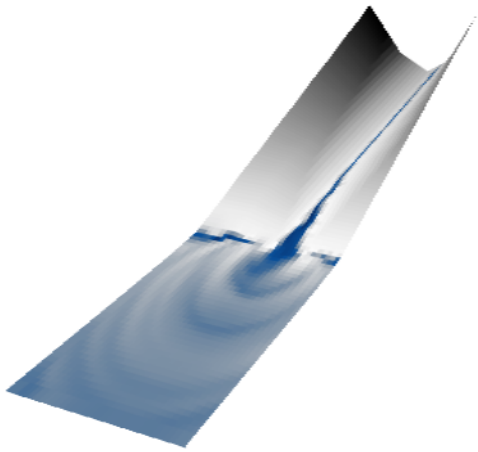

Figure 1.4: An example of two-dimensional numerical simulation of turbidity currents in a channel-basin setting with flow depth shown in blue.

1.4 Inverse Analysis of Turbidity Currents

In comparison to flume experiments and numerical simulations, the number of studies attempting inverse analysis of turbidity currents is relatively small. One of the earliest attempts was that of *Komar and Li* [1986], where grain entrainment threshold was reconstructed from grain size and shape. *Hiscott* [1994] tried to explore the relationship between flow velocity and the grain size of deposits using numerical calculation and then determine how the characteristics of deposit could be used to predict the state of the flow velocity. *Kubo et al.* [1998] attempted to reconstruct the spatial variation in paleocurrent structure from characteristics of turbidite beds. Into the twenty-first century, flow velocity was reconstructed through analyses of sedimentary structures of turbidites in *Baas et al.* [2000]. The results provided an estimation of the hydraulic conditions of flow at a single location but did not provide a reconstruction of the spatial evolution of the turbidity current. In contrast,

inverse analysis methods in previous studies based on numerical models provided more detailed insights into the spatial structure and evolution of flows over time [e.g., *Falcini et al.*, 2009; *Lesshafft et al.*, 2011; *Parkinson et al.*, 2017]. The method proposed by *Falcini et al.* [2009] assumed steady flow conditions and was simplified for obtaining analytical solutions, preventing it from accurately illustrating the flow mechanism of unsteady turbidity currents that can produce normally graded bedding. Consequently, this method cannot be applied to normally graded beds, which are typical characteristics of turbidites. Other studies used the optimization method, where the hydraulic parameters were determined by optimizing the input parameters of numerical models so that the resulting calculations were consistent with the observed data from turbidites [*Lesshafft et al.*, 2011]. This method can provide a relatively good reconstruction of the hydraulic conditions of turbidity currents but has an extremely heavy calculation load due to the complexity of the forward model employed and the repetitive calculation of the forward model for optimization. Therefore, applying the method to natural scale turbidites, which typically run over tens to hundreds of kilometers and flow continuously for several hours [*Talling et al.*, 2015], is impossible. Optimization using the adjoint approach proposed by *Parkinson et al.* [2017] solved the problem of heavy calculation load, but the reconstructed values differed from the expected values up to an order of magnitude.

Since previous methods to estimate flow conditions for turbidites were either overly simplified [*Baas et al.*, 2000], incapable of reproducing graded beds [*Falcini et al.*, 2009], accurate but computationally intractable for natural scale turbidity currents [*Lesshafft et al.*, 2011], or low in accuracy [*Parkinson et al.*, 2017], a method that is both accurate and not computationally intractable should be developed. To resolve the aforementioned issues, *Naruse and Nakao* [2021] proposed a new method for inverse analysis of turbidite deposits using deep learning neural networks (DNN). A DNN model is a machine-learning computing system that works as a universal function approximator [*Liang and Srikant*, 2016], meaning that an unknown function governing the relationship between observations within

a domain is explored and approximated. Previously, it was applied to problems such as landslide susceptibility analyses [*Pradhan et al.*, 2010] and identification of lithology from well log data [*Rogers et al.*, 1992], where the empirical relationship between the observed data and parameters aimed to be predicted was explored. In the case of turbidity currents, however, it is impossible to obtain sufficient datasets of in-situ measurements of flow characteristics for developing a DNN inverse model. Instead of using in-situ measurements of turbidity currents in nature, *Naruse and Nakao* [2021] generated numerical datasets of turbidites using a forward model. The generated datasets were input into a DNN model to explore the functional relationship between turbidites and initial flow conditions. After this network training process, the DNN model can estimate flow conditions from new turbidite data. *Naruse and Nakao* [2021] performed inverse analysis using a trained DNN model on field scale numerical test datasets generated by a forward model. Their results showed that the DNN model can reconstruct flow properties from numerical test datasets and was robust against noise in input data. The inverse model was applied to tsunami deposits in *Mitra et al.* [2020] and *Mitra et al.* [2021], where it proved efficient in reconstructing the inundation depth and depositional characteristics of the 2001 Tohoku-Oki tsunami and the 2004 Indian Ocean tsunami.

The DNN inverse model by *Naruse and Nakao* [2021] proved promising for exploring the flow behavior of turbidity currents. However, since a large amount of artificial dataset is needed for training the DNN inverse model, a forward numerical model that accurately illustrates the behavior of turbidity currents becomes essential for its application. Although the DNN model has demonstrated its performance on artificial datasets and with tsunami deposits, it has yet to be tested with turbidite data from flume experiments or in-situ measurements.

1.5 Objective of this study

The main objective of this study is to establish the methodology for reconstructing the behavior of turbidity currents from the deposited turbidites. In Chapter 2, the ability of the DNN inverse model in reconstructing flow behavior from turbidites was verified using one-dimensional flume experiments. The DNN inverse model was trained with artificial datasets produced by a one-dimensional numerical model and applied to turbidites deposited in flume experiments. In Chapter 3, the DNN inverse model alongside a two-dimensional numerical model was used to reconstruct the turbidity current flow behavior from outcrop datasets of the Anno Formation, Chiba, Japan. The DNN inverse model was trained with two-dimensional artificial outcrop datasets produced using an artificial topographical setting and was then applied to the actual outcrop data measured. In Chapter 4, the DNN inverse model and the two-dimensional numerical model were applied to artificial datasets of oceanic cores produced using actual topography data of Japan Trench and the surrounding area. The performance of the DNN model combined with a two-dimensional numerical model for reconstructing flow behavior of turbidity current from core data was examined. A synthesis and future prospect of numerical forward and inverse models conclude this thesis in Chapter 5.

Chapter 2

One-Dimensional Experimental Verification of the DNN Inverse Model

Abstract

Despite the importance of turbidity currents in environmental and resource geology, their flow conditions and mechanisms are not well understood. This study proposes and verifies a novel method for the inverse analysis of turbidity currents using a deep learning neural network (DNN) with numerical and flume experiment datasets. Numerical datasets of turbidites were generated with a forward model. Then, the DNN model was trained to find the functional relationship between flow conditions and turbidites by processing the numerical datasets. The performance of the trained DNN model was evaluated with 2000 numerical test datasets and 5 experiment datasets. Inverse analysis results on numerical test datasets indicated that flow conditions can be reconstructed from depositional characteristics of turbidites. For experimental turbidites, spatial distributions of grain size and thickness were consistent with the sample values. Concerning hydraulic conditions, flow depth, layer-averaged velocity, and flow duration were reconstructed with a certain level of deviation. The reconstructed flow depth and duration had percent errors less than 36.0% except for one experiment, which had an error of 193% in flow duration. The flow velocity was reconstructed with percent errors 2.38-73.7%. Greater discrepancies between the measured and reconstructed values of flow concentration (1.79-300%) were observed rela-

tive to the former three parameters, which may be attributed to difficulties in measuring the flow concentration during experiments. Although the DNN model did not provide perfect reconstruction, it proved to be a significant advance for the inverse analysis of turbidity currents.

2.1 Introduction

In *Naruse and Nakao* [2021], a DNN inverse model was developed and its performance on numerical datasets was demonstrated. However, it has has yet to be tested with turbidite data from experiments or in-situ measurements. In this chapter, the ability of the DNN model to perform inverse analysis of turbidity currents was verified by applying it to data collected from turbidites deposited in flume experiments. The DNN inverse model was first tested on flume experiments instead of field data, because turbidity currents were generated in a controlled environment during flume experiments. Conditions, including flow duration and initial hydraulic conditions, can be set manually, and measurements of these parameters can also be conducted easily during experiments.

Here, a one-dimensional forward model and a DNN inverse model was implemented. The forward model was implemented with the same governing equations as *Naruse and Nakao* [2021], but the numerical scheme and closure equations were modified to accommodate experimental scale simulations and improve the accuracy of the calculation. The DNN model was trained with the experimental scale numerical datasets. The trained DNN model was first tested with independent sets of numerical datasets that were also produced by the forward model. Then, the trained DNN model was tested with flume experiment data. Initial flow conditions of experiments were reconstructed from sampled deposits. These flow conditions were then fed into the forward model to reconstruct the spatio-temporal evolution of the experiment. Reconstructed hydraulic conditions during the flow and grain size distribution of the deposits were compared with the measured values.

2.2 Forward Model

2.2.1 Governing Equations

The forward model implemented in this study is a layer-averaged shallow water model based on *Kostic and Parker* [2006]. It is expanded to account for the transport and deposition of non-uniform grain size distribution discretized to multiple grain-size classes in *Nakao et al.* [2020] (Figure 2.1). This model was chosen because it is sufficiently complex to some details of the internal structure of flow, but also contains simplifications that make its calculation cost reasonable. The five governing equations are as follows:

$$\frac{\partial H}{\partial t} + U\frac{\partial H}{\partial x} = e_{\mathrm{w}}U - H\frac{\partial U}{\partial x}, \tag{2.1}$$

$$\frac{\partial U}{\partial t} + U\frac{\partial U}{\partial x} = RC_{\mathrm{T}}g\left(\sin\theta - \cos\theta\frac{\partial H}{\partial x}\right) - \frac{1}{2}gHR\cos\theta\frac{\partial C_{\mathrm{T}}}{\partial x} - \frac{U^2}{H}(c_{\mathrm{f}} - e_{\mathrm{w}}), \tag{2.2}$$

$$\frac{\partial C_i}{\partial t} + U\frac{\partial C_i}{\partial x} = \frac{w_i}{H}(F_i e_{\mathrm{s}i} - r_{\mathrm{o}}C_i) - \frac{e_{\mathrm{w}}C_i U}{H}, \tag{2.3}$$

$$\frac{\partial \eta_i}{\partial t} = \frac{w_i}{1-\lambda_{\mathrm{p}}}(r_{\mathrm{o}}C_i - e_{\mathrm{s}i}F_i), \tag{2.4}$$

$$\frac{\partial F_i}{\partial t} + \frac{F_i}{L_{\mathrm{a}}}\frac{\partial \eta_{\mathrm{T}}}{\partial t} = \frac{w_i}{L_{\mathrm{a}}(1-\lambda_{\mathrm{p}})}(r_{\mathrm{o}}C_i - e_{\mathrm{s}i}F_i), \tag{2.5}$$

where the equations represent fluid mass conservation (equation 2.1), momentum conservation (equation 2.2), sediment mass conservation (equation 2.3), mass conservation in bed (Exner's equation) (equation 2.4), and sediment mass conservation in active layer (equation 2.5) [*Nakao et al.*, 2020].

Let x and t be the bed-attached streamwise coordinate and time, respectively. Parameters H, U, and C_i represent the flow depth, the layer-averaged velocity, and the layer-averaged volumetric concentration of suspended sediment of the ith grain-size class, respectively. Parameter C_{T} denotes the layer-averaged total concentration of suspended sediment ($C_{\mathrm{T}} = \sum C_i$), and g represents gravitational acceleration. Parameter c_{f} is the friction coefficient. Parameter θ is the angle of inclination of the base slope. Sediment properties

are described by R, the submerged specific density of sediment; w_i represents the settling velocity of a sediment particle of the ith grain-size class; λ_p represents the porosity of bed sediment. Parameter η_i is the volume per unit area of bed sediment of the ith grain-size class, and η_T is the sum of all η_i ($\eta_\mathrm{T} = \sum \eta_i$). Parameter L_a represents the active layer thickness, and F_i represents the volume fraction of the ith grain-size class in active layer. Parameters $e_{\mathrm{s}i}$, e_w, and r_o represent the entrainment rate of sediment of the ith grain-size class into suspension, the entrainment rate of ambient water to flow, and the ratio of near-bed suspended sediment concentration to the layer-averaged concentration of suspended sediment, respectively (Figure 2.1).

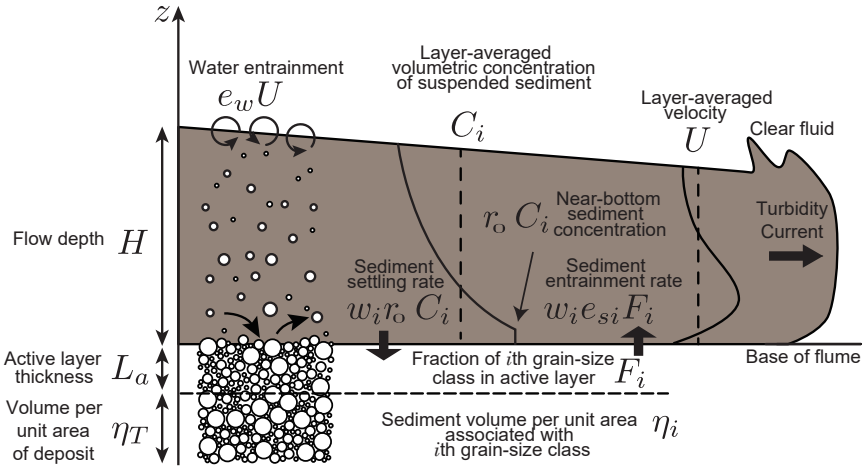

Figure 2.1: Schematic diagram of processes considered in the forward model from *Nakao et al.* [2020].

2.2.2 Closure Equations

Empirical formulations from previous studies are adapted to close the governing equations. In this study, the friction coefficient c_f is assumed to be a constant value. The particle settling velocity w_i for each grain-size class with representative grain diameter D_i is calculated

using the relation from *Dietrich* [1982], which can be expressed as follows:

$$w_i = R_{\mathrm{f}i}\sqrt{RgD_i}, \tag{2.6}$$

$$R_{\mathrm{f}i} = \exp\{-b_1 + b_2\log(Re_{\mathrm{p}i}) - b_3[\log(Re_{\mathrm{p}i})]^2 - b_4[\log(Re_{\mathrm{p}i})]^3 + b_5[\log(Re_{\mathrm{p}i})]^4\}, \tag{2.7}$$

$$Re_{\mathrm{p}i} = \frac{\sqrt{RgD_i}D_i}{\nu}, \tag{2.8}$$

where b_1, b_2, b_3, b_4 and b_5 are 2.891394, 0.95296, 0.056835, 0,000245 and 0.000245, respectively. e_{w} is calculated using the empirical formula from *Fukushima et al.* [1985] as follows:

$$e_{\mathrm{w}} = \frac{0.00153}{0.0204 + Ri}, \tag{2.9}$$

with Ri, the bulk Richardson number, defined as:

$$Ri = \frac{RgC_{\mathrm{T}}H}{U^2}. \tag{2.10}$$

The entrainment coefficient of sediment $e_{\mathrm{s}i}$ is calculated using the empirical relation from *Garcia and Parker* [1993]:

$$e_{\mathrm{s}i} = \frac{aZ^5}{1 + (\frac{a}{0.3})Z^5}, \tag{2.11}$$

$$Z = \alpha_1 \frac{u_*}{w_i} Re_{\mathrm{p}i}^{\alpha_2}, \tag{2.12}$$

where shear velocity u_* is calculated as follows:

$$u_* = \sqrt{c_{\mathrm{f}}}U, \tag{2.13}$$

and the constants α_1 and α_2 are 0.586 and 1.23 respectively if $Re_{\mathrm{p}} \leq 2.36$. If $Re_{\mathrm{p}} > 2.36$, α_1 and α_2 are 1.0 and 0.6, respectively. Constant a is 1.3×10^{-7}. Kinematic viscosity of water ν is calculated as follows:

$$\nu = \mu/\rho, \tag{2.14}$$

where ρ and μ denote water density and dynamic viscosity, respectively.

2.2.3 Implementation of Forward Model

In this study, the constrained interpolation profile (CIP) method [*Yabe et al.*, 2001] implemented with staggered grid was used for integrating of the partial differential equations 2.1, 2.2, and 2.3. The stability condition of the CIP scheme is as follows [*Gunawan*, 2015]:

$$1 \quad > \quad \frac{\Delta t \max(|U| + \sqrt{gH})}{\Delta x}. \tag{2.15}$$

The time step Δt was fixed to a value of 0.01 s so that it does not violate the stability condition. The CIP scheme implemented was of third order accuracy. Although this numerical scheme is not strictly mass-conservative, the volume loss of this method has been verified to be less than 0.07% when tested with a simple numerical wave tank (NWT), acceptable for fluid simulation [*Vestbøstad et al.*, 2007]. To stabilize the calculation, artificial viscosity was used with the scheme of *Jameson et al.* [1981], where the parameter κ was set to 0.25. The two-step Adams predictor-corrector method, which was more stable than the ordinary Euler's method, was used to solve ordinary differential equations 2.4 and 2.5. Interval of spatial grids Δx was set to 0.05 m based on experimental settings (Section 2.4.1). The model was tested with different mesh sizes ranging from one fifth to five times the current mesh size and was confirmed to be mesh independent. Initial values of θ for all grids were set to the same value as the base slope of experimental setups.

The Dirichlet boundary condition was used for the upstream boundary, where all flow parameters at the upper boundary of the calculation domain, including the initial flow depth H_0, the initial flow velocity U_0, the initial total volumetric concentration of sediment $C_{\mathrm{T},0}$, and the initial volumetric concentration of each grain-size class $C_{i,0}$, were set to be constant. Parameter $F_{i,0}$, the initial volume fraction of the ith grain-size class in active layer, was set to 1/N for all grain-size classes, where N represents the number of grain-size classes. The downstream boundary was the Neumann boundary condition in which all parameters

were set to the same values as those of the grid adjacent to the lower boundary toward the upstream direction. Other than the upstream boundary, all flow parameters were initialized to zero. The wet-dry boundary condition at the head of the flow was conducted using the scheme proposed by *Yang et al.* [2016]. A threshold value of $C_{\mathrm{T}}H$, ε, was used to determine the position of the waterfront. If $C_{\mathrm{T}}H < \varepsilon$, the grid was dry. If $C_{\mathrm{T}}H \geq \varepsilon$, the grid was wet. In this study, ε was set to 0.000001. A dry grid adjacent and downstream to a wet grids was a partial wet grid. Flow discharge M at a partial wet grid j was calculated using Homma's equation [*Yang et al.*, 2016] as follows:

$$M = C_{\mathrm{s}} H_{j-1} \sqrt{RgC_{\mathrm{T},j-1} H_{j-1}}, \tag{2.16}$$

where C_s, the discharge coefficient, is equal to 0.35.

The number of grain-size classes and representative grain diameter D_i for each grain-size class were determined on the basis of the grain size distribution in each experiment. For this study, the number of grain-size classes was set to 4 and D_i of grain-size classes 1, 2, 3, and 4 were 210, 149, 105, and 74.3 μm, respectively. The density of the surrounding fluid ρ_{f} was set to 1000.0 kg/m^3 in this study, since experiments were conducted with water. Dynamic viscosity μ was 0.00101 Pa·s, an experimentally determined of μ at 20.0°C [*Rumble*, 2018]. The submerged specific density of sediment $R = (\rho_{\mathrm{s}} - \rho_{\mathrm{f}})/\rho_{\mathrm{f}}$ was set according to the type of particles used in experiments. The density of sediment particles ρ_{s} for this study was 1.45 g/cm^3. The porosity of bed sediment λ_{p} was assumed to be 0.4. In this study, both the friction coefficient c_{f} and ratio of near-bed concentration to layer-averaged values r_{o} were assumed to be constant. c_{f} was set to 0.004. r_{o} was set to 1.5 [*Kostic and Parker*, 2006]. In addition, the thickness of active layer L_{a} was set to be a constant, 0.003 m [*Arai et al.*, 2013]. The gravitational acceleration g was 9.81 m/s^2.

2.2.4 Example of Forward Model Calculation

The forward model was tested with two sets of numerical simulations of turbidity currents. Testing was conducted using the forward model programmed for generating numerical datasets for experiments conducted with a 10% slope. The settings of the numerical simulations are listed in Table 2.1, whereas the time evolution of the high $C_{T,0}$, U_0 simulation is shown in Figure 2.2, and the time evolution of the low $C_{T,0}$, U_0 simulation is shown in Figure 2.3. In both cases, the flow depth H was greater toward the head of the current. H at the head of the current also increased over time (Figures 2.2A and 2.3A). Flow velocity U in the high $C_{T,0}$, U_0 simulation increased toward the head of the current(Figure 2.2B), whereas U in the low $C_{T,0}$, U_0 simulation increased initially, and then decreased toward the head of the current (Figure 2.3B). The total volumetric concentration of sediment C_T in flow decreased downstream in both cases (Figures 2.2C and 2.3C). In the high $C_{T,0}$, U_0 case, a larger portion of sediment was deposited downstream than in the low $C_{T,0}$, U_0 case (Figures 2.2D and 2.3D). The low $C_{T,0}$, U_0 case had the most sediment deposited toward the upstream end of the flow.

For the both high and low $C_{T,0}$, U_0 simulations, a thicker deposit was observed for grain-size classes 1 and 2 than for grain-size classes 3 and 4 (Figures 2.2E, G, H and 2.3E, G, H). Although the initial concentrations of the finer grain-size classes 3 and 4 $C_{3,0}$, $C_{4,0}$ were higher than that of the coarser grain-size class 1 ($C_{1,0}$), less fine sediment was deposited since it was more likely to remain suspended and be carried beyond the lower flow boundary by the high-velocity flow. For the low $C_{T,0}$, U_0 simulation, the coarser grain-size class, grain-size classes 1 and 2, had almost all sediment deposited near the upstream boundary, whereas the finer grain-size class, grain-size classes 3 and 4, had sediment spread out toward the downstream direction (Figures 2.3E, F, G, H). This happened because the low-velocity flow was unable to keep the coarse sediment suspended.

Table 2.1: Initial flow conditions of numerical simulations of turbidity currents.

	High $C_{\mathrm{T},0}$, U_0	Low $C_{\mathrm{T},0}$, U_0
H_0 (m)	0.15	0.15
U_0 (m/s)	0.2	0.02
$C_{\mathrm{T},0}$	0.018	0.001
$C_{1,0}$	0.004	0.0002
$C_{2,0}$	0.005	0.0003
$C_{3,0}$	0.0047	0.00027
$C_{4,0}$	0.0043	0.00023
c_{f}	0.004	0.004
r_{o}	1.5	1.5
Duration (s)	420	420

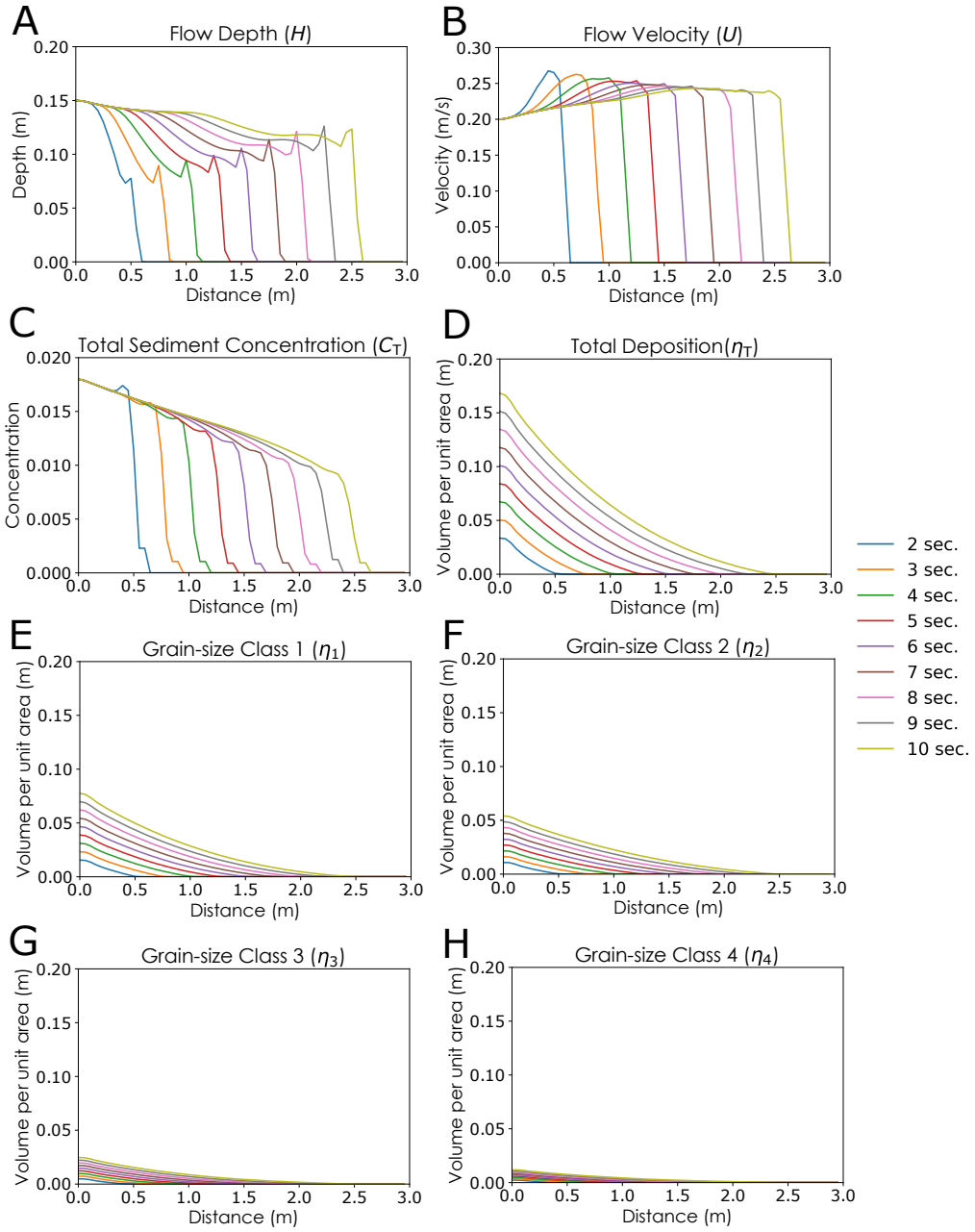

Figure 2.2: Example of forward model calculation with high initial flow velocity and sediment concentration (Table 2.1). A. Time evolution of flow depth H. B. Time evolution of flow velocity U. C. Time evolution of total sediment volumetric concentration C_{T}. D. Time evolution of deposit profile η_{T}. E. Time evolution deposit profile of grain-size class 1 η_1. F. Time evolution of deposit profile of grain-size class 2 η_2. G. Time evolution of deposit profile of grain-size class 3 η_3. H. Time evolution of deposit profile of grain-size class 4 η_4.

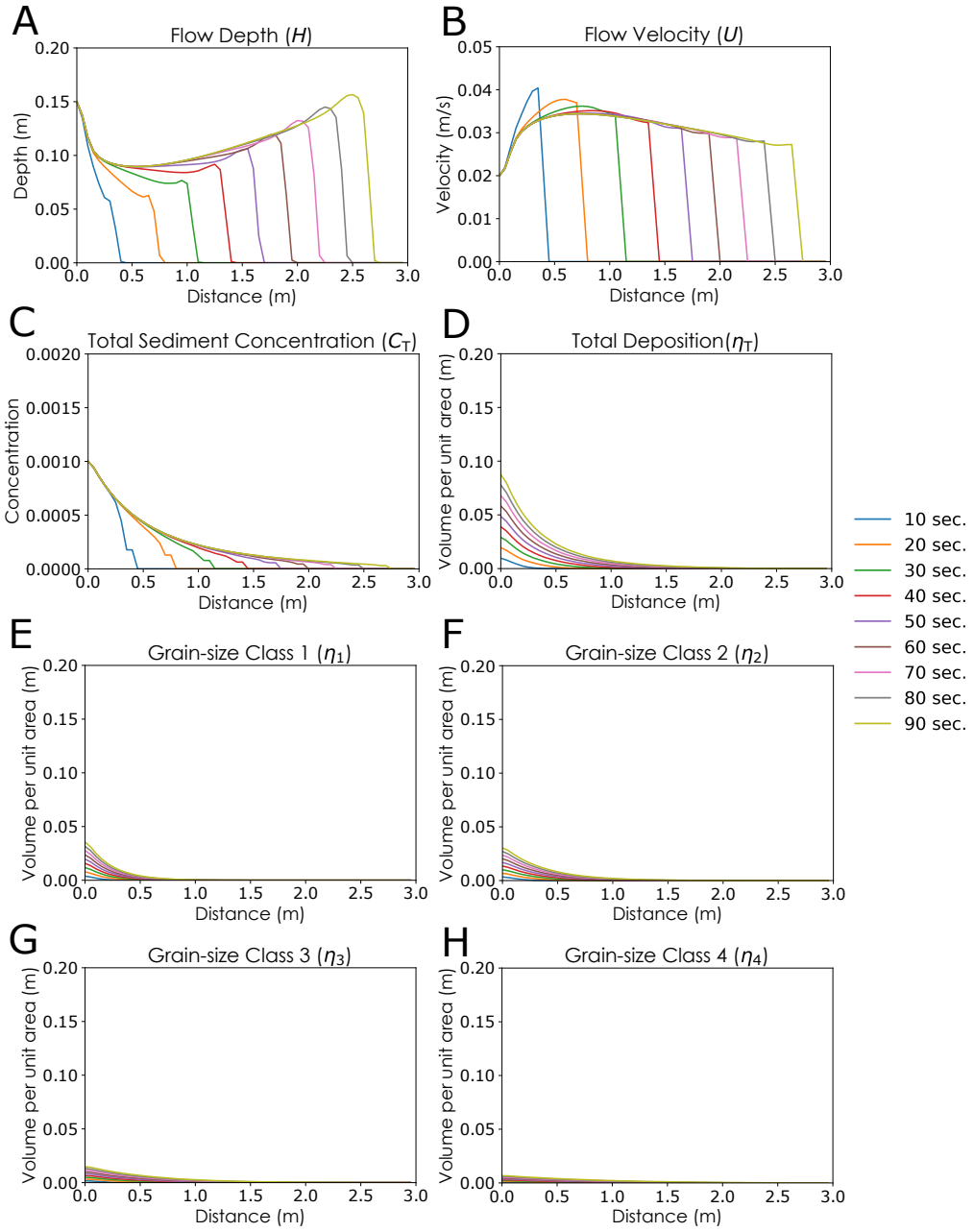

Figure 2.3: Example of forward model calculation with low initial flow velocity and sediment concentration (Table 2.1). A. Time evolution of flow depth H. B. Time evolution of flow velocity U. C. Time evolution of total sediment volumetric concentration C_T. D. Time evolution of deposit profile η_T. E. Time evolution deposit profile of grain-size class 1 η_1. F. Time evolution of deposit profile of grain-size class 2 η_2. G. Time evolution of deposit profile of grain-size class 3 η_3. H. Time evolution of deposit profile of grain-size class 4 η_4.

2.2.5 Sensitivity Tests of Forward Model

The degree of sensitivity of the forward model to changes in the initial conditions of the flow and model parameters was tested (Table 2.2). Testing was conducted using the forward model programmed for generating numerical datasets of experiments conducted with the 10% slope. Numerical simulations were conducted with different values of the six parameters H_0, U_0, $C_{T,0}$, e_s, r_o, and c_f. H_0, U_0 and $C_{T,0}$ values in Case 1 were the mid-values over the range of H_0, U_0, and $C_{T,0}$ for generating training data. Other parameters remained constant for the simulations.

The results of the sensitivity tests revealed that changes in the deposit profile occur when the initial flow conditions differ (Figure 2.4). The volume of the deposited sediment increased overall as H_0 increased (Figure 2.4A). The same trend was observed for U_0, and $C_{T,0}$ (Figures 2.4B, C). Among these three parameters, the amount of increase in the volume per unit area of deposit was greatest for $C_{T,0}$, and smallest for U_0 and H_0. Concerning model closure parameters, the resultant deposit profile showed almost no change for different values of entrainment coefficient e_s and c_f(Figures 2.4D, F). A slightly lower amount of deposition was observed for larger e_s. A small increase in the amount of deposition was observed as c_f decreased (Figure 2.4F). The volume per unit area of deposit increased moderately when r_o increased (Figure 2.4E).

Table 2.2: Settings for sensitivity tests of forward model.

Case	H_0 (m)	U_0 (m/s)	$C_{T,0}$	e_s	r_o	c_f
1	0.15	0.1	0.01	GP	1.5	0.004
2	0.3	0.1	0.01	GP	1.5	0.004
3	0.05	0.1	0.01	GP	1.5	0.004
4	0.15	0.2	0.01	GP	1.5	0.004
5	0.15	0.02	0.01	GP	1.5	0.004
6	0.15	0.1	0.02	GP	1.5	0.004
7	0.15	0.1	0.001	GP	1.5	0.004
8	0.15	0.1	0.01	GPx2	1.5	0.004
9	0.15	0.1	0.01	GPx0.5	1.5	0.004
10	0.15	0.1	0.01	GP	2.0	0.004
11	0.15	0.1	0.01	GP	1.0	0.004
12	0.15	0.1	0.01	GP	1.5	0.01
13	0.15	0.1	0.01	GP	1.5	0.007
14	0.15	0.1	0.01	GP	1.5	0.001
15	0.15	0.1	0.01	GP	1.5	0.0005

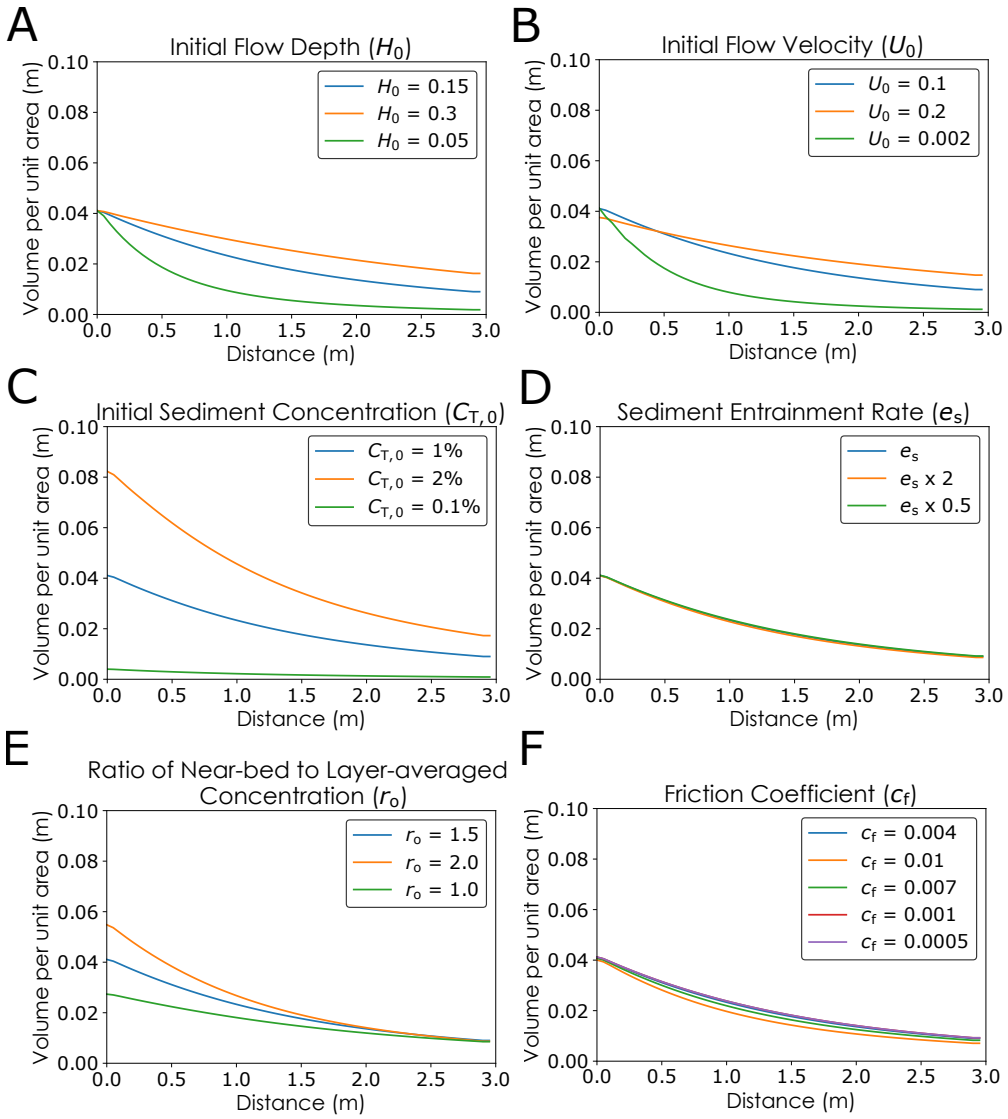

Figure 2.4: Sensitivity tests of deposit profile of numerical turbidites to change in initial flow conditions and closure parameters (Table 2.2). A. Dependency on initial flow depth H_0. B. Dependency on initial flow velocity U_0. C. Dependency on initial total sediment volumetric concentration $C_{T,0}$. D. Dependency on sediment entrainment rate e_s. E. Dependency on the ratio of near-bed to layer-averaged concentration r_o. F. Dependency on friction coefficient c_f.

2.2.6 Verification of Forward Model with Results from Previous Research

Calculations on experiment NOVA2 [*García*, 1993] were conducted under the same flow conditions and parameter settings as those used for modeling in *Kostic and Parker* [2006] to validate the numerical scheme and forward model implemented in this study. The resulting flow depth profile, velocity profile and concentration profile were compared with the model results from *Kostic and Parker* [2006] and the experiment data from *García* [1993] in Figure 2.5. The calculated flow depth profile showed an almost perfect match with that from *Kostic and Parker* [2006] (Figure 2.5A). The velocity profile was slightly higher than that of *Kostic and Parker* [2006] before the slope break, with close match for the values after the slope break (Figure 2.5B). The calculated concentration profile by the model in this study was slightly higher than that of *Kostic and Parker* [2006] (Figure 2.5C). The overall reconstruction by the model implemented in this study matched the results from the previous study by *Kostic and Parker* [2006].

2.2.7 Sensitivity of Forward Model to Different Entrainment Functions

Calculations were conducted using the same initial flow conditions as those of experiments GLASSA5 and GLASSA7 [*García*, 1993] to test sensitivity of the implemented forward model to different entrainment functions. Three different entrainment functions were tested, including functions from *van Rijn* [1984b], *Garcia and Parker* [1993], and *Dorrell et al.* [2018]. The resulting deposit profiles are shown in Figure 2.6. Measurements from *García* [1993] and model results from *Kostic and Parker* [2006] are also shown for comparison. Figures 2.6A and B show that results from the model implemented in this study showed a closer match with the experimental measurements from *García* [1993], but the deposit profile showed almost no change with the change in entrainment function. A greater difference may be visible for a field scale simulation, but for experimental turbidity currents, the effect

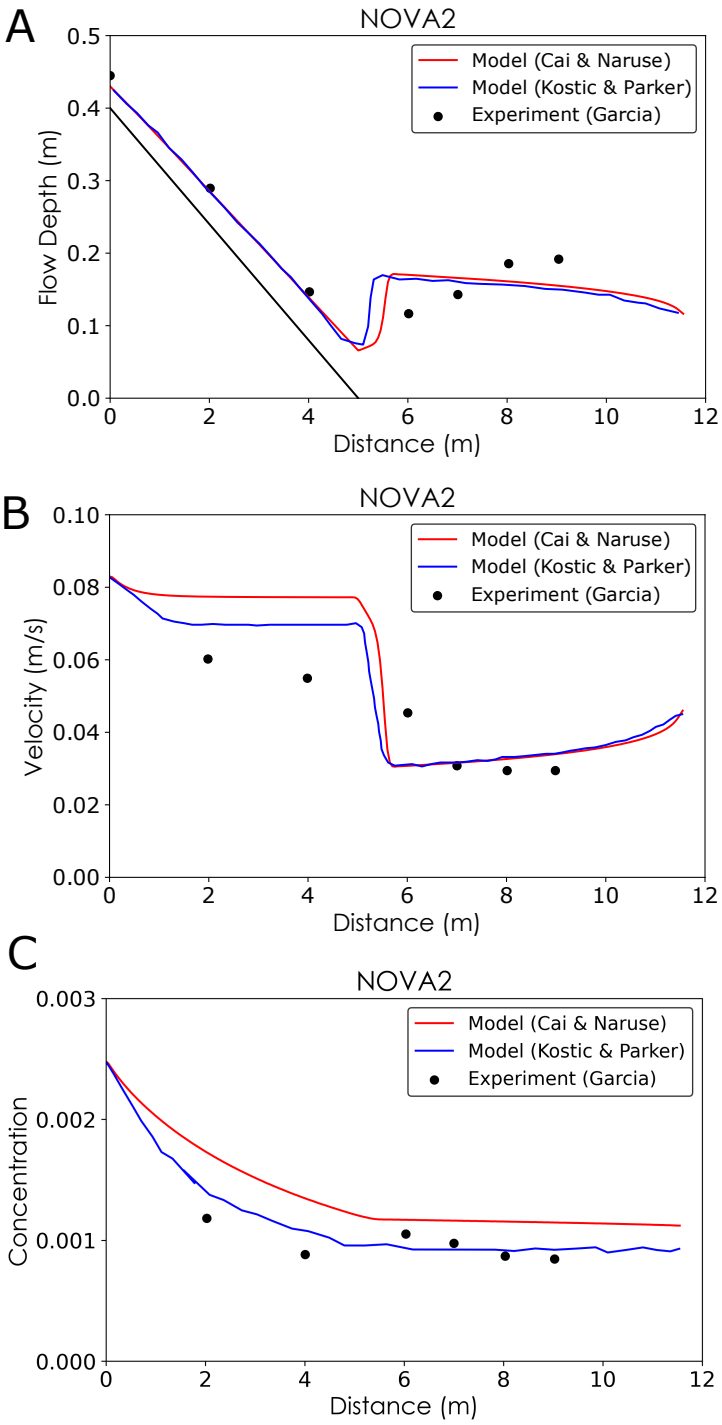

Figure 2.5: Forward model calculation results using initial flow conditions of experiment NOVA2 from *García* [1993]. Plotted with experimental measurements from *García* [1993] and model results from *Kostic and Parker* [2006]. A. Flow depth profile. B. Velocity profile. C. Concentration profile

does not seem to be visibly large.

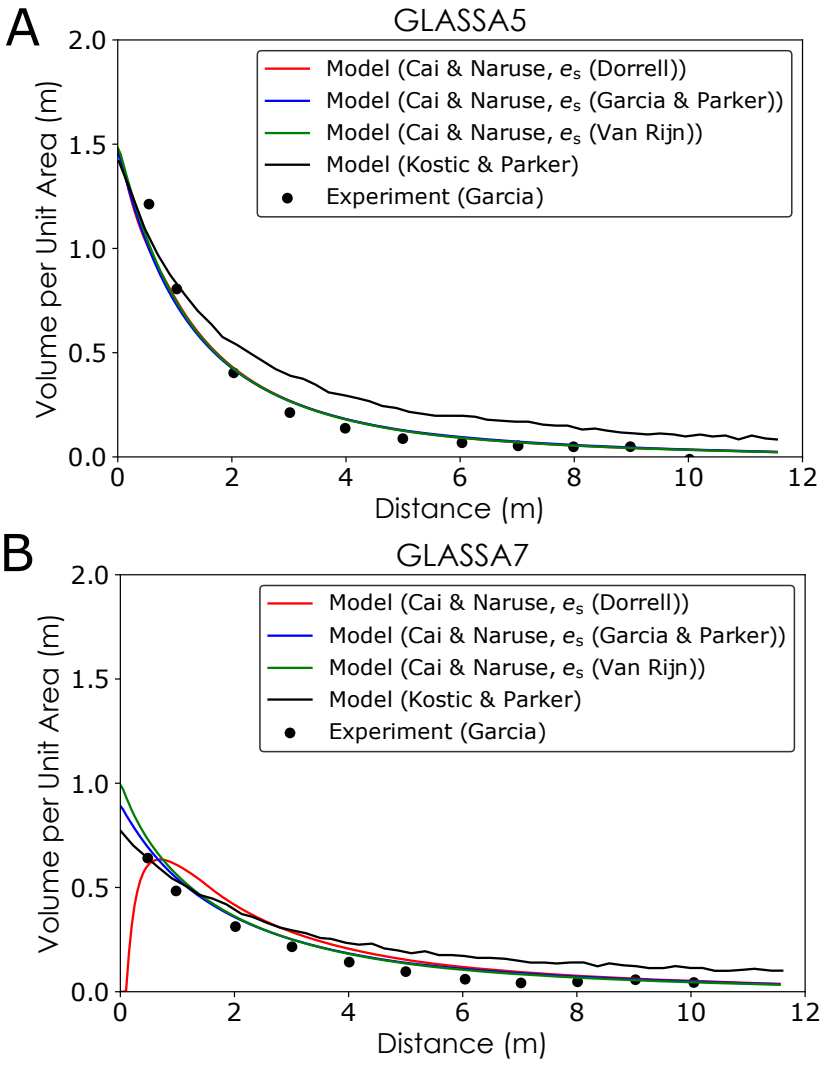

Figure 2.6: Forward model test of sensitivity to different entrainment functions using initial flow conditions of experiment GLASSA5 and GLASSA7 from [*García*, 1993]. Plotted with experimental measurements from [*García*, 1993] and model results from *Kostic and Parker* [2006]. A. Deposit profile of GLASSA5 when calculated with different entrainment functions. B. Deposit profile of GLASSA7 when calculated with different entrainment functions.

2.3 Inverse Analysis by Deep Learning Neural Network

In this method, initial flow conditions of turbidity currents are reconstructed from their turbidite deposits. The DNN model first explores the functional relationship between the initial flow conditions of turbidity currents and the resulting turbidite deposits via training. After training, the DNN model is applied to new turbidite datasets for inverse analysis. In preparation for training, numerical training datasets are generated using the forward model. During training, the training datasets are fed into the DNN. The DNN model examines the datasets and adjusts its internal parameters to make a good estimation of the initial flow conditions from the deposit profile. After training, the DNN, which can predict the initial flow conditions of new turbidites based on the functional relationship it discovered, is tested with independent numerical datasets that are also generated by the forward model and with flume experiment data. The procedure of using the DNN model as a method of inverse analysis in this study is illustrated in a flowchart in Figure 2.7.

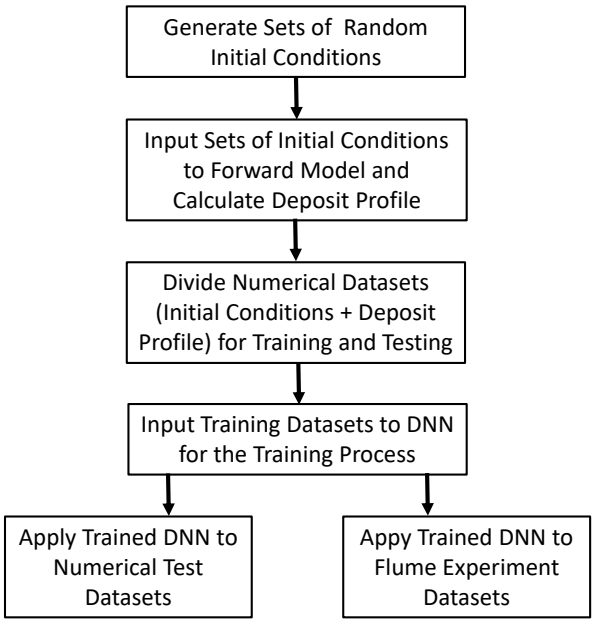

Figure 2.7: A flowchart illustrating the procedures from generation of numerical data to the application of a DNN model to numerical test datasets and flume experiment datasets.

2.3.1 Generation of Training Data

A training dataset is a combination of randomly generated initial flow conditions at the upstream boundary of the flow and a matching deposit profile calculated using the forward model. A program in Python was written to generate sets of initial flow conditions. Each set of flow conditions generated consists of an initial flow velocity U_0, an initial flow depth H_0, a flow duration T_d, and the initial concentrations of each grain-size class $C_{i,0}$. Other variables, such as slope, are set to constant values. The slope was set according to values of slope in experiments conducted (Section 2.4.1).

The forward model calculates the deposit profile of a turbidite using randomly generated initial flow conditions. The deposit profile is calculated as volume per unit area for each grain-size class at 60 locations within a 3 m range downstream from the upstream boundary. Each data point is 0.05 m away from its neighboring points. These data points are akin to sampled data from flume experiments or core or outcrop data from actual turbidites. Since fewer data points can be obtained from experiments or actual turbidites, details of deposit profiles need to be interpolated from available data points. Table 2.3 illustrates the ranges of randomly generated initial flow conditions. These ranges were decided on the basis of possible values that can be observed in experimental scale turbidity currents. Since terms in the forward model calculation were set to be consistent with experimental settings instead of natural scale turbidity currents, no range of values beyond that of experimental scale would be appropriate for the current model implemented. In this study, 10000 training datasets were used for training and 2000 datasets were used for verifying the DNN. The number of test datasets was chosen to be the same number as that of validation datasets. The test numerical datasets for verification were generated independently from the training datasets.

Table 2.3: Range of initial flow conditions generated for the production of training datasets.

Parameter	Minimum	Maximum
H_0 (m)	0.01	0.3
U_0 (m/s)	0.01	0.2
$C_{i,0}$	0.0002	0.005
T_d (s)	180	1080

2.3.2 Structure of Deep Learning Neural Network

The type of neural network (NN) used in this study is a fully connected NN, which consists of an input layer, several hidden layers, and an output layer. Each layer consists of some nodes. Each node connects with every node in the adjacent layers (Figure 2.8A). Nodes in the input layer hold deposit profile values, i.e., the volume-per-unit-area for all grain-size classes at spatial grids. Nodes in the output layer hold estimates of parameters to be reconstructed, which in this case are the initial flow conditions U_0, H_0, $C_{i,0}$, and the flow duration T_d. The activation function used in this study is the rectified linear unit (ReLU), which is one of the most commonly used activation functions for DNNs and is proven to perform calculations at a higher speed than other activation functions [*Krizhevsky et al.*, 2012].

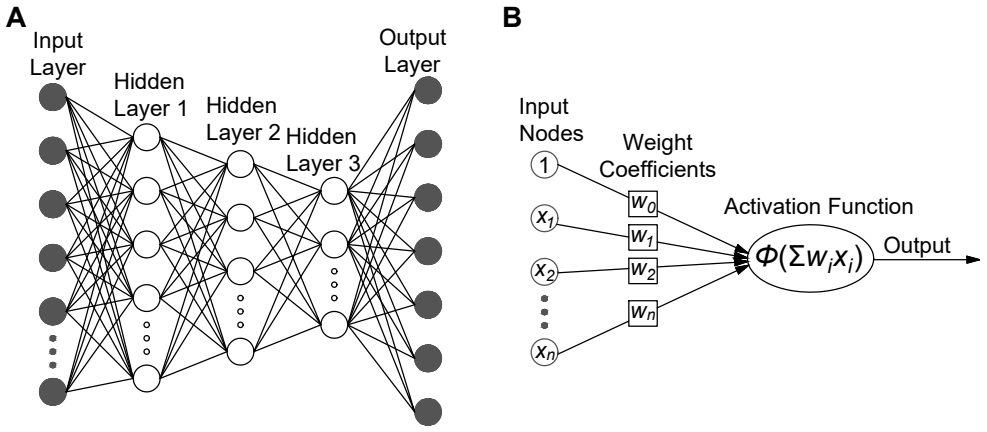

Figure 2.8: Schematic diagrams of DNN. A. Overall structure of DNN. B. Concept of weight coefficient and activation function.

Before training, the weight coefficients are set to random values. As the training process begins, deposit profile values from the training datasets are fed into the input layer. These values propagate through the hidden layers of the DNN, and estimates of the initial flow conditions are outputted at the output layer. At this point in the training process, the DNN model is yet to adapt its internal variables to the functional relationship between turbidite deposits and initial flow conditions. Thus, the initial estimates are expected to largely differ from the actual values. To explore this functional relationship, a loss function is used to evaluate the accuracy of the estimated values. The loss function used in this case is the mean squared error function, which is considered as one of the best functions for regression [*Wang and Bovik*, 2009]. The gradient of the loss function is calculated and fed back to the hidden layers of the DNN model through backpropagation [*Nielsen*, 2015; *Schmidhuber*, 2015], where the internal values of the DNN model are optimized toward minimizing the difference between the estimated and actual values. This process is repeated for every epoch of calculation. An epoch is a cycle of calculation in a DNN that involves one forward pass and one backpropagation of all training data.

The optimization algorithm used in this study is stochastic gradient descent (SGD), which drastically reduces the amount of calculation involved in training without compromising accuracy compared to previous gradient descent algorithms [*Bottou*, 2010]. In this study, Nesterov momentum is used with SGD [*Ruder*, 2016]. Because of the difference in the order of the range of the initial flow conditions, the training datasets should be normalized before they are inputted to the DNN. In this case, all values are normalized to be between 0 and 1 for the DNN model to consider all parameters at equal weights. The hyperparameters, including the number of layers, number of nodes at each layer, dropout rate, validation split, learning rate, batch size, epoch, and momentum, were adjusted manually. Various combinations were attempted. The best combination of hyperparameters was chosen on the basis of the performance of the DNN, which is judged on the basis of the final validation loss.

In this study, the DNN model was developed using Python with the package Keras 2.2.4. The package Tensorflow 1.14.0 [*Abadi et al.*, 2015] was used for backend calculations. Calculations were performed using GPU NVIDIA GeForce GTX 1080 Ti.

2.3.3 Evaluation of Trained DNN Model

During the verification of the DNN model with test numerical datasets (Section 2.5.1), the reconstruction result of each parameter was evaluated using bias (B) and sample standard deviation (s) of residuals. The calculations were performed using the following equations:

$$B = \frac{\sum x_i}{n}, \tag{2.17}$$

$$s = \sqrt{\frac{\sum (x_i - B)^2}{n-1}}, \tag{2.18}$$

where n represents the number of test datasets, and x_i denotes the residual of the specific reconstructed parameter for the ith test dataset. The value of s for each reconstructed parameter was compared with a representative value C_v^*, which is the mid-value over the range in which the specific parameter was generated (Table 2.3). The confidence interval of B was determined using the bootstrap resampling method [*Davison and Hinkley*, 1997]. Resampling of B was conducted 10000 times, and the 95% confidence interval (CI) of B was determined.

During the verification of the DNN model using flume experiment data (Section 2.5.4), linear interpolation was first applied to the sampled experimental deposit datasets so that the number of data points for one experimental dataset was the same as that for a training dataset. Then, flow parameters at the upstream end of the simulation were reconstructed from the measured properties of the deposit profile. The upstream end of the simulation was set at 1.0 m from the inlet of the flume. The reconstructed parameters were inputted into the forward model so that downstream flow parameters and the time evolution of the deposit profile were calculated. The calculated downstream flow parameters were compared

with the flow conditions measured during experiments. The deposit profile calculated from the reconstructed flow parameters was also compared with the measured deposit profile that was used for inversion.

To evaluate the precision of reconstruction, Jackknife method [*McIntosh*, 2016] was applied to the sampled deposit values and delete-1 Jackknife samples were generated. Inverse analysis by the DNN model was performed for the delete-1 Jackknife samples, and downstream flow parameters were calculated for each sample. There were 18 delete-1 Jackknife samples for each experiment, since the deposits were sample at 18 locations. Considerng the small sample size (less than 30), t-distribution was used instead of noraml distribution. The 95% confidence interval of t-distribution is $\pm(t \times s_{\overline{x}})$, where $s_{\overline{x}}$ is the standard error and is defined by the following equations:

$$\overline{x} = \frac{\sum_{i=1}^{n} x_i}{n}, \tag{2.19}$$

$$s_{\overline{x}} = \sqrt{\frac{\sum_{i=1}^{n} (x_i - \overline{x})^2}{n(n-1)}}, \tag{2.20}$$

where n represents the sample size, x_i denotes the jackknife sample where the ith sampled deposits value were eliminated, and $\overline{x}$ is the mean of x_i. The value t is a standarized value determined by the degree of freedom and the alpha level. Degree of freedom is the sample size subtracted by 1. In this case, the sample size is 18, thus degree of freedom is 17. For 95% confidence interval, the alpha level is 0.05. According to the two-tails t-distribution table, t for our samples is 2.110.

2.4 Flume Experiments

2.4.1 Experiment Settings

The flume was made of acrylic panels and was 4 m in length, 0.12 m in width, and 0.5 m in depth. During the experiments, it was submerged in a tank made of glass panels and a steel supporting frame. The tank was 5.5 m in length, 2.5 m in width, and 1.8 m in depth.

The slope of the channel floor changed at 1.0 m from the inlet, where a was the upstream slope and b was the downstream slope (Figure 2.9). Values of a and b for each experiment are stated in Table 2.4.

Sediment was mixed with water in two mixing tanks before the experiments. During the experiments, the mixture of sediment and water was first pumped to the constant head tank and then released into the flume. The flow into the flume was controlled via a valve at the base of the constant head tank. Flow discharge was regulated by changing the degree of valve opening. The amount of mixture in the constant head tank was kept at a constant level during the experiments to maintain a stable flow discharge. The damping tank at the downstream end of the flume prevented any reflection of flow toward the upstream direction. A pipe of freshwater supply was placed at the top of the damping tank, and a draining pipe was placed at the bottom of the damping tank. The combination of these two pipes kept the level of water in the tank constant and prevented the reflection of flow.

Five experiments were conducted using plastic particles in this study. The density of the plastic particles used was 1.45 g/cm^3. Two experiments (experiments PP1, PP2) were performed using polyvinyl chloride, which had an average grain diameter of 0.120 mm, and melamine, which had an average grain diameter of 0.220 mm (Section 2.4.3). Three experiments (experiments PP3, PP4, PP5) were performed with two types of melamine, which had an average grain diameter of 0.120 mm and 0.220 mm, respectively (Section 2.4.3).

2.4.2 Measurements and Data Analysis

Before each experiment, the tank water temperature was measured using a glass alcohol thermometer. The mixture in the tank was sampled with a 500 mL beaker to measure the initial concentration in the tank. Flow velocity was measured using an acoustic Doppler velocity profiler (ADVP; Nortek Vectrino Profiler). The maximum functional range of the ADVP used was $4.0 - 7.0$ cm below the probe. The actual range of reliable measurement may be shorter if the signal-to-noise ratio (SNR) of data collected is below a certain thresh-

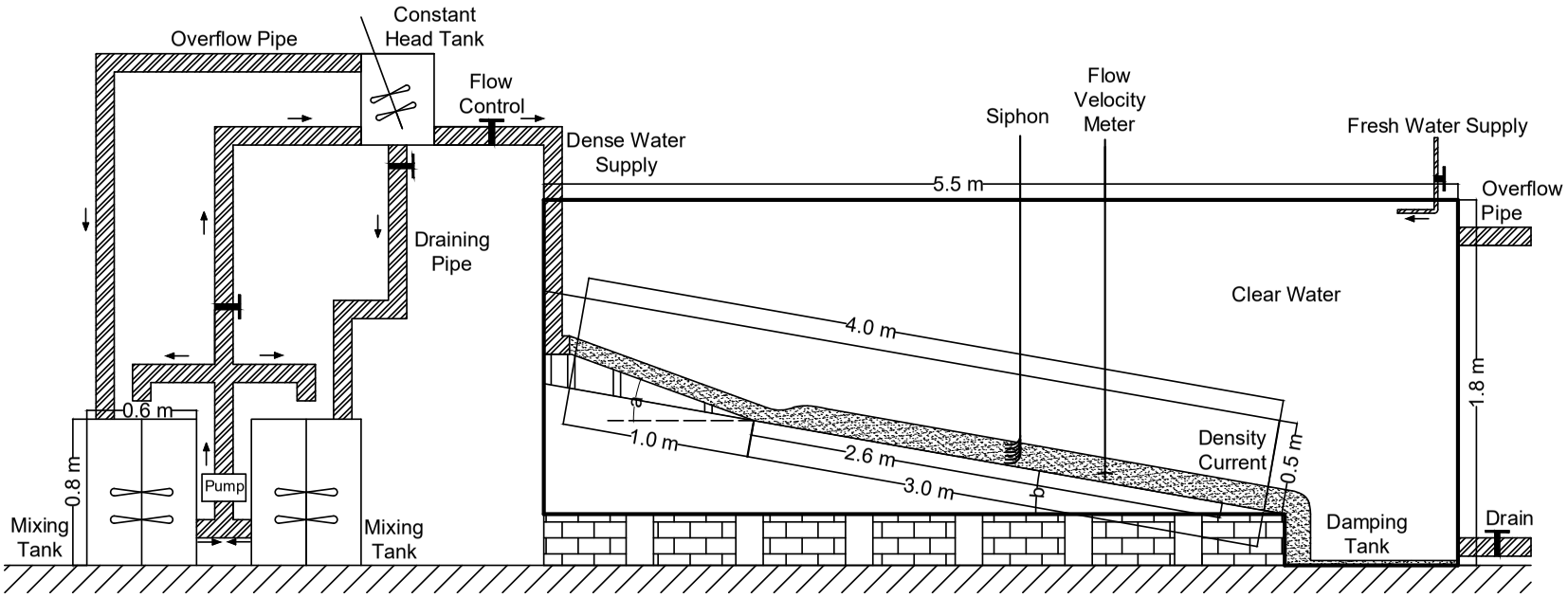

Figure 2.9: Schematic diagram of flume used for experiment.

old (2.4.4). To obtain the vertical velocity profile of the flow, an actuator was used to adjust the position of the ADVP during the experiments.

A siphon with 10 plastic tubes was used to measure the suspended sediment concentration of the flow. The tubes were aligned vertically at 1.0 cm intervals and were positioned such that samples were collected at 0.0 to 9.0 cm above the bed. Aluminum tubes with an outer diameter of 8.0 mm and an inner diameter of 5.0 mm were attached to the outlets of plastic tubes to keep them in place. Sampling by siphon was conducted when the flow reached a quasi-equilibrium state. The state of flow was determined by observing the development of the flow. Two single-lens reflex cameras were used to record the experiments. Flow depth was determined based on the video recorded.

After the experiments, the flume was left untouched for 1 to 3 days for the suspended sediment to settle. Afterward, photos were taken from a lateral view perpendicular to the flume. The lateral view of the deposited sediment was photographed with a ruler beside it. The height of the deposit was determined from the photos. Water was then gradually drained from the tank with a bath pump at a rate of 0.0002333 m^3/s. After the water was drained, deposited sediment was sampled at 20 cm intervals starting from the upstream boundary of the flume.

Samples from the siphon and the mixing tank were first weighed immediately after they were collected. Then, they were dried in a drying oven at 70°C along with the deposit samples. Samples from the siphon and the mixing tank were weighed again after drying. The measurements were used for calculating the sediment concentration in the flow and tank. Grain size distribution analysis was performed in a settling tube for all dried sediment samples. The settling tube used was 1.8 m in length. The calculation of grain size distribution was performed using STube [*Naruse*, 2005]. Particle settling velocity was calculated using *Gibbs* [1974]. The measured grain size distribution of sediment was discretized to four grain-size classes with representative grain diameter D_i for grain-size classes 1, 2, 3, and 4 were set to be 210, 149, 105, and 74.3 μm, respectively.

In steady flow conditions, the relationship between the layer-averaged flow velocity U, the layer-averaged sediment volumetric concentration C, and the flow depth H is defined as follows [*Garcia and Parker*, 1993]:

$$UCH = \int_a^\infty u_z c_z dz, \tag{2.21}$$

where u_z and c_z represent the flow velocity and sediment volumetric concentration, respectively, at elevation z above the bed. The relationship between the layer-averaged flow velocity U and the velocity maximum U_m is defined by the following equation [*Altinakar et al.*, 1996]:

$$\frac{U_\mathrm{m}}{U} = 1.3. \tag{2.22}$$

The layer-averaged flow velocity was calculated from the velocity maximum of the profile measured by the ADVP using the relationship described by equation 2.22. The sediment volumetric concentration was calculated from siphon measurements using the relationship described by equation 2.21.

2.4.3 Experimental Conditions

Experimental conditions for the five runs conducted are outlined in Table 2.4. C_TT represents the total concentration of sediment in the mixing tank. C_1T, C_2T, C_3T, and C_4T represent the concentrations of grain-size classes 1, 2, 3, and 4, respectively. Parameter x_C represents the position of the siphon downstream, whereas x_U represents the position of ADVP downstream. x_H represents the position in which the flow depth was measured from a video taken during the experiments. x_U, x_C and x_H were changed for each run because of limitations in the flume setup at the time of the experiments. Temperature is the measured temperature of clear water in the tank before the experiments.

Table 2.4: Conditions and settings of experiments conducted.

	PP1	PP2	PP3	PP4	PP5
C_{TT}	0.0191	0.0276	0.0120	0.0141	0.0101
C_{1T}	0.0102	0.0160	0.00230	0.00453	0.00290
C_{2T}	0.00713	0.00820	0.00670	0.00657	0.00446
C_{3T}	0.00146	0.00254	0.00250	0.00246	0.00199
C_{4T}	0.000366	0.000817	0.000460	0.000567	0.000766
x_C (m)	1.08	2.10	1.50	1.50	1.50
x_U (m)	1.46	2.48	1.20	1.20	1.20
x_H (m)	1.10	1.10	1.20	1.20	1.20
Temperature (°C)	22.5	17.0	13.0	13.5	14.0
Slope a	26.8%	26.8%	25.6%	25.6%	25.6%
Slope b	10.0%	10.0%	8.00%	8.00%	8.00%

2.4.4 Flow Velocity Profile and the Corresponding Signal-to-Noise Ratio (SNR)

The accuracy of flow velocity measurements by the ADVP used (Nortek Vectrino Profiler) was affected by the Singal-to-Noise Ratio (SNR). According to the user manual of Nortek Vectrino Profiler, the "weak spot" of acoustic profile measurement due to pulse interference can be detected from the SNR values. The manual states that the SNR value of measurements need to be at least 30 dB to be considered reliable. Data with SNR between 20 dB and 30 dB should be used with caution and data with SNR lower than 20 dB should not be trusted. The measured velocity profile for each experiment and the matching SNR profile are shown in Figures 2.10 and 2.11. The height above bed of ADVP differed for the experiments conducted, thus the range of measured profiles above bed were also different.

From Figures 2.10 and 2.11, it was apparent that SNR of velocity measurements for experiments PP1 and PP2 were much higher than those of experiments PP3, PP4, and PP5. The SNR values of PP1 and PP2 were above 40 dB. Experiment PP3 had slightly better SNR profile than PP4 and PP5, with the peak SNR above 40 dB, but the lowest SNR barely above 30 dB. Experiment PP4 had especially low SNR, with the peak SNR slightly above 30 dB. SNR of PP5 was above 40 dB toward the bottom, but decreased below 30 dB toward

the top. While the entire velocity profile can be used for analysis of PP1 and PP2, only regions with high SNR can be used for PP3, PP4, and PP5.

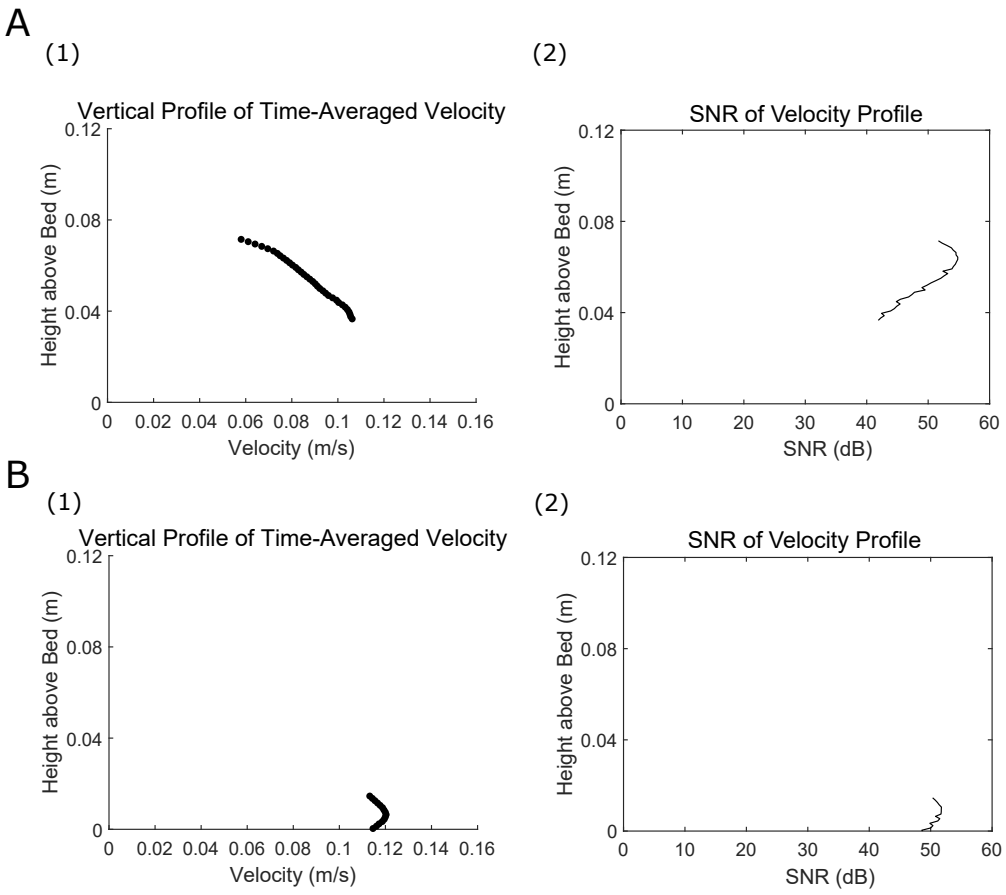

Figure 2.10: Time-averaged velocity profile and SNR of velocity profile for experiments conducted with 10.0% slope. A. (1) Time-averaged velocity profile of PP1. (2) SNR of velocity profile for PP1. B. (1) Time-averaged velocity profile of PP2. (2) SNR of velocity profile for PP2.

2.5 Results

Inverse analysis was applied to deposits within a 2.6 m range downstream of the beginning of slope *b* (1.0 m from the inlet of flow). Due to the limited size of the flume, slope *a* was set to a steep angle (26.8% or 25.6%) in all five experiments to ensure that the flow accelerates sufficiently for entrainment to occur. Considering the instabilities near the inlet and the

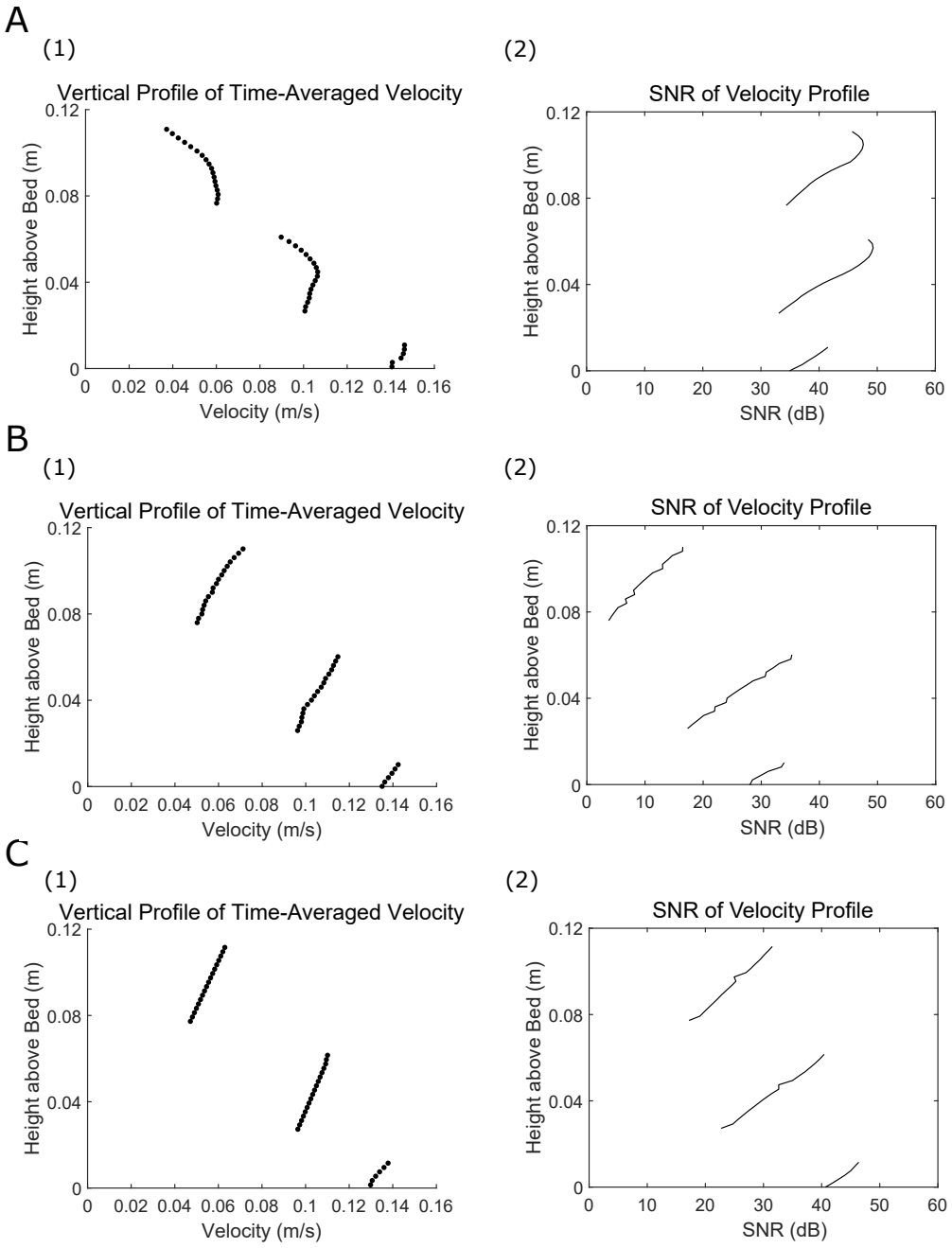

Figure 2.11: Time-averaged velocity profile and SNR of velocity profile for experiments conducted with 8.00% slope. A. (1) Time-averaged velocity profile of PP3. (2) SNR of velocity profile for PP3. B. (1) Time-averaged velocity profile of PP4. (2) SNR of velocity profile for PP4. C. (1) Time-averaged velocity profile of PP5. (2) SNR of velocity profile for PP5.

overly steep slope, the region with slope a was excluded from numerical simulations and inverse analysis. For the generation of numerical datasets, the upstream boundary of the simulation was set at the beginning of slope b, and calculations were performed for a 3.0 m range downstream. The actual sampling of experiment deposits was performed only up to 2.6 m from the beginning of slope b (Figure 2.9), because deposits beyond the region were too thin to be collected for some experiments. Only simulation data from the same range were used for training and verification to match the actual sampling range of experiment deposits.

For hyperparameters used during training, the dropout rate, validation split, and momentum for the DNN model were set to 0.5, 0.2, and 0.9, respectively. The learning rate was set to 0.01. The batch size was set to 32 and the number of layers was set to 5. The number of nodes each layer was 2000. Epoch was 20000. With this setting the validation loss was 0.0033 for training with 10.0% slope datasets and 0.0038 for training with 8.00% slope datasets. Figures 2.12A and 2.13A show that overlearning did not occur, as no deviation was observed between the resulting values of the loss functions for the training and validation datasets.

2.5.1 Verification with Test Numerical Datasets: Overview

This section presents the verification results with numerical test datasets. Parameter reconstruction results by the DNN model are shown in Figures 2.12 and 2.13. Parameters reconstructed include flow duration T_{d} and flow conditions at the upstream end (flow velocity U_0, flow depth H_0, and sediment concentrations $C_{i,0}$). Separate verification was performed with numerical datasets of experiments conducted with 10.0% slope and 8.00% slope. Verification results are described in Sections 2.5.2 and 2.5.3.

2.5.2 Verification with Test Numerical Datasets of 10.0% Slope Experiments

Overall, the reconstructed values mostly matched with the original values, with a few outliers (Figure 2.12B-H). However, a greater degree of scattering was observed for T_d compared with other parameters.T_d seemed show a tendency of being underestimated (Figure 2.12B). The ranges of misfit ($2s$) were reasonable for all parameters, which had $2s/C_v^*$ values under 22.0% (Table 2.5). For $C_{i,0}$, zero was within the 95% CI of B , but not for T_d, U_0, and H_0. CI range was below zero for T_d and U_0 and above zero for H_0.

Table 2.5: Sample standard deviation and bias of the inversion result for numerical datasets of experiments conducted with 10.0% slope.

Parameters	s	C_v^*	$2s/C_v^*$	B	CI of B
U_0 (m/s)	0.00577	0.105	0.110	-0.00234	(-0.00316, -0.00155)
H_0 (m)	0.00978	0.155	0.126	0.00164	(0.000286, 0.00301)
T_d (s)	68.6	630	0.218	-49.4	(-59.1, -40.1)
$C_{1,0}$	0.000254	0.0026	0.195	0.0000318	(-0.00000234, 0.0000679)
$C_{2,0}$	0.000278	0.0026	0.214	0.0000292	(-0.00000832, 0.0000681)
$C_{3,0}$	0.000280	0.0026	0.215	0.0000149	(-0.0000237, 0.0000536)
$C_{4,0}$	0.000271	0.0026	0.209	0.0000234	(-0.0000130, 0.0000617)

2.5.3 Verification with Test Numerical Datasets of 8.00% Slope Experiments

Overall, good correlations were observed for the reconstructed and original values of flow parameters. The reconstructed values were mostly consistent with the original values, with a few outliers (Figure 2.13B-H). Similar to the test datasets described in Section 2.5.2, a tendency of underestimation was observed for T_d (Figure 2.13B). The range of misfit ($2s$) was reasonable for all parameters, which had $2s/C_v^*$ values under 23.0% (Table 2.6). Zero was included in the 95% CI of B for U_0, $C_{2,0}$, and $C_{3,0}$, but not for T_d, H_0, $C_{1,0}$, and $C_{4,0}$. CI range was below zero for T_d and H_0 and above zero for $C_{1,0}$ and $C_{4,0}$.

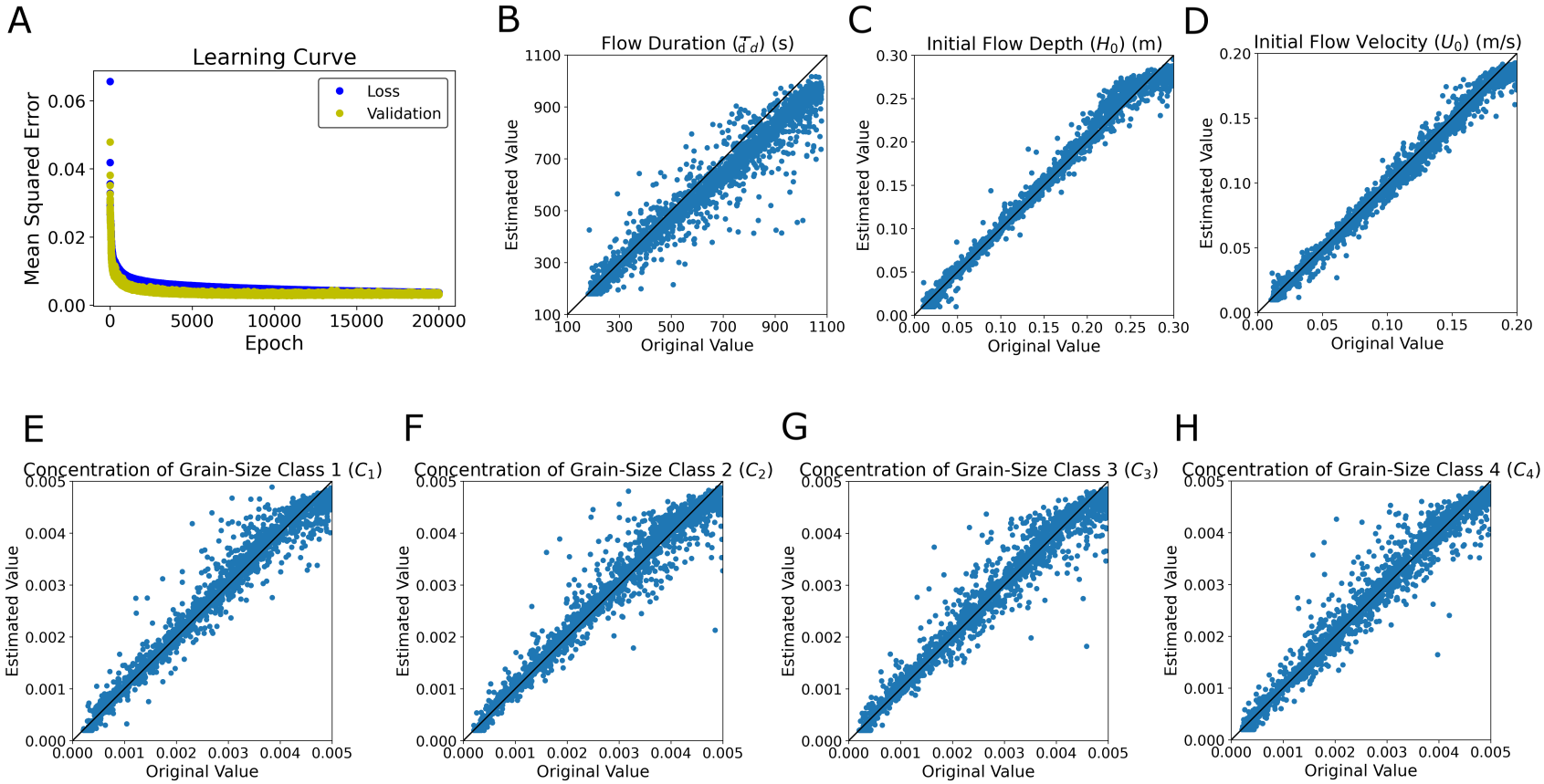

Figure 2.12: Results of verification with independent numerical datasets (slope = 10.0%). The black diagonal line in each graph is where values on the x-axis (the true values) equal to the values on the y-axis (the estimated values). If a point lies on this line, the reconstructed value matches the true value perfectly. A. Learning curve. B. Estimates of T_d. C. Estimates of H_0. D. Estimates of U_0. E. Estimates of $C_{1,0}$. F. Estimates of $C_{2,0}$. G. Estimates of $C_{3,0}$. H. Estimates of $C_{4,0}$.

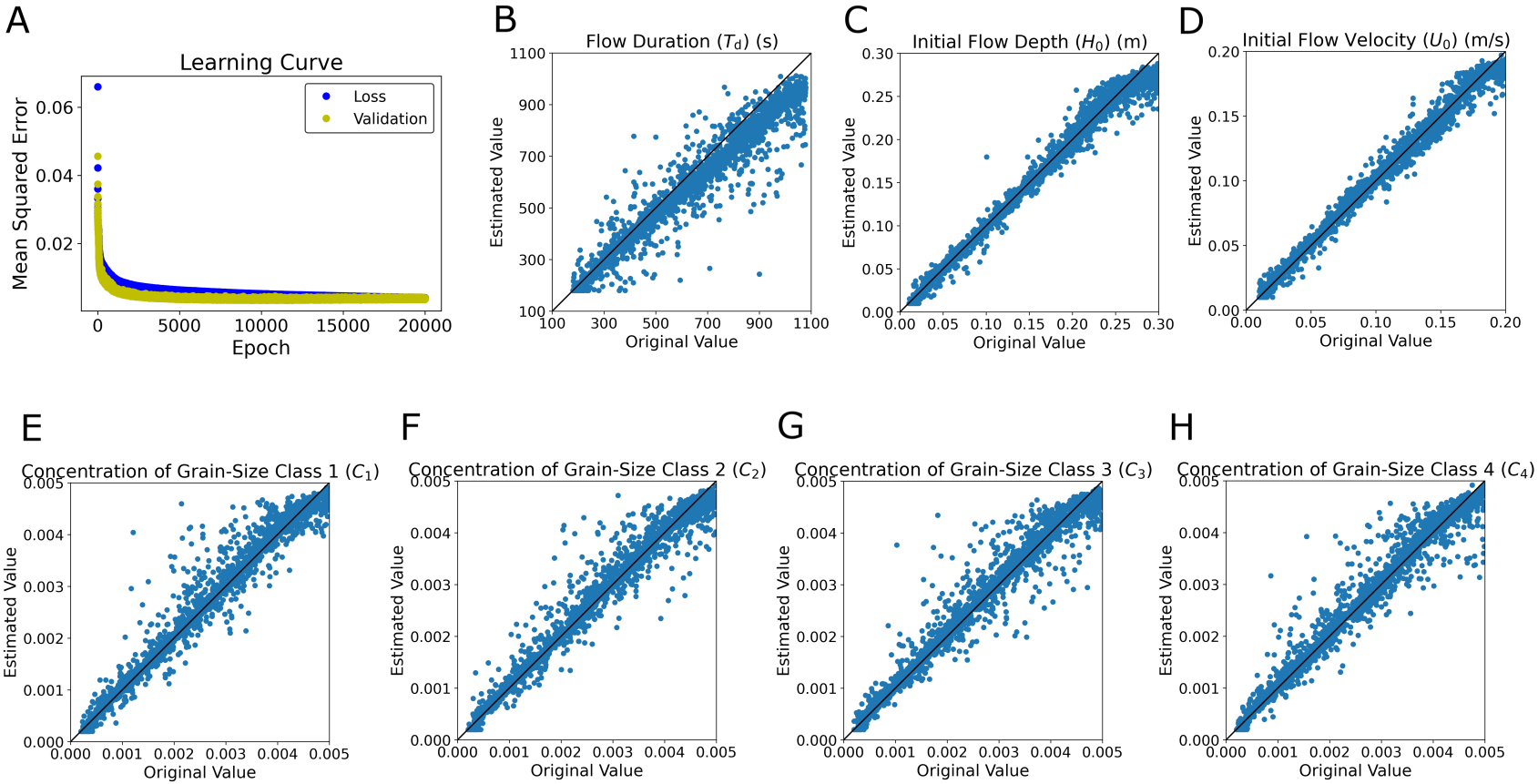

Figure 2.13: Results of verification with independent numerical datasets (slope = 8.00%). The black diagonal line in each graph is where values on the x-axis (the true values) equal to the values on the y-axis (the estimated values). If a point lies on this line, the reconstructed value matches the true value perfectly. A. Learning curve. B. Estimates of T_d. C. Estimates of H_0. D. Estimates of U_0. E. Estimates of $C_{1,0}$. F. Estimates of $C_{2,0}$. G. Estimates of $C_{3,0}$. H. Estimates of $C_{4,0}$.

Table 2.6: Sample standard deviation and bias of the inversion result for numerical datasets of experiments conducted with 8.00% slope.

Parameters	s	C_v^*	$2s/C_v^*$	B	CI of B
U_0 (m/s)	0.00637	0.105	0.121	0.000369	(-0.000532, 0.00124)
H_0 (m)	0.0107	0.155	0.138	-0.00225	(-0.00376, -0.000790)
T_d (s)	72.1	630	0.229	-47.3	(-57.4, -37.5)
$C_{1,0}$	0.000285	0.0026	0.219	0.0000538	(0.0000149, 0.0000947)
$C_{2,0}$	0.000279	0.0026	0.215	0.0000339	(-0.00000493, 0.0000736)
$C_{3,0}$	0.000296	0.0026	0.228	0.0000393	(-0.00000157, 0.0000806)
$C_{4,0}$	0.000288	0.0026	0.221	0.0000464	(0.00000740, 0.0000871)

2.5.4 Inverse Analysis of Flume Experiment Data: Overview

In this section, the calculated deposit profiles and grain size distributions are compared with the actual deposit profiles sampled from the experiments (Figures 2.14, 2.15). The results of the reconstructed flow conditions, including flow velocity U_{x_U}, flow depth H_{x_H}, sediment concentrations C_{x_C}, and flow duration T_d, are compared with the measured values (Tables 2.7 and 2.8). H_{x_H} is the flow depth H at position x_H (see the positions in Table 2.4) downstream when the flow reached a quasi-equilibrium state. U_{x_U} is the velocity U at position x_U downstream when the flow reached a quasi-equilibrium state. C_{x_C} is the C at position x_C downstream when the flow reached a quasi-equilibrium state. Inverse analysis results of the experiments conducted with 10.0% slope (PP1, PP2) and 8.00% slope (PP3, PP4, PP5) are described in Sections 2.5.5 and 2.5.6.

2.5.5 10.0% Slope Experiments (PP1, PP2)

Deposit profiles of experiments PP1 and PP2 demonstrated a thinning and fining downstream trend with concave-upward geometry. For both runs, the reconstructed deposit profiles of the total deposition almost entirely overlapped with the sampled data (Figures 2.14A(1), B(1)). The reconstructed grain size distributions at 1.4 m and 1.8 m downstream also agreed with the measured values for both experiments (Figures 2.14A(2),(3), B(2),(3)).

For flow depth H_{x_H}, the measured and reconstructed values were in good agreement (Figure 2.16A). The measured H_{x_H} of PP1 was 0.116 m and the reconstructed value was 0.157 m with a uncertainty range (95% confidence interval) of $\pm$0.00921 m. The measured H_{x_H} of PP2 was 0.123 m and the reconstructed value was 0.142 m with a uncertainty range of $\pm$0.00849 m. Reconstructed H_{x_H} of both PP1 and PP2 had a relatively small uncertainty range in comparison to the meausred and reconstructed values. The percent errors between reconstructed and measured H_{x_H} were 35.1% and 15.3% for PP1 and PP2, respectively (Table 2.7). For flow velocity U_{x_U}, the measured value of PP1 was 0.0812 m/s and the reconstructed value was 0.793 m/s with a uncertainty range of $\pm$0.00360 m/s. The measured U_{x_U} of PP2 was 0.924 m/s and the reconstructed value was 0.109 m/s with a uncertainty range of $\pm$0.00817 m/s. The uncertainty range of reconstructed U_{x_U} for both PP1 and PP2 were also relatively small in comparison to the meausred and reconstructed values. The percent errors between reconstructed and measured U_{x_U} were 2.38% and 17.9%, of which that of PP1 was lower than that of PP2.

The measured value of flow duration T_d for PP1 was 936 s and the reconstructed value was 494 s with a uncertainty range of $\pm$58.6 s. The measured T_d for PP2 was 966 s and the reconstructed value was 920 s with a uncertainty range of $\pm$72.6 s. The percent errors between reconstructed and measured T_d were 47.2% (PP1) and 4.76% (PP2). Reconstructed values for T_d were lower than the meausred values (Table 2.7). The measured value of total flow concentration C_{T,x_C} for PP1 was 0.000808 and the reconstructed value was 0.00702 with a uncertainty range of $\pm$0.000667. The measured C_{T,x_C} for PP2 was 0.00410 and the reconstructed value was 0.00344 with a uncertainty range of $\pm$0.000462. The percent errors between reconstructed and measured C_{T,x_C} were 768% (PP1) and 16.1% (PP2), of which that of PP1 had a significantly larger deviation than that of PP2. The reconstructed values of each grain-size class were mostly overestimated (Figure 2.16D).

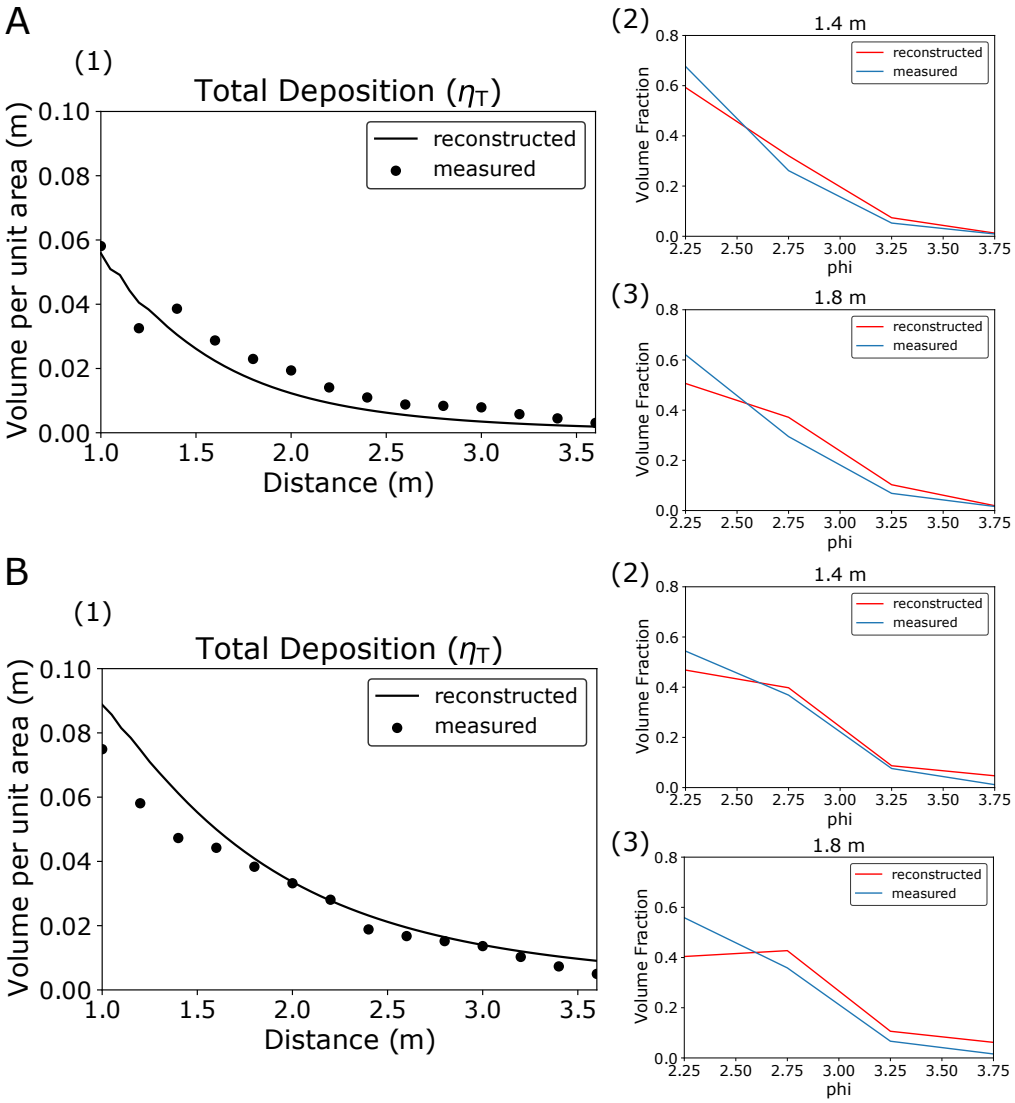

Figure 2.14: Reconstructed deposit profiles and sampled deposit data of experiments PP1 and PP2. A. (1) Reconstructed and sampled η_T of PP1. (2) Grain size distribution at 1.4 m downstream. (3) Grain size distribution at 1.8 m downstream. B. (1) Reconstructed and sampled η_T of PP2. (2) Grain size distribution at 1.4 m downstream. (3) Grain size distribution at 1.8 m downstream.

Table 2.7: Measured and reconstructed flow conditions for experiments PP1 and PP2. (R.: Reconstructed, M.: Measured)

Parameters	PP1 R.	PP1 M.	Percent Error	PP2 R.	PP2 M.	Percent Error
C_{T,x_C}	0.00702±0.000667	0.000808	768%	0.00344±0.000462	0.00410	16.1%
C_{1,x_C}	0.00333±0.000274	0.0000911	3560%	0.000623±0.0000924	0.000612	1.80%
C_{2,x_C}	0.00250±0.000244	0.000389	541%	0.00135±0.000189	0.00224	39.9%
C_{3,x_C}	0.000915±0.000125	0.000228	302%	0.000683±0.0000834	0.000944	27.7%
C_{4,x_C}	0.000272±0.0000509	0.0000999	172%	0.000788±0.000106	0.000303	160%
H_{x_H} (m)	0.157±0.00921	0.116	35.1%	0.142±0.00849	0.123	15.3%
U_{x_U} (m/s)	0.0793±0.00360	0.0812	2.38%	0.109±0.00817	0.0924	17.9%
T_{d} (s)	494±58.6	936	47.2%	920±72.6	966	4.76%

2.5.6 8.00% Slope Experiments (PP3, PP4, PP5)

Similar to the results of PP1 and PP2, deposit profiles in experiments PP3, PP4, and PP5 showed thinning and fining downstream trends. The reconstructed deposit profiles of the total deposition closely matched the sampled data for PP4 and PP5 (Figures 2.15B(1), C(1)) but was slightly greater than the measured values for PP3 (Figure 2.15A(1)). The reconstructed grain size distributions at 1.4 m and 1.8 m downstream agreed well with the measured values for all three experiments (Figures 2.15A(2),(3), B(2),(3), C(2),(3)).

The measured H_{x_H} of PP3 was 0.149 m and the reconstructed value was 0.192 m with a uncertainty range (95% confidence interval) of $\pm$0.0145 m. The measured H_{x_H} of PP4 was 0.232 m and the reconstructed value was 0.258 m with a uncertainty range of $\pm$0.0180 m. For PP5, the measured H_{x_H} was 0.196 m and the reconstructed value was 0.126 m with a uncertainty range of $\pm$0.00925 m. Reconstructed H_{x_H} of PP3, PP4, and PP5 had a relatively small uncertainty range in comparison to the meausred and reconstructed values. The percent errors between reconstructed and measured H_{x_H} were 28.8%, 11.1%, and 35.7% for PP3, PP4 and PP5, respectively (Table 2.8). Of these values, that of PP5 was slightly higher than those of PP3 and PP4. The measured U_{x_U} of PP3 was 0.113 m/s and the reconstructed value was 0.150 m/s with a uncertainty range of $\pm$0.00508 m/s. The measured U_{x_U} of PP4 was 0.109 m/s and the reconstructed value was 0.172 m/s with a uncertainty range of $\pm$0.00147 m/s. For PP5, the measured U_{x_U} was 0.137 m/s and the reconstructed value was 0.183 m/s with a uncertainty range of $\pm$0.00451 m/s. Reconstructed U_{x_U} of PP3, PP4 and PP5 had a relatively small uncertainty range in comparison to the meausred and reconstructed values. The percent errors between reconstructed and measured U_{x_U} were 33.2% (PP3), 57.6% (PP4), and 73.7% (PP5), in which PP5 also exhibited a deviation higher than those of PP3 and PP4 (Figure 2.16B).

The measured T_d of PP3 was 740 s and the reconstructed value was 689 s with a uncertainty range of $\pm$82.5 s. The measured T_d of PP4 was 332 s and the reconstructed value

was 974 s with a uncertainty range of ±46.8 s. For PP5, the measured T_{d} was 408 s and the reconstructed value was 264 s with a uncertainty range of ±17.4 s. The percent errors between reconstructed and measured T_{d} were 7.16% (PP3), 193% (PP4), and 35.3% (PP5), of which PP4 showed a much larger deviation than PP3 and PP5. The measured C_{T,x_C} of PP3 was 0.00227 and the reconstructed value was 0.00580 with a uncertainty range of ±0.000443. The measured C_{T,x_C} of PP4 was 0.00533 and the reconstructed value was 0.00151 with a uncertainty range of ±0.000385. For PP5, the measured C_{T,x_C} was 0.00331 and the reconstructed value was 0.00564 with a uncertainty range of ±0.000342. The percent errors between reconstructed and measured C_{T,x_C} were 155% (PP3), 71.7% (PP4), and 70.1% (PP5), where PP3 showed a greater deviation than the other two experiments. The concentrations of individual grain-size classes were mostly overestimated (Figure 2.16D).

2.6 Discussion

2.6.1 Validation of DNN as an Inversion Method for Turbidity Currents Using Numerical Test Datasets

Verificaiton results using numerical datasets proved the ability of the DNN model to reasonably reconstruct the hydraulic conditions of turbidity currents from turbidites. Reconstructions of initial flow conditions and the flow duration using numerical datasets (Sections 2.5.2 and 2.5.3) were good judging from the s and B values (Tables 2.5 and 2.6). The reconstructions of the flow duration T_{d}, flow depth H_0, velocity U_0, and sediment concentrations $C_{1,0}$, $C_{2,0}$, $C_{3,0}$, and $C_{4,0}$ showed high precision (Tables 2.5 and 2.6).

Correlations between the actual and reconstructed values were observed for all parameters. Some outliers were observed for the reconstructed parameters, but most of the reconstructed values were close to the perfect reconstruction line. The range of misfit ($2s$) of all parameters was below 23.0% of the matching representative value (Tables 2.5 and 2.6). A relatively greater degree of scattering was observed for T_{d} compared to the other parameters (Figures 2.12B and 2.13B).

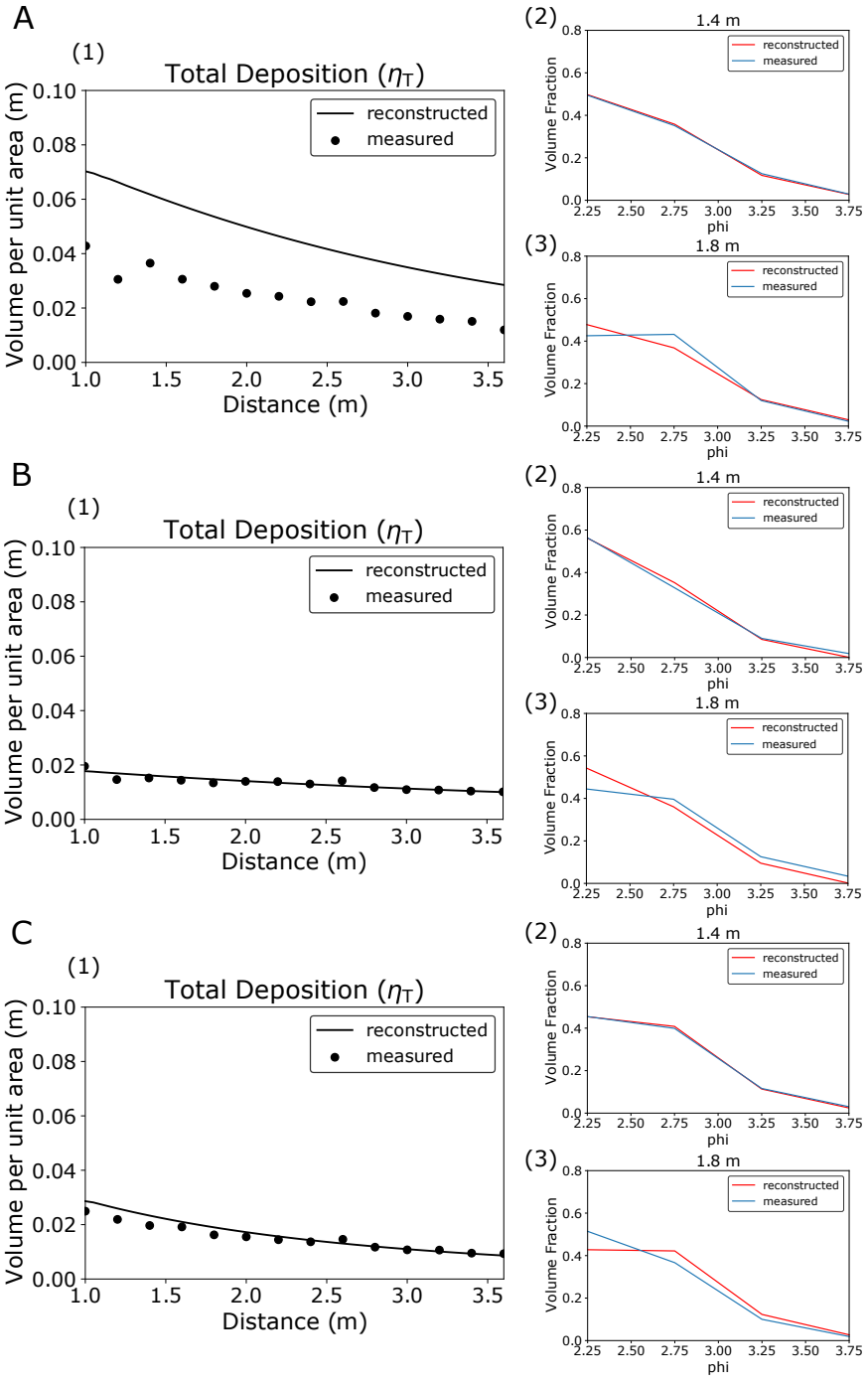

Figure 2.15: Reconstructed deposit profiles and the sampled deposit data of experiments PP3, PP4 and PP5. A. (1) Reconstructed and sampled η_T of PP3. (2) Grain size distribution at 1.4 m downstream. (3) Grain size distribution at 1.8 m downstream. B. (1) Reconstructed and sampled η_T of PP4. (2) Grain size distribution at 1.4 m downstream. (3) Grain size distribution at 1.8 m downstream. C. (1) Reconstructed and sampled η_T of PP5. (2) Grain size distribution at 1.4 m downstream. (3) Grain size distribution at 1.8 m downstream.

Table 2.8: Flow conditions measured and reconstructed for experiments PP3, PP4 and PP5. (R.: reconstructed, M.: Measured)

Parameters	PP3 R.	PP3 M.	Percent Error	PP4 R.	PP4 M.	Percent Error	PP5 R.	PP5 M.	Percent Error
C_{T,x_C}	0.00580 $\pm$0.000443	0.00227	155%	0.00151 $\pm$0.000385	0.00533	71.7%	0.00564 $\pm$0.000342	0.00331	70.1%
C_{1,x_C}	0.00142 $\pm$0.000120	0.000108	1210%	0.000379 $\pm$0.000106	0.000884	57.1%	0.00108 $\pm$0.0000556	0.000258	321%
C_{2,x_C}	0.00218 $\pm$0.000167	0.00136	59.9%	0.000534 $\pm$0.000126	0.00313	82.9%	0.00227 $\pm$0.000116	0.00210	7.80%
C_{3,x_C}	0.00149 $\pm$0.000104	0.000646	1310%	0.000420 $\pm$0.0000814	0.00109	61.5%	0.00149 $\pm$0.000124	0.000793	88.1%
C_{4,x_C}	0.000713 $\pm$0.000105	0.000157	3540%	0.000175 $\pm$0.0000716	0.000227	22.9%	0.000793 $\pm$0.0000685	0.000159	3980%
H_{x_H} (m)	0.192 $\pm$0.0145	0.149	28.8%	0.258 $\pm$0.0180	0.232	11.1%	0.126 $\pm$0.00925	0.196	35.7%
U_{x_U} (m/s)	0.150 $\pm$0.00508	0.113	33.2%	0.172 $\pm$0.00147	0.109	57.6%	0.183 $\pm$0.00451	0.137	73.7%
T_{d} (s)	687 $\pm$82.5	740	7.16%	974 $\pm$46.8	332	193%	264 $\pm$17.4	408	35.3%

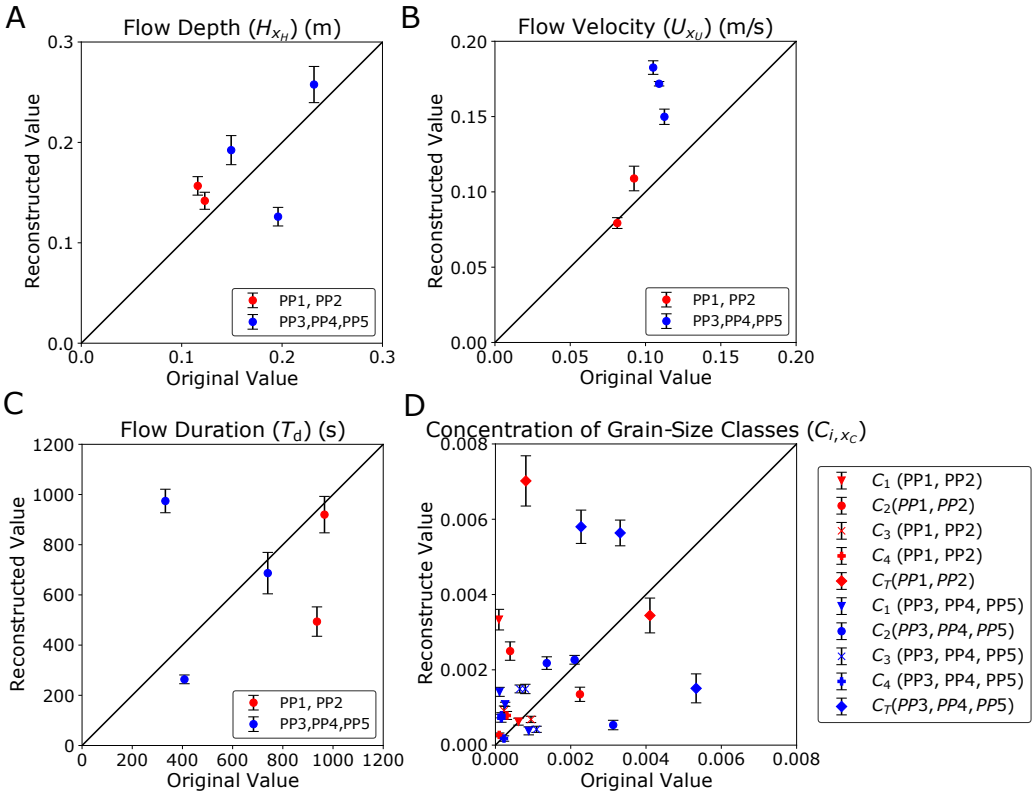

Figure 2.16: Reconstructed (with 95% confidence interval uncertainty range) vs measured flow conditions for experiments PP1, PP2, PP3, PP4 and PP5. A. Plot for H_{x_H}. B. Plot for U_{x_U}. C. Plot for T_{d}. D. Plot for C_{i,x_C}.

Concerning the estimation bias, zero was included in the 95% CI of bias for most of the parameters, proving that the reconstructed values were not significantly biased with respect to the original values. Even among parameters where statistically significant biases were detected, their deviations were minor compared with the representative values of the parameters (Tables 2.5 and 2.6). For example, in both numerical datasets of experiments conducted with 10.0% slope and 8.00% slope, the estimation bias B for T_{d} had a negative value and the range of the CI of B was below zero (Tables 2.5 and 2.6), indicating a tendency of underestimation for T_{d}. However, the bias for T_{d} was only 7.84% (10.0% slope numerical datasets) or 7.51% (8.00% slope numerical datasets) of the representative value of this parameter (630 s).

Thus, this method is suitable for estimating the paleo-hydraulic conditions of actual experimental scale turbidity currents. Correlation between reconstructed parameters and original values did not show any significant bias, implying that the inverse model developed in this study served as a high precision, high accuracy estimator of flow conditions.

2.6.2 Verification of DNN Inversion with Flume Experiment Data

As a result of inversion using the DNN model, the overall deposit profiles were reasonably reconstructed for all five experiments, and the reconstructed grain size distribution downstream matched the sampled values from experiment deposits (Figures 2.14 and 2.15). The DNN model as an inverse method tries to find the combination of hydraulic conditions that best produces the inputted deposit profiles. The fact that the reconstructed hydraulic conditions reproduced the deposit profiles used for inverse analysis indicated the DNN inverse model performed well.

For the hydraulic conditions and flow duration, a good match was observed for H_{x_H} for all five experiments with a percent error under 36.0% (Tables 2.7 and 2.8). Flow duration T_{d} was reasonably reconstructed for PP1, PP2, PP3, and PP5, with a percent error lower than 48.0%. Reconstructed T_{d} of PP4 had a percent error greater than 190%. The reconstructed

concentrations of each grain-size class C_{i,x_C} were mostly overestimated (Figure 2.16). The measured and reconstructed values of flow velocities U_{x_U} agreed well, especially for PP1 and PP2, with a percent error less than 18.0%. U_{x_U} reconstructed for PP3, PP4, and PP5 ranged from 33.2% to 73.7%.

The ability of the DNN model to distinguish minor differences in the characteristics of deposits was proved in the tests using numerical datasets, where a wide variety of initial conditions of flows were well reconstructed (Section 2.5.1). The fact that the reconstructed initial flow conditions by the DNN model for the 2000 artificial test datasets lay very close to the line of perfect reconstruction showed that non-uniqueness of deposit was unlikely a problem for the range of flow conditions tested in this study. According to the analysis of the results of the application of the DNN model to flume experiment data, there are three sources of deviations in the reconstruction of hydraulic conditions: (1) measurement errors during and after the experiments, (2) bias inherent in the inverse model, and (3) inaccuracy within the forward model of turbidity currents.

(1) The main source of deviation for sediment concentrations C_{i,x_C} may be inaccuracies in measurements. As shown in Figure 2.16, some of the measured concentrations C_{i,x_C} were extremely small ($< 0.1\%$), making them susceptible to minor disturbances during sampling and measurements. For extremely small values, even minor deviations appear to be large. Thus, for C_{i,x_C}, the main source of deviation may not be the reconstructed values but the measured values.

As for flow velocity U_{x_U}, the accuracy of measurement was greatly affected by the SNR during the experiments. Experiments PP3, PP4, and PP5 had relatively lower SNRs and a narrower range of reliable measurement than PP1 and PP2, with PP4 and PP5 having the lowest SNR (2.4.4). The narrower range of relaiable measurement for PP3, PP4, and PP5 resulted in ranges of vertical velocity profile without measurements. The measured values closest to the velocity maximum was used for calculation for PP3, PP4, and PP5, which could be slightly smaller than the actual value. In which case, the calculated layer-averaged

flow velocity would also be smaller than the actual value. This may be the reason that U_{x_U} of experiments PP3, PP4 and PP5 were overestimated and showed larger deviation than PP1 and PP2.

Slight deviation in the sampling and measurement of the deposits could also be a source of deviation in the eventual reconstruction. The uncertainty range for the reconstructed parameters was calculated using Jackkinfe samples of the η values measured from the experiment deposits. The width of the uncertainty range showed that slight deviation of the input η values can propagate to the output reconstructed values of H_{x_U}, U_{x_U}, C_{i,x_C}, and T_d.

(2) Regarding the inherent bias in the inverse model, the reconstructed T_d for the experiments PP1, PP2, PP3, and PP5 exhibited the same tendencies of deviation during the reconstruction using numerical test datasets. Thus, deviation in the reconstruction of T_d may be partially due to systematic error originating from the internal settings of the DNN.

(3) Inaccuracy in the forward model in describing the physical processes of turbidity currents may account for deviations of the reconstructed flow velocities from the measured values. There are several possible reasons why the reconstruction of flow velocity was not as accurate as with the other parameters, but the most probable reason is the inaccuracy of the entrainment function in describing the actual effect of entrainment in flow, considering that the exponent in the calculation of the dimensionless vertical velocity in the entrainment function was determined purely via optimization and differed greatly in previous studies [*Parker et al.*, 1987; *Garcia and Parker*, 1991; *Dorrell et al.*, 2018]. Another problem may lie in the layer averaging of flow velocity. *Dorrell et al.* [2014] had pointed out that vertical stratification of flow velocity and density fields reduces depth averaged hydrostatic pressure and enhances suspended sediment and momentum flux, proving that incorporating the effect of flow stratification can be essential for calculating turbidity currents. This research aims to verify the DNN model as a method of inverse analysis of turbidity currents. The improvement of the forward model, including entrainment function and velocity calculation, should be the next step in the inverse analysis study of turbidity currents.

A limitation of the inverse analysis is that it can only be conducted for flow that is depositional. Inverse analysis reconstructs the flow conditions from turbidite deposited by turbidity current, so the model would be unable to detect a non-depositional condition if it happened during a flow. Although unlikely in the current lab setting, there is a possibility that flow parameters cannot be reconstructed when different combinations of initial conditions produce the same deposit profile, which will be a problem to be resolved in the future when using field data. Compared to the analytical models, the shallow water model implemented provides some details of the internal structure of the flow, but also holds certain limitations due to its simplified calculation of flow dynamics. Nonetheless, the simplifications enable large batches of natural scale simulations to be performed. Overall, even though a certain amount of deviation was observed for all parameters, they mostly lie within a reasonable range and provided valuable insights into the development of flow and deposits over time.

2.6.3 Comparison of DNN with Existing Methodologies

In comparison to previous methods of inverse analysis of turbidity currents, the inversion method using the DNN model has great advantages in terms of calculation cost and reconstruction accuracy. Previous inversion methods of turbidity currents seek to optimize flow initial conditions to a particular set of data collected from turbidites, which is extremely time-consuming for application to one dataset and does not guarantee the general applicability of the methods to turbidite deposits [*Lesshafft et al.*, 2011; *Parkinson et al.*, 2017; *Nakao et al.*, 2020]. For example, a genetic algorithm used in *Nakao et al.* [2020] first initializes a population of parameters and then optimizes the population of parameters through selection and mutation. Eventually, the remaining parameters can successfully reconstruct target turbidite. However, each epoch of optimization requires the selection results from the previous epoch, and thus, the calculation of the forward model cannot be parallelized over epochs. In the adjoint method used by *Parkinson et al.* [2017], control variables within

the forward model of turbidity currents are first initialized and inputted into the numerical model. The turbidite deposit profile is calculated and compared with the target values using a cost function. Gradients of the cost function (objective function) for control variables are calculated analytically. If the result is not optimal, the adjoint model will run, and control variables will be adjusted by descent method. The adjusted control variables will be re-inputted into the numerical model. This cycle is repeated until the reconstructed deposit profile is judged to be optimal. Thus, the iteration of calculation cannot be performed simultaneously. In contrast, the DNN model explores the general functional relationship between turbidite deposited and flow, allowing its applicability to turbidity currents in general. The forward model calculation to generate training datasets can be perfectly parallelized, thereby significantly reducing the amount of calculation time.

Since the parallelization of the forward model calculation significantly reduced the calculation time, a more accurate and realistic forward model with a heavier calculation load could implemented. As a result, the forward model used in this research is much better at capturing the spatio-temporal evolution of turbidity current than the forward model used in previous research [*Falcini et al.*, 2009; *Parkinson et al.*, 2017]. *Falcini et al.* [2009] used a steady flow forward model, whereas our forward model is a non-steady flow model that reproduces the evolution of flow over time. The method implemented in *Parkinson et al.* [2017] omitted the effect of entrainment, which is a significant part of sediment transport in turbidity currents. As a result, their reconstructed values of flow depth, concentration, and grain diameter of the turbidite were 2.56 km, 0.0494%, and 103 μm, respectively [*Parkinson et al.*, 2017]. Compared to the objective values collected from the turbidite deposits, these values showed great deviations. In contrast, our predictions closely agreed with the original values and the effect of sediment suspension was incorporated in our forward model. Another improvement from previous research is that the forward model used in this study applies to turbidite datasets of multiple grain-size classes.

Lesshafft et al. [2011] proposed a method based on direct numerical simulation (DNS)

of the Navier-Stokes equations. However, the calculation costs of the method were extremely high, making it impractical to apply the method to natural scale turbidites. The computational cost of DNS was scaled to Re^3, thereby limiting the effectiveness of DNS to only experimental scale flows [*Biegert et al.*, 2017]. As a result, the maximum value of Reynolds number attained in previous numerical simulation using DNS was 15,000 [*Cantero et al.*, 2007], which corresponds to 3.0 cm/s for flow velocity and 50 cm for the flow depth. Thus, their methodology cannot be applied to natural scale turbidites.

2.7 Conclusions

In this study, a new method for the inverse analysis of turbidites using a DNN model was verified with actual flume experiment data. Compared to previous methods, the DNN model proved to be an efficient method for the inverse analysis of turbidity currents without compromising reconstruction accuracy. The DNN model performed well for verification using numerical datasets, judging by the standard deviation and bias of the reconstructed parameters. In terms of the application of the DNN model to experiment data, deposit profiles were well reconstructed; however, the initial flow conditions did not match the measured values perfectly. The uncertainty range of 95% confidence interval was determined for the reconstructed values of the experiment datasets using Jackknife resampling method.

The reconstructed and measured flow depths H had percent error that is less than 36.0%, which is low for the inverse analysis results. The inverse analysis result for flow duration T_d had a percent error ranging from 4.76% to 35.2%, except for PP4, which had a percent error of 193%. Flow velocity U was well reconstructed for experiments PP1 and PP2 (percent error 2.38% and 17.9%) and showed greater deviation for PP3, PP4, and PP5 (percent error 33.2%-73.7%). The reconstructed values for flow concentration of the ith grain-size class C_i had percent errors ranging from 1.79% to greater than 300%.

Overall, the DNN model exhibited good performance for the inversion of numerical

datasets and some parameters of the experiment data. The deposit profiles were well reconstructed, demonstrating the success of the DNN model in exploring the functional relationship between the initial conditions of flow and resulting deposits. The verification results with numerical datasets and flume experiments reveal that the implemented forward model is competent in performing inverse analysis on turbidity currents, but it needs to be more robust for application to a wide range of flow conditions. Improvement of the forward models and parameters, such as the entrainment function, will be a top priority in the future. The DNN's hyperparameter settings and internal structure also have room for improvement, judging from the inversion result using numerical datasets. The application of the DNN model to field datasets will be the eventual goal.

Acknowledgements

Contents of this chapter was published in the Journal of Geophysical Research: Earth Surface.

Chapter 3

Inverse Analysis of Turbidites from the Anno Formation, Chiba, Japan Using the DNN Model

Abstract

This study performed an inverse analysis of a turbidite bed using data from 9 outcrops in the Pliocene Anno Formation. A preestablished DNN inverse model alongside a 2D shallow-water forward model was used for the inverse analysis. The goal is to reconstruct the flow conditions of the ancient turbidity current that deposited the turbidite. The Pliocene Anno Formation is distributed in the southern part of Boso Peninsula, Chiba, Japan. It is a forearc basin-fill deposit consisting mainly of alternation of fine-grained turbidites and hemipelagic deposits. A series of tuff marker beds can be observed within the Anno formation, which made it possible to trace one single turbidite bed over a range of more than 25 km. Sampling from the sandstone bed correlated within the formation was conducted at 9 outcrops across a 15 km range.

Inverse analysis using the DNN model involves three steps. First, artificial outcrop datasets are generated using the 2D forward model. Then, training of DNN is performed using the artificial outcrop datasets. Finally, inverse analysis of artificial outcrop datasets and actual sampled outcrop data are conducted using the trained DNN. The viability of this reconstruction was tested with artificial outcrop datasets and the reconstructed flow

conditions were very high in accuracy. This proves that the DNN inverse model along with the 2D shallow-water forward model can potentially provide an accurate reconstruction of the flow conditions of turbidity currents from the 9 outcrops of turbidites. The reconstructed time evolution of flow depth, velocity, and concentration distribution, and the deposit profile can be used to estimate the scale of flow that occurred in the past. The reconstructed deposit profile was precise in the southern region, where the deviation of total deposit thickness was around 0.15 m for one location and smaller than 0.1 m for the other locations. Deviation in the northern region, especially near the channel outlet, where the deviation in total thickness was around 0.2 m. The reconstructed paleocurrent direction was close to the direction indicated by outcrop observation.

3.1 Introduction

An inverse analysis method for turbidity currents using deep learning neural network was proposed in *Naruse and Nakao* [2021] and verified by flume experiments in *Cai and Naruse* [2021]. The model applied to tsunami deposits in *Mitra et al.* [2021] and successfully reconstructed the inundation depth and deposit thickness from the 2014 Indian Ocean tsunami. As a method that proved useful in reconstructing the flow conditions and characteristics of the entire turbidite using only a few samples within the turbidite, it is optimistic that this method may be able to reconstruct the ancient turbidites in its entirety from the limited number of outcrops exposed. In this study, the DNN inverse model was applied to a turbidite bed from the Anno Formation located in the Boso Peninsula, Chiba, Japan. To perform inverse analysis on a turbidite deposited in nature, it was necessary to sample from multiple points within the same turbidite across a wide area. The Anno Formation contains many tuff key beds that made tracing a single turbidite over a range of 15 to 20 km possible [*Ishihara and Tokuhashi*, 2001], an ideal condition for the sampling of datasets for inverse analysis using the DNN model.

Other than the basic criteria for inverse analysis, the correlation of a single turbidite over distance, there exists another difficulty in the application of the DNN model to outcrop datasets. The precise topography during the deposition of the turbidite, an important factor in determining the characteristics of turbidite, remains unknown. For verification of the DNN model using flume experiments in *Cai and Naruse* [2021] and for application of the model to tsunami deposits in *Mitra et al.* [2021], the inverse analysis was performed with the assumption that the topography was flat. However, basin topography in nature was known to be complicated [*Saito*, 1991]. Previous research by *Tokuhashi* [1982] indicated that a ridge existed in the center of the basin along the Kiyosumi Anticline during the deposition of the Anno Formation. Paleocurrent direction of reflected turbidites identified in the southern part region of the Anno Formation indicated a rise in the southern rim of the basin at the time of deposition. To account for the known complexity in basin topography, this study employs a two-dimensional forward numerical model instead of the one-dimensional models used in *Cai and Naruse* [2021] and *Mitra et al.* [2021]. An artificial basin was constructed in the calculation domain with a ridge and a rise in the southern rim based on the basin characteristics identified in previous studies so that the topography used for calculation resembles the unknown actual topography as much as possible.

In this study, the DNN inverse model was implemented together with a two-dimensional forward model based on the one-dimensional model implemented in *Naruse and Nakao* [2021]. The sensitivity of the forward model was tested with different topographical settings and input parameters. Artificial datasets were produced using the forward model and the DNN inverse model was trained with the artificial datasets. The trained DNN was first tested with independent sets of artificial datasets also produced by the forward model and then applied to the outcrop samples from the field survey. Parameters in the initiation region of flow were reconstructed from sampled deposits. These reconstructed values were then fed into the forward model to reconstruct the spatio-temporal evolution of the experiment. Reconstructed grain size distribution of the deposits at each outcrop location was compared

with the measured values.

3.2 Geological Settings

The Anno Formation is the Pliocene succession exposed in the central part of Boso Peninsula, Chiba, Japan and distributes across a 40 km range in the east-west direction and 7 km north-south direction (Figure 3.1) [*Ishihara and Tokuhashi*, 2001]. It is the uppermost unit of the Awa Group, which consists of deposits from the Miocene to the Pliocene. The Anno Formation conformably overlies the Kiyosumi Formation and is unconformably overlain by the Pleistocene Kazusa Group via the Kurotaki Unconformity. [*Tokuhashi et al.*, 2000].

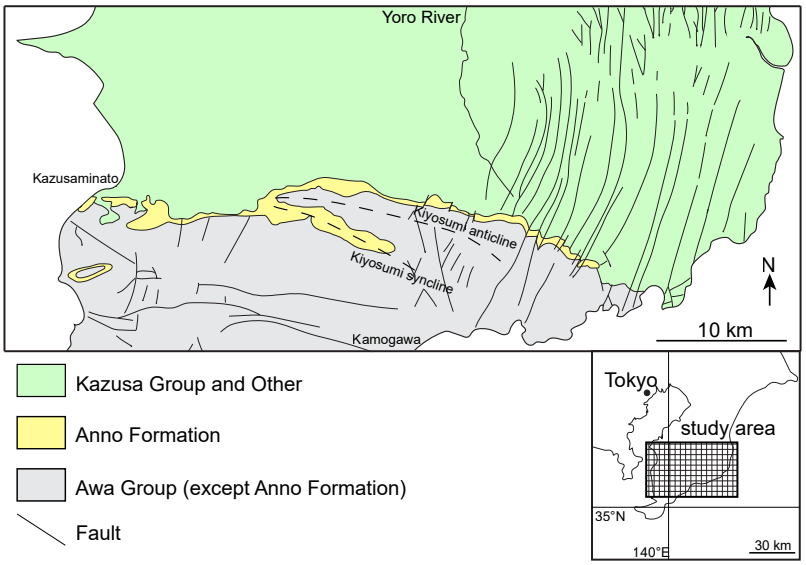

Figure 3.1: Geological map of the distribution of Anno Formation in the Boso Peninsula, Chiba Prefecture, Japan (from [*Ishihara and Tokuhashi*, 2005]).

Near the central part of Boso Peninsula, the Awa Group is exposed in three separate belt regions elongated in the west-northwest to the east-southeast direction due to the effect of the Kiyosumi Anticline and Kiyosumi Syncline. The maximum thickness of the Awa Group exposure observed was around 600 m [*Ishihara and Tokuhashi*, 2001]. An abundance of

tuff key beds within the Awa Group was reported in *Tokuhashi* [1982] and *Ishihara and Tokuhashi* [2001]. A total of 85 tuff key beds were identified for the Anno Formation, which were numbered and named An-1 to An-85 from bottom to top. No change in color, thickness, or grain size was observed for the tuff key beds observed in the Anno Formation over the exposed region, making them an ideal marker for tracing and correlating the turbidite beds that lie in between the tuff key beds [*Tokuhashi*, 1988]. Zircon fission-track age of An-49 and An-73, which lie above and below An-55, was determined to be 3.9$\pm$0.4 Ma and 3.7$\pm$0.2 Ma, respectively [*Tokuhashi et al.*, 2000], thus the age of An-55 should be in between those values.

The Awa Group was identified as forearc basin deposits formed on the landward slope of a submarine trench [*Tokuhashi*, 1982]. Within the Awa Group, both the Kiyosumi Formation and the Anno Formation were composed of interbedded turbidites and hemipelagites, where the Kiyosumi Formation was part of a sandstone-dominated submarine fan and the Anno Formation was part of a mudstone-dominated submarine fan [*Tokuhashi*, 1988]. The paleocurrent direction of the Kiyosumi Formation and the Anno Formation were from north to south for most turbidite units, but units with paleocurrent from east to west and reflected turbidites with paleocurrent direction from south to north were also identified [*Tokuhashi*, 1982; *Ishihara and Tokuhashi*, 2005]. Similar to the upper part of the Kiyosumi Formation, the paleocurrent direction of the lower part of the Anno Formation was mainly toward the east near the central part of Boso Peninsula [*Tokuhashi and Iwawaki*, 1975]. Toward the upper part of the Anno Formation, the paleocurrent direction in the eastern part of the Boso Peninsula was toward the southeast, while in the western part of the Boso Peninsula the paleocurrent direction was mainly toward the west or southwest [*Ishihara and Tokuhashi*, 2005].

For the depositional environment of the turbidite succession within Anno Formation, a shift from channel-levee system to channel-lobe transition zone was identified from the lower to the upper part of the Anno Formation through facies analysis conducted by *Ishi-*

hara and Tokuhashi [2005]. Similar to the uppermost part of the Kiyosumi Formation, a channel-levee system was identified near the central part of the Boso Peninsula for the lower part of the Anno Formation, which continues to an especially thick sedimentary succession toward the eastern part of the Boso Peninsula near the channel-lobe transition zone. For the upper part of the Anno Formation, a shift from the channel-levee system to the channel-lobe transition zone had the deposition of the thick sedimentary successions moved from the eastern to the central part of the Boso Peninsula, during which the previous channel was filled and a lobe that spread across the Boso Peninsula formed in its place. The target turbidite layer for this study lies close to the An-55 tuff key bed, which was part of the channel-lobe successions and contains mainly lobe and interlobe deposits [*Ishihara and Tokuhashi*, 2005].

3.3 Forward Model

3.3.1 Governing Equations

The forward model implemented in this study is a layer-averaged shallow water model based on *Kostic and Parker* [2006]. The model was expanded to account for multiple grain-size classes by *Nakao et al.* [2020] and *Naruse and Nakao* [2021]. This study employed a two-dimensional model developed based on the one-dimensional multiple grain-size classes model by *Naruse* [2019]. The model was chosen for its ability to retain sufficient details of the internal structure of turbidity currents while running at a reasonable calculation cost.

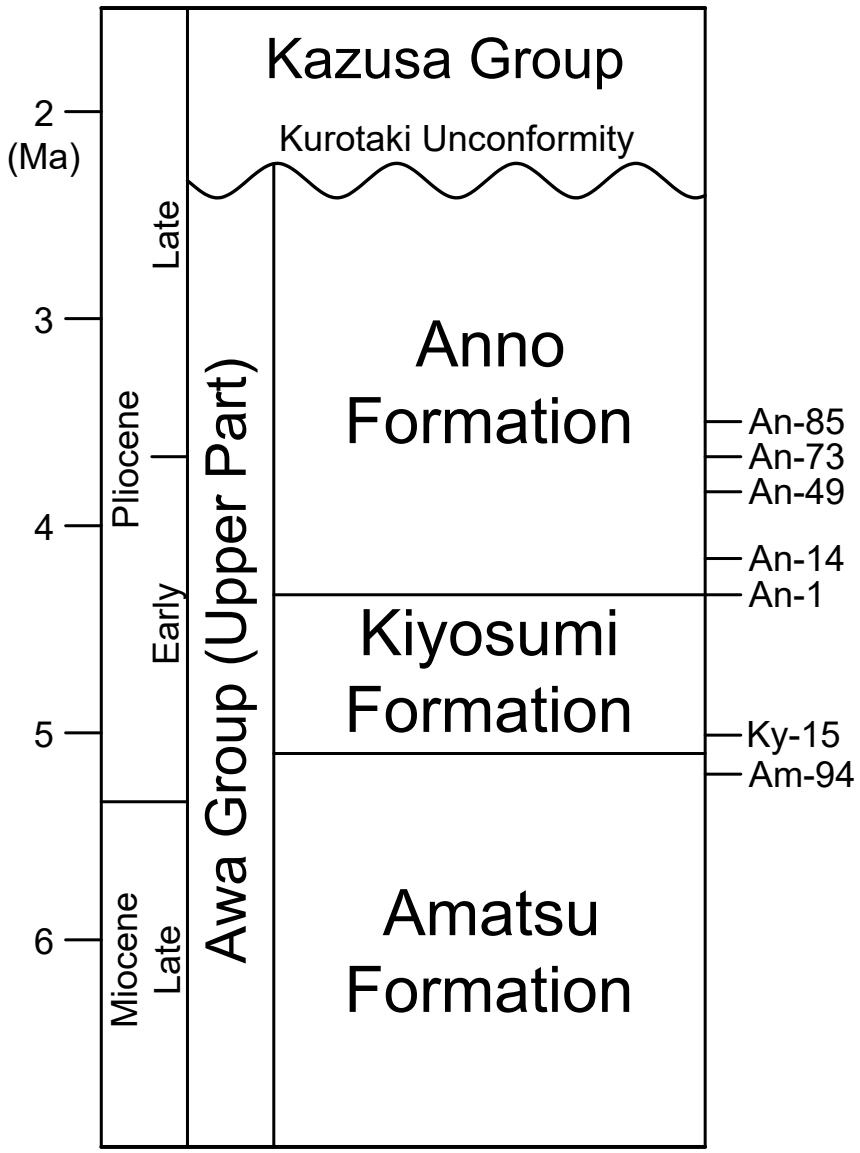

Figure 3.2: Stratigraphic column of the upper part of Awa Group, showing stratigraphic division, tuff key horizons, and geologic ages (from [*Ishihara and Tokuhashi*, 2001]).

The governing equations are as follows:

$$\frac{\partial H}{\partial t}+U\frac{\partial H}{\partial x}+V\frac{\partial H}{\partial y} = e_{\mathrm{w}}\sqrt{U^2+V^2}-H\left(\frac{\partial U}{\partial x}+\frac{\partial V}{\partial y}\right), \tag{3.1}$$

$$\frac{\partial U}{\partial t}+U\frac{\partial U}{\partial x}+V\frac{\partial U}{\partial y} = -\frac{1}{2}Rg\frac{\partial C_{\mathrm{T}}H^2}{\partial x}-Rg\frac{C_{\mathrm{T}}H}{H}\frac{\partial \eta_{\mathrm{T}}}{\partial x}-\frac{(c_{\mathrm{f}}+e_{\mathrm{w}})U\sqrt{U^2+V^2}}{H} +\nu_{\mathrm{t}}\left(\frac{\partial^2 U}{\partial x^2}+\frac{\partial^2 V}{\partial y^2}\right), \tag{3.2}$$

$$\frac{\partial V}{\partial t}+U\frac{\partial V}{\partial x}+V\frac{\partial V}{\partial y} = -\frac{1}{2}Rg\frac{\partial C_{\mathrm{T}}H^2}{\partial y}-Rg\frac{C_{\mathrm{T}}H}{H}\frac{\partial \eta_{\mathrm{T}}}{\partial y}-\frac{(c_{\mathrm{f}}+e_{\mathrm{w}})V\sqrt{U^2+V^2}}{H} +\nu_{\mathrm{t}}\left(\frac{\partial^2 U}{\partial x^2}+\frac{\partial^2 V}{\partial y^2}\right), \tag{3.3}$$

$$\frac{\partial C_iH}{\partial t}+U\frac{\partial C_iH}{\partial x}+V\frac{\partial C_iH}{\partial y} = w_i\left(F_ie_{\mathrm{s}i}-r_{\mathrm{o}}\frac{C_iH}{H}\right)-C_iH\left(\frac{\partial U}{\partial x}+\frac{\partial V}{\partial y}\right), \tag{3.4}$$

$$\frac{\partial \eta_i}{\partial t} = \frac{w_i(r_{\mathrm{o}}C_i-e_{\mathrm{s}i}F_i)}{1-\lambda_{\mathrm{p}}}, \tag{3.5}$$

$$\frac{\partial F_i}{\partial t}+\frac{F_i}{L_{\mathrm{a}}}\frac{\partial \eta_{\mathrm{T}}}{\partial t} = \frac{w_i}{L_{\mathrm{a}}(1-\lambda_{\mathrm{p}})}(r_{\mathrm{o}}C_i-e_{\mathrm{s}i}F_i), \tag{3.6}$$

where the equations represent fluid mass conservation (Equation 3.1), momentum conservation in the x-direction (Equation 3.2), momentum conservation in the y-direction (Equation 3.3), sediment mass conservation (Equation 3.4), mass conservation in bed (Equation 3.5), and sediment mass conservation in active layer (Equation 3.6).

Let x and y be the bed-attached coordinates in lateral and longitudinal directions, respectively. Variable t is time. Parameters H, U, V and C_i represent the flow depth, the layer-averaged velocity in the x-direciton, the layer-averaged velocity in the y-direciton and the layer-averaged volumetric concentration of suspended sediment of the ith grain-size class, respectively. Parameter C_{T} denotes the layer-averaged total concentration of suspended sediment ($C_{\mathrm{T}} = \sum C_i$). Parameter c_{f} is the friction coefficient. Parameter ν_{t} is the horizontal eddy viscosity, and g represents gravitational acceleration. Sediment properties are described by R, the submerged specific density of sediment, λ_{p}, the porosity of bed sediment, and w_i, the settling velocity of a sediment particle of the ith grain-size class. Parameter η_i is the sum of volume per unit area of bed sediment of the ith grain-size class

η_{si} and the topographical elevation. The sum of all η_{si} is η_{sT} ($\eta_{sT} = \sum \eta_{si}$). Parameter η_T is the sum of all η_{sT} and the topographical ($\eta_T = \sum \eta_i$) plus the topographical elevation. Parameter L_a represents the active layer thickness. Parameter F_i is the volume fraction of the ith grain-size class in active layer. Parameters r_o, e_{si}, and e_w represent the ratio of near-bed suspended sediment concentration to the layer-averaged concentration of suspended sediment, the entrainment rate of sediment of the ith grain-size class into suspension, and the entrainment rate of ambient water to flow, respectively.

3.3.2 Closure Equations

Empirical formulations from previous studies are used to solve Equations 3.1-3.6. In this study, the friction coefficient c_f is a constant value. Horizontal eddy viscosity v_t is calculated using the following equation:

$$v_t = \frac{1}{6}\kappa u_* H, \tag{3.7}$$

where κ is the Karman constant, which equals to 0.4. Shear friction velocity u_* is calculated as follows:

$$u_* = \sqrt{c_f} U. \tag{3.8}$$

The particle settling velocity w_i for each grain-size class is calculated using the relation from *Dietrich* [1982], which can be expressed as follows:

$$w_i = R_{fi}\sqrt{RgD_i}, \tag{3.9}$$

$$R_{fi} = \exp\{-b_1 + b_2 \log(Re_{pi}) - b_3[\log(Re_{pi})]^2 - b_4[\log(Re_{pi})]^3 + b_5[\log(Re_{pi})]^4\}, \tag{3.10}$$

$$Re_{pi} = \frac{\sqrt{RgD_i}D_i}{\nu}, \tag{3.11}$$

where D_i is the representative grain diameter of the ith grain-size class. Emperical constants b_1, b_2, b_3, b_4 and b_5 are 2.891394, 0.95296, 0.056835, 0,000245 and 0.000245, respectively.

Kinematic viscosity of water ν is defined as:

$$\nu = \frac{\mu}{\rho}, \tag{3.12}$$

where μ and ρ are dynamic viscosity and water density, respectively.

The entrainment coefficient of ambient water e_{w} is calculated using the empirical formula from *Fukushima et al.* [1985] as follows:

$$e_{\mathrm{w}} = \frac{0.00153}{0.0204 + Ri}, \tag{3.13}$$

with the bulk Richardson number Ri defined as:

$$Ri = \frac{RgC_{\mathrm{T}}H}{U^2}. \tag{3.14}$$

The entrainment coefficient of sediment for each grain-size classes $e_{\mathrm{s}i}$ is calculated using the empirical relation from *Garcia and Parker* [1993]:

$$e_{\mathrm{s}i} = \frac{aZ^5}{1 + (\frac{a}{0.3})Z^5}, \tag{3.15}$$

$$Z = p\alpha_1 \frac{u_*}{w_i} Re_{\mathrm{p}i}^{\alpha_2}, \tag{3.16}$$

where constant a is 1.3×10^{-7}. Emperical constant p is 1.0 for experimental scale flows and estimated to be 0.1 for natural scale flows [*Fildani et al.*, 2006]. The constants α_1 and α_2 are 0.586 and 1.23 respectively if $Re_{\mathrm{p}} \leq 2.36$. If $Re_{\mathrm{p}} > 2.36$, α_1 and α_2 are 1.0 and 0.6, respectively.

3.3.3 Implementation of Forward Model

In this study, the CIP-combined and unified procedure (C-CUP) method [*Yabe and Wang*, 1991], a third order accurate scheme, was used for integrating Equations 3.1, 3.2, 3.3, and 3.4. Neumann-type artificial viscosity was implemented with C-CUP for shock capturing with ν_a set to 0.75 [*Ogata and Yabe*, 1999]. Time step Δt was initialized to 0.1 for the first

time step, then calculated using the following equation for later time steps:

$$\Delta t = \alpha \frac{\Delta x}{\max(\max(|U| + C_s), \max(|V| + c_s))}, \quad (3.17)$$

$$c_s = \sqrt{RgC_T H}, \quad (3.18)$$

where c_s is wave celerity. Parameter α is the Courant number, which was set to 0.4 in this study. To stabilize the calculation, a second order artificial viscosity was implemented using the scheme by *Jameson et al.* [1981], where the parameter κ_a was set to 0.05. The fractional step method was used to solve Equations 3.5 and 3.6. Interval of spatial grids is the same in x- and y-direcitons ($\Delta x = \Delta y$). In this study, Δx was set to 100.0 m based on the area of interest for this study.

Based on the topographical settings of the area of interest in this research, an artificial basin with surge flow produced from a lock-exchange setting was used for calculation in this study. Specifics of the described calculation domain were illustrated in Figures 3.3A and 3.3B. As shown in the figures, the calculation domain was rectangular with W_{topo} (m) and L_{topo} (m) as the width (lateral x-direction) and the length (longitudinal y-direction). Number of grids in the x-direction, G_x, was calculated by G_x=W_{topo}/Δx. Number of grids in the y-direction, G_y, was calculated by G_y=L_{topo}/Δx. The total number of grids was G_x x G_y.

The rectangular domain was divided into a basin area with a south-dipping slope at m_b to the south and an area with a steeper south dipping slope at m_s to the north in the longitudinal direction. The change in slope (slope-basin break) occurred at a distance of L_s (m) from the southern edge of the calculation domain in the longitudinal direction. In the north region, a parabola shaped canyon cut into the steeper sloped area at a slope of m_c ($< m_s$). The canyon was centered at a distance W_{init} (m) from the western edge of the calculation domain in the lateral direction. The outlet of the canyon (canyon-basin break) was at a distance of L_c (m) ($> L_s$) from the southern edge of the calculation domain in the longitudinal direction. The half-width of the canyon at the canyon-basin break was w_c. The

basin created has smooth topography. To make it more realistic, an unevenness of $\pm n_{\mathrm{topo}}$ was added randomly to the topographical elevation within the calculation domain.

For this study, a parabolic arch-shaped ridge was added to the basin part of the calculation domain along the lateral direction based on the basin topography during the deposition of the Anno Formation explained in Section 3.2. The center of the ridge was at a distance of L_{r} (m) from the southern edge of the calculation domain in the longitudinal direction. The height of the ridge was h_{r} (m). The width of the ridge was w_{r} (m). A north dipping slope at m_{d} starting at the southern edge of the calculation domain and ending at L_{d} (m) north of the southern edge was also added. The initiation region the lock-exchange setting was a circular with radius r_{init}, height H_{init}, and concentrations of each grain size class $C_{\mathrm{init},i}$ ($C_{\mathrm{init,T}} = \sum C_{\mathrm{init},i}$) inputted as initial conditions. The location of the circular initiating region within the calculation domain was determined by W_{init} (m) and L_{init} (m), which were the distances of the center of the circular initiating region from the southern edge toward the north, and from the western edge toward the east within the calculation domain.

In this study, values of W_{topo} and L_{topo} were 15000.0 m and 20000.0 m, respectively. All four boundaries of the calculation domain was set to Neumann boundary condition. Parameters m_{b}, m_{s}, and m_{d} were set to 0.0, 0.2, and 0.0875. Parameters L_{s} and L_{d} were 10000.0 m and 500.0 m, respectively. Canyon related parameters m_{c}, L_{c}, W_{init}, and w_{c} were 0.05, 10200.0 m, 7500.0 m, and 1000.0 m. The noise parameter n_{topo} was 0.01 m. Ridge related parameters L_{r} and w_{r} were 5000.0 m and 500 m. Calculations were conducted for ridge height h_{r} set to 25 m and 50 m. The position of initiation region of flow had W_{init} and L_{init} set to 7500.0 m and 15000.0 m, respectively.

Parameter $F_{i,0}$, the initial volume fraction of the ith grain-size class in active layer, was set to 1/N for all grain-size classes, where N represents the number of grain-size classes. Other than the initiating region, all other grids had flow parameters initialized to zero. The wet-dry boundary condition at the head of the flow was conducted using the scheme proposed by *Yang et al.* [2016]. Threshold values of $C_T H$ and H, ε and H_{w}, was used to

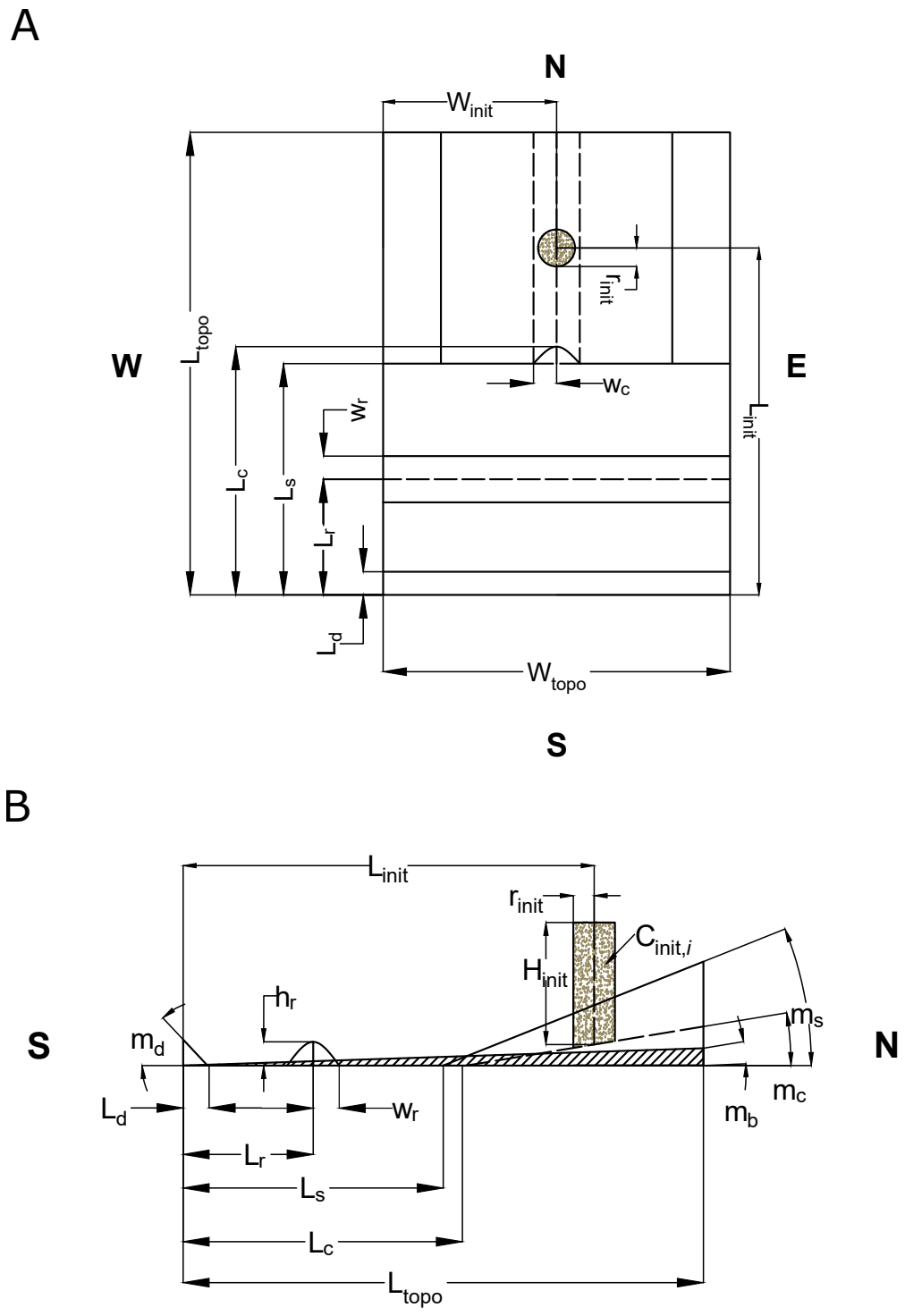

Figure 3.3: A. A top view schematic diagram of the aritificial basin used in this study. B. A side view schematic diagram of the artificial basin.

determine the position of the waterfront. If $C_T H \geq \varepsilon$ and $H \geq H_{\mathrm{w}}$, the grid was wet. If and $H < H_{\mathrm{w}}$ or $C_T H < \varepsilon$, the grid was dry. In this study, ε and H_{w} was set to 0.00001 and 0.001, respectively. A dry grid adjacent and downstream to a wet grid was a partial wet grid. Flow discharge M at a partial wet grid j was calculated using Homma's equation [*Yang et al.*, 2016] as follows:

$$M = C_{\mathrm{s}} H_{j-1} \sqrt{R g C_{\mathrm{T},j-1} H_{j-1}}, \tag{3.19}$$

where the discharge coefficient C_s is equal to 0.35.

The number of grain-size classes and representative grain diameter D_i for each grain-size class were determined on the basis of the grain size distribution measured from samples. In this study, the number of grain-size classes was 4 and D_i for grain-size classes 1, 2, 3, 4 were 250, 125, 62.5, and 31.3 μm, respectively. The density of the surrounding fluid ρ_{f} was set to 1000.0 kg/m^3 in this study. The submerged specific density of sediment $R = (\rho_{\mathrm{s}} - \rho_{\mathrm{f}})/\rho_{\mathrm{f}}$, where ρ_{s}, the density of sediment particles, is 2.65 g/cm^3. The porosity of bed sediment λ_{p} was assumed to be 0.4. The friction coefficient c_{f} was set to 0.004 and the ratio of near-bed concentration to layer-averaged values r_{o} was set to 1.5 [*Kostic and Parker*, 2006]. Dynamic viscosity μ Pa·s was 0.00101, an experimentally determined of μ at 20.0°C [*Rumble*, 2018]. Constant p for the calculation of $e_{\mathrm{s}i}$ is 0.1 in this study, since the calculation will be conducted with a field scale setting [*Fildani et al.*, 2006]. In addition, the thickness of active layer L_{a} was set to be a constant, 0.01 m. The gravitational acceleration g was 9.81 m/s^2.

3.3.4 Sampling from Forward Model Simulations

Numerical simulations were performed using the two-dimensional model described in Section 3.3. The simulations were conducted with an artificial bain topography constructed based on the depositional environment of the Anno Formation indicated by previous research (Section 3.2). The location and dimensions of the calculation domain relative to the

actual Anno Formation distribution and sampled outcrop locations are shown in Figure 3.4, where the calculation domain north was rotated 10 degrees to the east to align the ridge with the Kiyosumi Anticline. Specifics of the calculation domain of simulations conducted in this study are explained in Section 3.3.3. Turbidity current flow characteristics over the predetermined topography served as a comparison with field observations. Deposits from forward model simulations were sampled at grids that correspond to the outcrop locations on map (Figure 3.4).

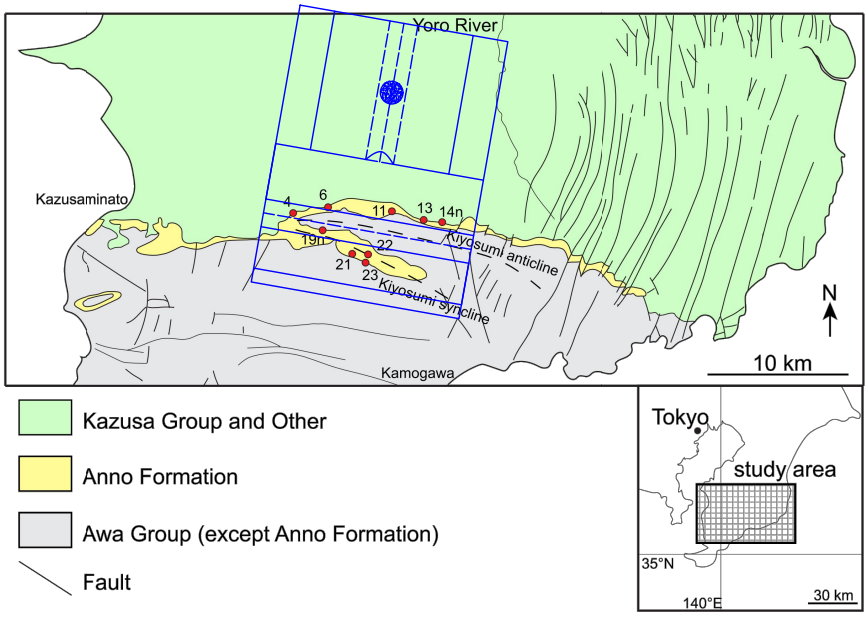

Figure 3.4: A map showing the outcrop locations within Anno Formation and the calculation domain in relation to the outcrops.

3.4 Inverse Analysis by Deep Learning Nerual Network

In this study, inverse analysis of outcrop samples was conducted using a DNN model proposed by [*Naruse and Nakao*, 2021]. Specifics concerning the structure of DNN implemented were done based on [*Cai and Naruse*, 2021]. As described in Chapter 2 Section 2.3, inverse analysis using DNN consists of four steps. First, artificial datasets of turbidity currents were produced using a forward model. Then, the DNN model was trained using the

datasets. After that, the trained DNN model was applied to a separate artificial dataset also produced using the forward model to test its performance for the reconstruction problem proposed. Finally, after performance proved to be good when tested with artificial datasets, the trained forward model was applied to the actual data measured from outcrop samples.

3.4.1 Production of Training Datasets

The training dataset for this study was a combination of randomly generated values for the parameters of the initiation region of flow in numerical simulations. A program in Python was written to generate sets of initial flow conditions. Each set of values generated consists of an initiation region height H_{init}, a radius of initiation region r_{init}, and the concentrations of each grain-size class in the initiation region $C_{\mathrm{init},i}$ (Figure 3.3). Other variables, such as the position of the initiation region, were set to constant values.

The forward model calculates the deposited turbidite distribution and thickness within the artificial basin using randomly generated initial conditions. The deposited turbidite was calculated as thickness without porosity at 9 locations within the calculation domain. The calculation domain was divided into G_{x} times G_{y} number of grids, where data points of deposits at grids are akin to sampled data from outcrops of an actual turbidite. Table 3.1 illustrates the ranges of randomly generated initial conditions. These ranges were decided based on possible values that can be observed in natural scale turbidity currents. In this study, 2000 training datasets were used for training and 100 datasets were used for verifying the DNN (Section 3.5.2). The number of test datasets was chosen to be the same number as that of validation datasets. The test numerical datasets for verification were generated independently from the training datasets.

3.4.2 DNN Inverse Model Settings

The DNN inverse model was implemented using the same structure as in [*Cai and Naruse*, 2021], but with different input nodes, output nodes, and hyperparameter settings. In this

Table 3.1: Range of initial flow conditions generated for production of training datasets.

Parameter	Minimum	Maximum
H_{init} (m)	50.0	1000.0
r_{init} (m)	100.0	900.0
$C_{\mathrm{init},i}$	0.005	0.2

study, nodes in the input layer held deposit values, i.e., the deposit thickness for all grain-size classes at spatial grids. Nodes in the output layer held estimates of parameters to be reconstructed, which in this case are H_{init}, r_{init}, and $C_{\mathrm{init},i}$. Hyperparameters dropout rate, validation split, and momentum for the DNN model were set to 0.5, 0.2, and 0.9, respectively. The learning rate was set to 0.01. The batch size was set to 32 and the number of layers was set to 5. The number of nodes in each layer was 2000. Epoch was 20000. Calculations were performed using GPU NVIDIA GeForce GTX 1080 Ti.

3.4.3 Evaluation of Trained DNN Model

For the evaluation of the DNN model with artificial datasets (Section 3.5.2), the reconstruction result of each parameter was evaluated using bias (B) and sample standard deviation (s) of residuals. The calculations were performed using the following equations:

$$B = \frac{\sum x_i}{n}, \tag{3.20}$$

$$s = \sqrt{\frac{\sum (x_i - B)^2}{n-1}}, \tag{3.21}$$

where n represents the number of test datasets, and x_i denotes the residual of the specific reconstructed parameter for the ith test dataset. The value of s for each reconstructed parameter was compared with a representative value C_v^*, which is the mid-value over the range in which the specific parameter was generated (Table 3.1). The confidence interval of B was determined using the bootstrap resampling method [*Davison and Hinkley*, 1997]. Resampling of B was conducted 1000 times, and the 95% confidence interval (CI) of B was determined.

During the application of the DNN model to outcrop data (Section 3.5.3), flow parameters at the initiation region of the simulation were reconstructed from the measured properties of the outcrop samples at 9 locations. The reconstructed parameters were inputted into the forward model so that downstream flow parameters and the time evolution of the flow and deposition were calculated. The calculated deposit properties at the locations corresponding to those of the outcrop samples (Figure 3.4) were compared with the sampled data. The accuracy of reconstruction for outcrops was quantified by the root mean squared error, which is defined by the formula below:

$$J = \frac{\sum x_{\mathrm{m}} - x_{\mathrm{r}}}{n}, \tag{3.22}$$

where x_{m} represents the measured value and x_{r} represents the reconstructed value.

3.4.4 Preparing Outcrop Datasets for Inversion

Samples were collected at 9 outcrop locations for the target layer q_t used in this study. The coordinates of outcrops measured by the handy GPS are listed in Table 3.2. Grain size analysis was conducted for all samples. Procedures for the analysis of samples from outcrop numbers 14n and 19n were different from the other samples since they were collected recently while others were sampled and measured in the past.

For samples from outcrops 14n and 19n, loosely compacted sediment samples were taken from turbidite sand beds at the outcrops. Each sample was placed in a drying dish and placed on a hot plate heated at 100 °C. A solution of 10.0% hydrogen peroxide was then added to each drying dish to remove organic contents from sample sediments. Hydrogen dioxide reacts with organic contents through an oxidization process, during which oxygen and water are produced as byproducts. When organic contents were present, the solution in drying dishes will produce air bubbles as oxygen was released. Hydrogen peroxide solution was added several times to each drying dish until the release of air bubbles comes to a halt. After that, samples were placed in an ultrasonic cleaning machine with water and

mixed with sodium hexametaphosphate as a release agent to remove mud contents. After removing organic and mud contents, dried in a drying oven at 70 °C. Grain size distribution analysis was then conducted for the dried samples.

For samples other than 14n and 19n, samples obtained from outcrop were first dried at 80 °C for 48 hours. The dried samples were weighed and then washed in an ultrasonic cleaning machine for 200 minutes to soften the sediments. The softened sediments were sieved with a 63 μm to separate mud from coarse sediments. After that, the coarse sediments were again dried at 80 °C for 48 hours. The dried weight of coarse sediments was weighed. The weight of the sample was initially measured and the weight of dried coarse sediments was used to calculate the percentage of mud contents within the sample. Dried coarse sediment, which consists of almost entirely sand-sized particles, was used for grain size distribution analysis.

A settling tube was used to conduct the grain size distribution analysis. The settling tube used was 1.8 m in length. The calculation of grain size distribution was performed using STube [*Naruse*, 2005]. Particle settling velocity was calculated using *Gibbs* [1974]. The measured grain size distribution of sediment was discretized to four grain-size classes. The representative grain diameter of grain-size classes 1, 2, 3, and 4 were set to be 250, 125, 62.5, and 31.3 μm, respectively. For samples other than 14n and 19n, the calculated value for mud contents was considered as part of grain-size class 4, the finest grain size class.

Table 3.2: A list of outcrops sampled and measured for this study.

Outcrop Number	Latitude	Longitude
4	35.21388889	139.9908333
6	35.215	140.0436111
11	35.20833333	140.1041667
13	35.21111111	140.125
14n	35.205872	140.134458
19n	35.202104	140.013112
21	35.1875	140.0354
22	35.18194	140.0458
23	35.18694	140.0478

3.5 Results

Results of numerical experiments and inverse analysis were plotted along the lines shown in Figure 3.5. Lines A-A' and B-B' runs west to east at positions 7500 m and 2500 m north of the southern edge of the calculation domain. Line C-C' runs north to south at 7500 m east of the western edge of the calculation domain. Section 3.5.1 contains sensitivity tests of forward model with different input flow parameters and different ridge height in the artificial basin topography. The resulting deposits were plotted along lines A-A', B-B', and C-C'. Section 3.5.3 contains inverse analysis of outcrop datasets sampled from field survey. The resulting deposits were also plotted along lines A-A', B-B', and C-C'.

3.5.1 Numerical Experiments

Sensitivity Tests of Forward Model with Different Flow Parameters

The degree of sensitivity of the forward model to changes in the initial conditions of the flow and model parameters was tested (Table 3.3) with ridge height h_r set to 25 m and 50 m. The results for h_r = 25 m are shown in Figures 3.6, 3.7, and 3.8. The results for h_r = 25 m are shown in Figures 3.9, 3.10, and 3.11. Numerical simulations were conducted with different values of the six parameters H_{init}, r_{init}, $C_{init,T}$, c_f, r_o, and e_s. H_{init}, r_{init}, and $C_{init,T}$ values in Case 1 contains the mid-values over the range of H_{init}, r_{init}, and $C_{init,T}$ for generating training data (Table 3.1). Values for c_f, r_o, and e_s in Case 1 were the constants used for all other numerical experiments performed in this study. Overall, similar trend was observed for h_r = 25 m and h_r = 50 m.

The results of the sensitivity tests revealed that changes in the deposit profile occur when the initial flow conditions differ (Figure 3.6A,B,C, 3.7A,B,C, 3.8A,B,C, 3.9A,B,C, 3.10A,B,C and 3.11A,B,C). Along A-A', B-B', and C-C', the volume of the deposited sediment increased overall as H_{init} increased (Figure 3.6A, 3.7A, 3.8A, 3.9A, 3.10A, and 3.11A). The same trend was observed for r_{init} and $C_{init,T}$ (Figure 3.6B,C, 3.7B,C, 3.8B,C,

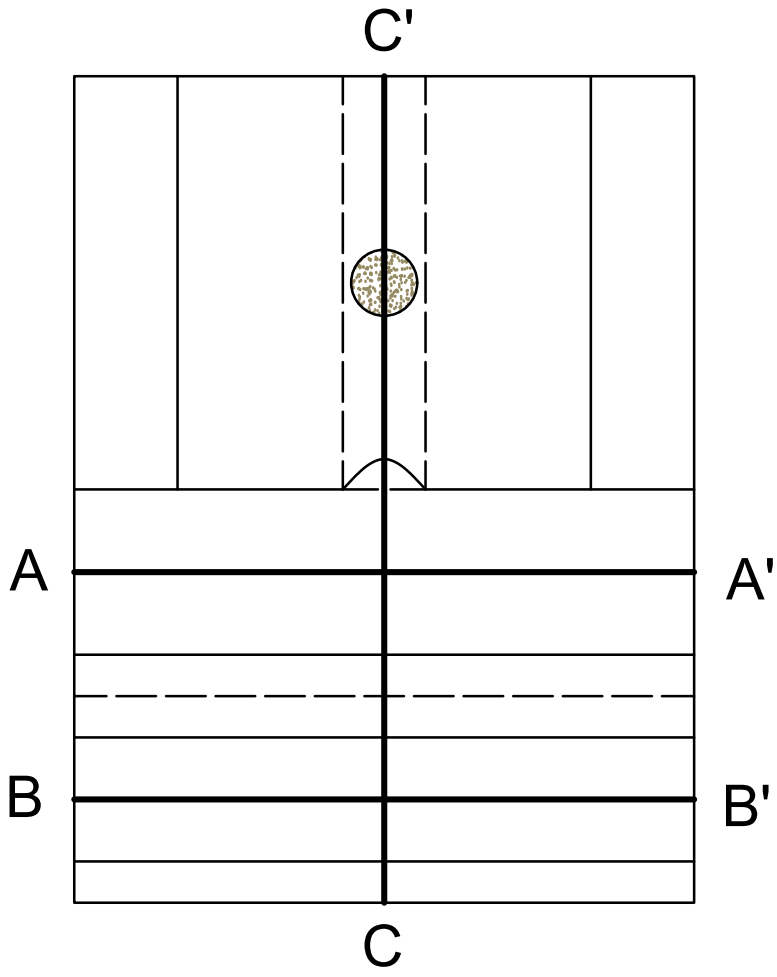

Figure 3.5: A diagram showing lines A-A', B-B', and C-C', along which the results of numerical experiments and inverse analysis were plotted in the following sections.

3.9B,C, 3.10B,C, and 3.11B,C). Among these three parameters, the amount of increase in the volume per unit area of deposit was greatest for r_{init}, and smaller for H_{init} and $C_{\mathrm{init,T}}$ along A-A', B-B', and C-C'. Increase in thickness of deposit observed for $C_{\mathrm{init,T}}$ was greater than H_{init} at A-A', but was about the same along B-B' (Figures 3.6A,C, 3.7A,C, 3.9A,C and 3.10A,C). For $C_{\mathrm{init,T}}$, a greater increae in thickness of deposit was observed upstream than downstream the ridge (Figures 3.8C, and 3.11C). H_{init} and r_{init} showed an opposite trend, where a greater increae in thickness of deposit was observed downstream (Figures 3.8A,B, and 3.11A,B).

Concerning model closure parameters, the resulting deposit profile along A-A' showed a small amount of increase in thickness at the center as the entrainment rate e_{s} increase. The amount of increase in thickness gradually decreases towrad the west and east boundary and changed to a decrease at around 45 m away from the center (Figure 3.6F). The opposite pattern was observed for the ratio of near-bed to the layer-averaged supsended sediment concentrations r_{o}, where a decrease in thickness at center was observed as r_{o} increased. The amount of decrease gradually gets smaller toward the west and east boundary and became an increase at around 25 m away from the center (Figures 3.6E and 3.9E). Along B-B', almost no change in deposit thickness was observed for different values of r_{o} and e_{s} (Figures 3.7E, F and 3.10E, F). As for the friction coefficient c_{f}, an increase in thickness of deposit was observed for increase in c_{f} along A-A' (Figures 3.6D and 3.9D). For $h_{\mathrm{r}} = 25$ m, a decrease in deposit thickness was observed as c_{f} increased from 0.004 to 0.01, but as c_{f} increased from 0.001 to 0.004, a increase was observed toward the center, which gradually changed to a decrease toward the west and east boundary (Figure 3.7D). For $h_{\mathrm{r}} = 50$ m, a decrease in deposit thickness was observed as c_{f} increased (Figure 3.10D)

Along C-C', deposit thickness increased as r_{o} increased, but the increase gradually became a decrease toward the south boundary. At around 40 m upstream of the south boundary, deposit thickness showed decreasing trend as r_{o} increased (Figures 3.8E and 3.11E). e_{s} again showed an opposite trend, where deposited thickness decreased as e_{s} increased. The

trend reversed to a increase in deposit thickness with increase in e_s at 20 m upstream of the south boundary (Figures 3.8F and 3.11F). For c_f, deposit thickness increased as c_f increased along C-C', but Case 9 with c_f = 0.001 showed a sharp increase at around 40 m upstream of the south boundary. Deposit thickness of Case 9 surpassed those of the other two cases south of the 40 m point (Figures 3.8D and 3.11D).

Table 3.3: Settings for sensitivity tests of forward model with different flow parameters.

Case	H_{init} (m)	r_{init} (m)	$C_{init,T}$	c_f	r_o	e_s
1	500.0	500.0	0.4	0.004	1.5	GP
2	750.0	500.0	0.4	0.004	1.5	GP
3	250.0	500.0	0.4	0.004	1.5	GP
4	500.0	750.0	0.4	0.004	1.5	GP
5	500.0	250.0	0.4	0.004	1.5	GP
6	500.0	500.0	0.6	0.004	1.5	GP
7	500.0	500.0	0.2	0.004	1.5	GP
8	500.0	500.0	0.4	0.01	1.5	GP
9	500.0	500.0	0.4	0.001	1.5	GP
10	500.0	500.0	0.4	0.004	2.0	GP
11	500.0	500.0	0.4	0.004	1.0	GP
12	500.0	500.0	0.4	0.004	1.5	GPx2
13	500.0	500.0	0.4	GP	1.5	GPx0.5

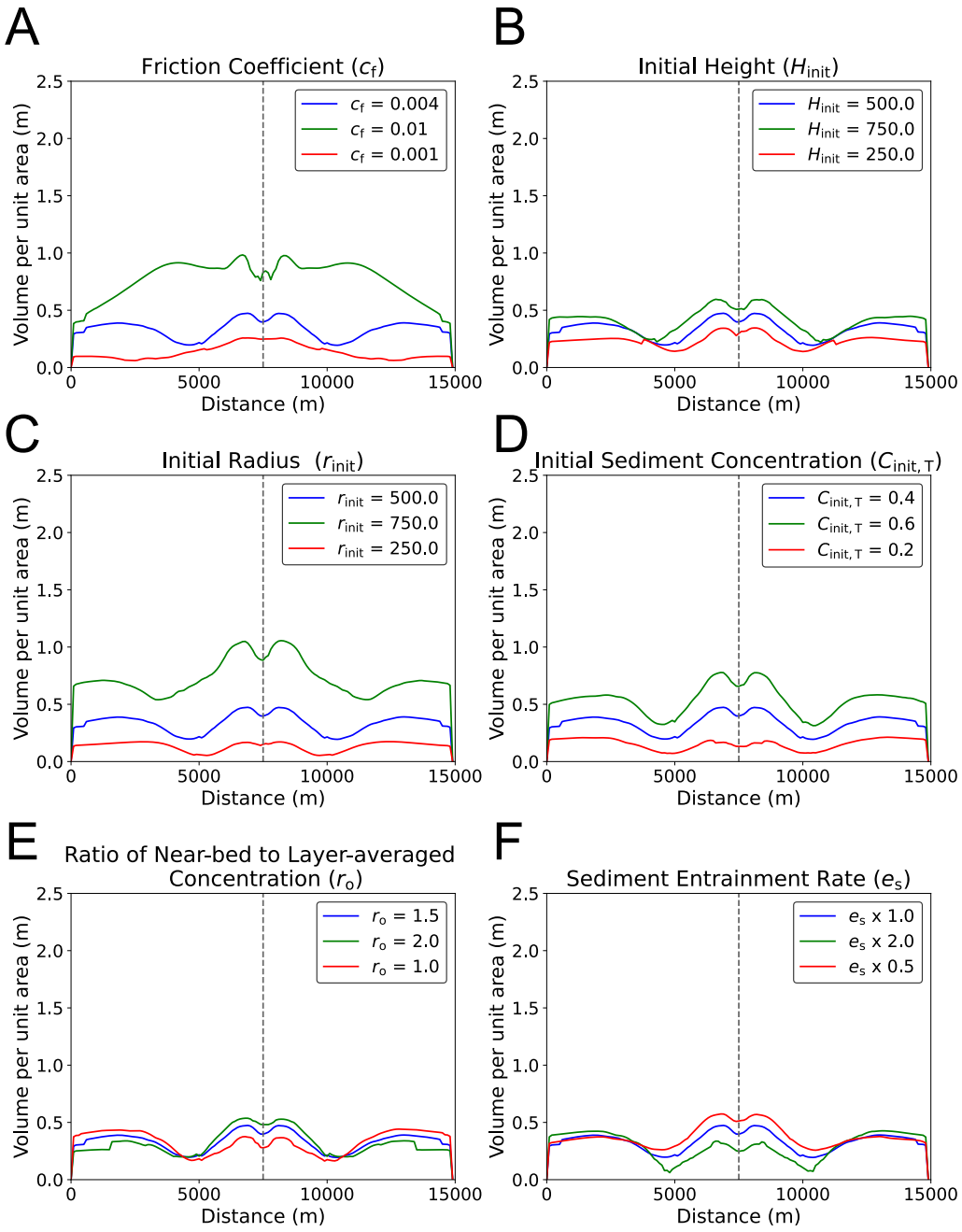

Figure 3.6: Sensitivity tests of deposit profile of numerical turbidites to change in initial flow conditions and closure parameters along A-A' with h_r set to 25 m (Table 3.3). The gray dotted line indicates the center of the channel outlet into basin. A. Dependency on initation region height H_{init}. B. Dependency on initiation region radius r_{init}. C. Dependency on initiation region total sediment volumetric concentration $C_{T,0}$. D. Dependency on friction coefficient c_f. E. Dependency on the ratio of near-bed to layer-averaged concentration r_o. F. Dependency on sediment entrainment rate e_s.

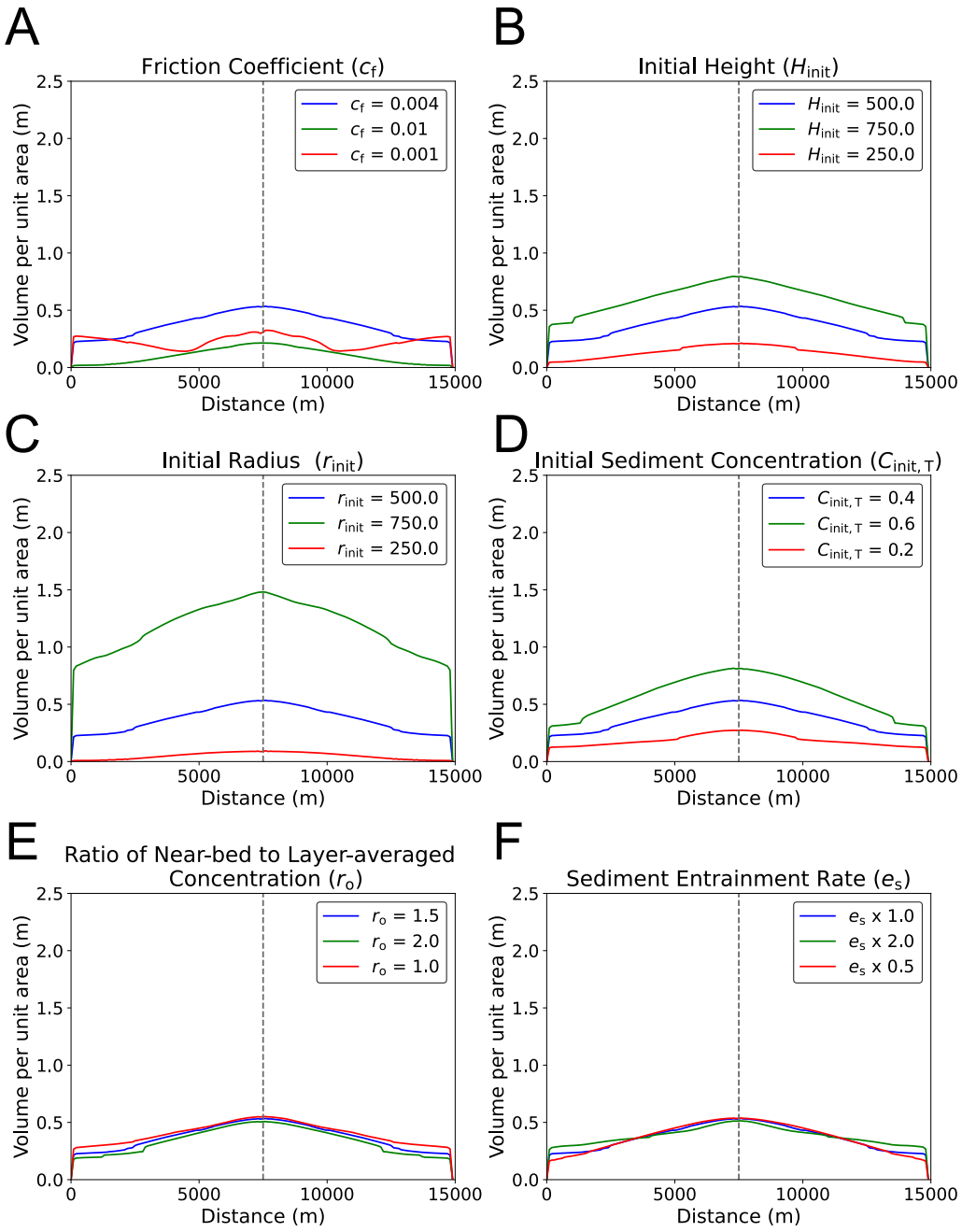

Figure 3.7: Sensitivity tests of deposit profile of numerical turbidites to change in initial flow conditions and closure parameters along B-B' with h_r set to 25 m (Table 3.3). The gray dotted line indicates the center of the channel outlet into basin. A. Dependency on initation region height H_{init}. B. Dependency on initiation region radius r_{init}. C. Dependency on initiation region total sediment volumetric concentration $C_{T,0}$. D. Dependency on friction coefficient c_f. E. Dependency on the ratio of near-bed to layer-averaged concentration r_o. F. Dependency on sediment entrainment rate e_s.

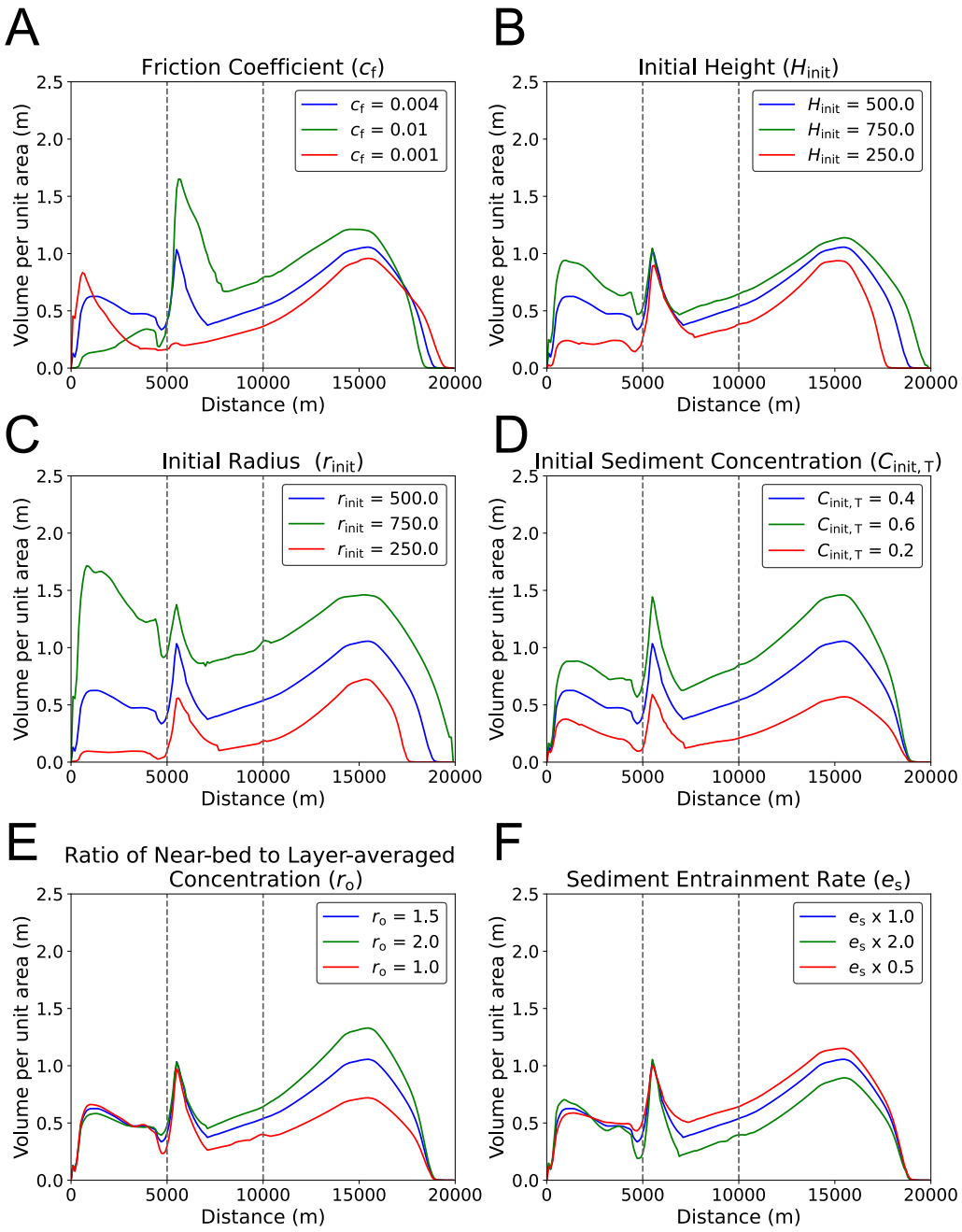

Figure 3.8: Sensitivity tests of deposit profile of numerical turbidites to change in initial flow conditions and closure parameters along C-C' with h_r set to 25 m (Table 3.3). The gray dotted line on left indicates the center of the ridge. The gray dotted line on right indicates the canyon-basin break. A. Dependency on initation region height H_{init}. B. Dependency on initiation region radius r_{init}. C. Dependency on initiation region total sediment volumetric concentration $C_{T,0}$. D. Dependency on friction coefficient c_f. E. Dependency on the ratio of near-bed to layer-averaged concentration r_o. F. Dependency on sediment entrainment rate e_s.

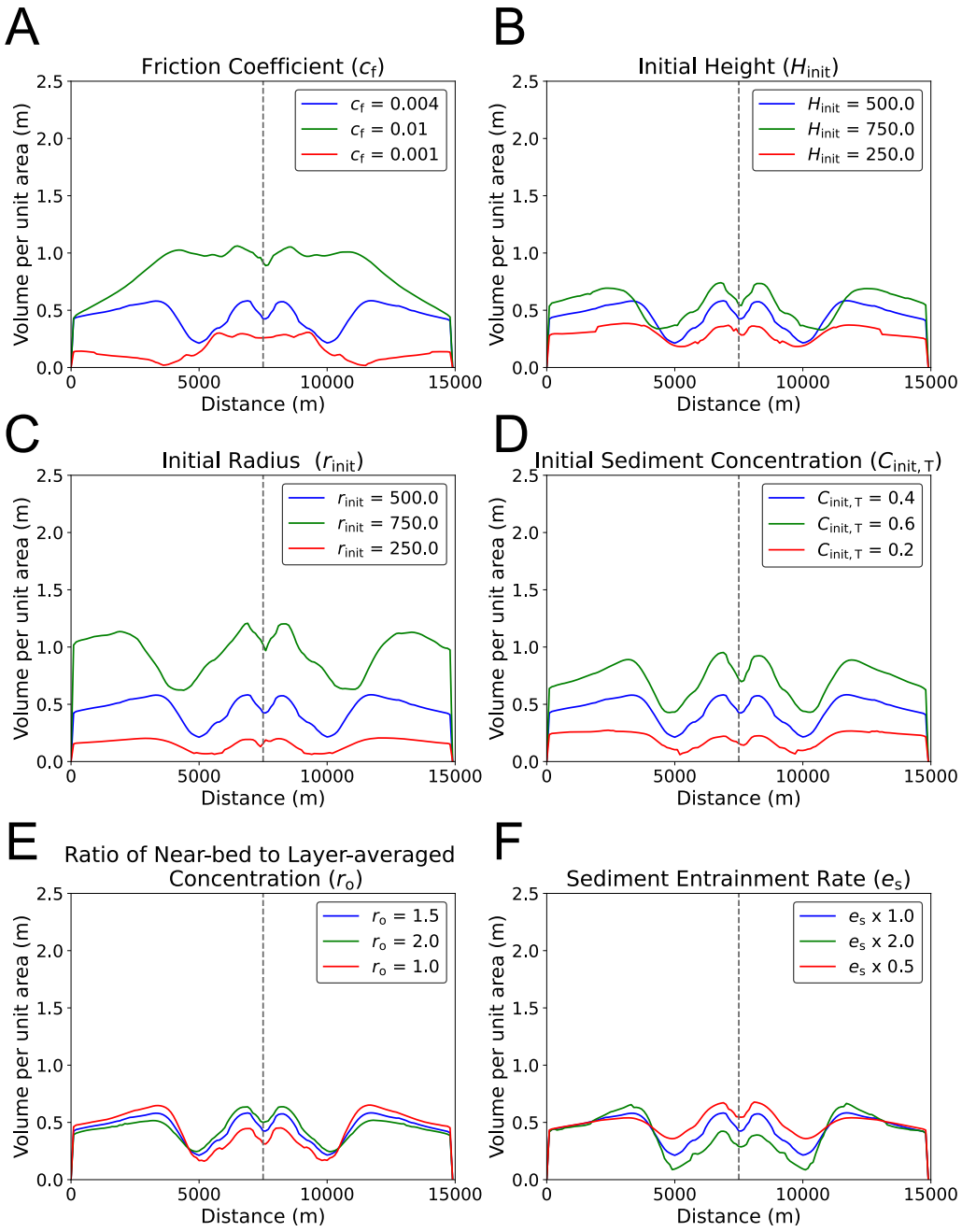

Figure 3.9: Sensitivity tests of deposit profile of numerical turbidites to change in initial flow conditions and closure parameters along A-A' with h_r set to 50 m (Table 3.3). The gray dotted line indicates the center of the channel outlet into basin. A. Dependency on initation region height H_{init}. B. Dependency on initiation region radius r_{init}. C. Dependency on initiation region total sediment volumetric concentration $C_{T,0}$. D. Dependency on friction coefficient c_f. E. Dependency on the ratio of near-bed to layer-averaged concentration r_o. F. Dependency on sediment entrainment rate e_s.

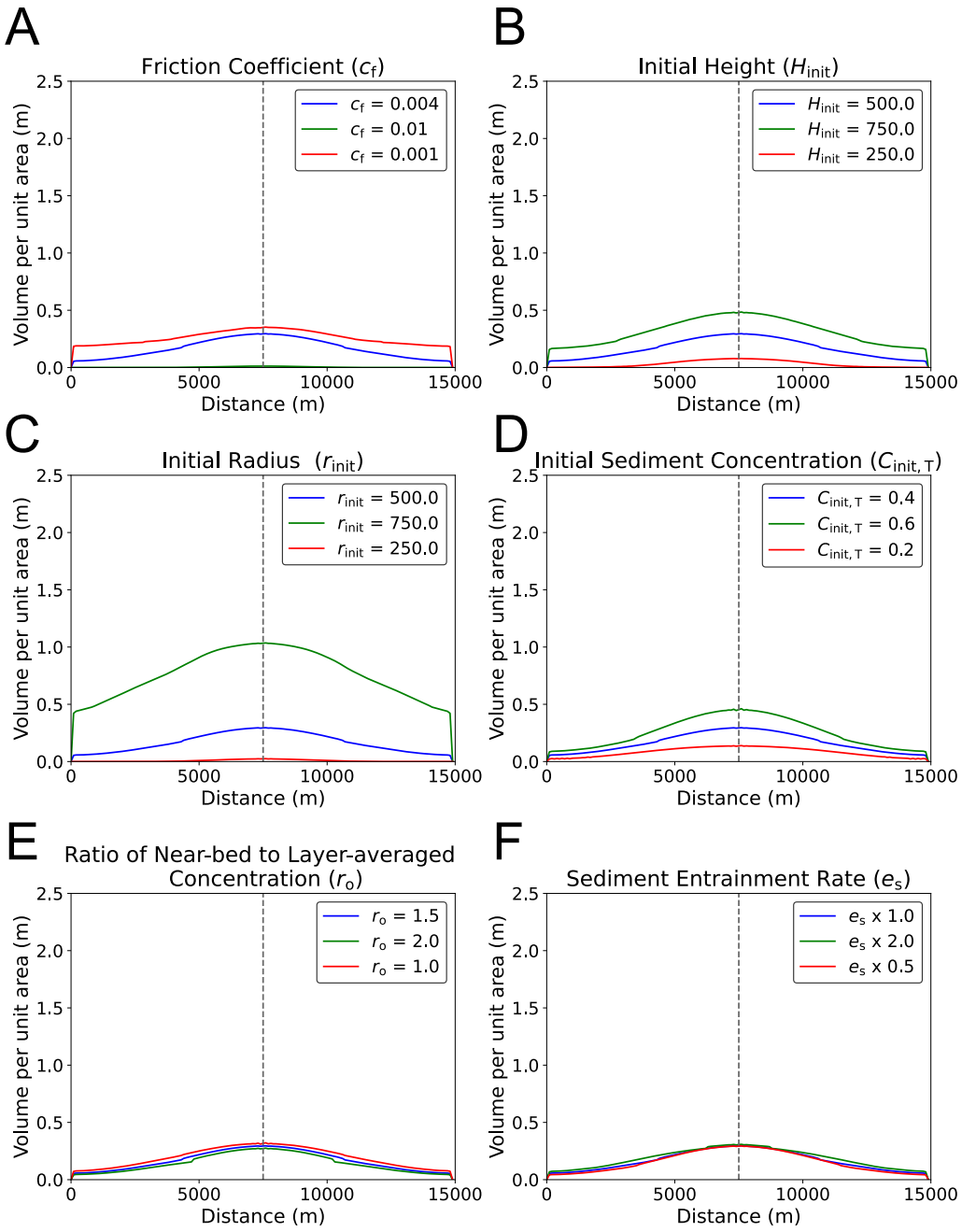

Figure 3.10: Sensitivity tests of deposit profile of numerical turbidites to change in initial flow conditions and closure parameters along B-B' with h_r set to 50 m (Table 3.3). The gray dotted line indicates the center of the channel outlet into basin. A. Dependency on initation region height H_{init}. B. Dependency on initiation region radius r_{init}. C. Dependency on initiation region total sediment volumetric concentration $C_{T,0}$. D. Dependency on friction coefficient c_f. E. Dependency on the ratio of near-bed to layer-averaged concentration r_o. F. Dependency on sediment entrainment rate e_s.

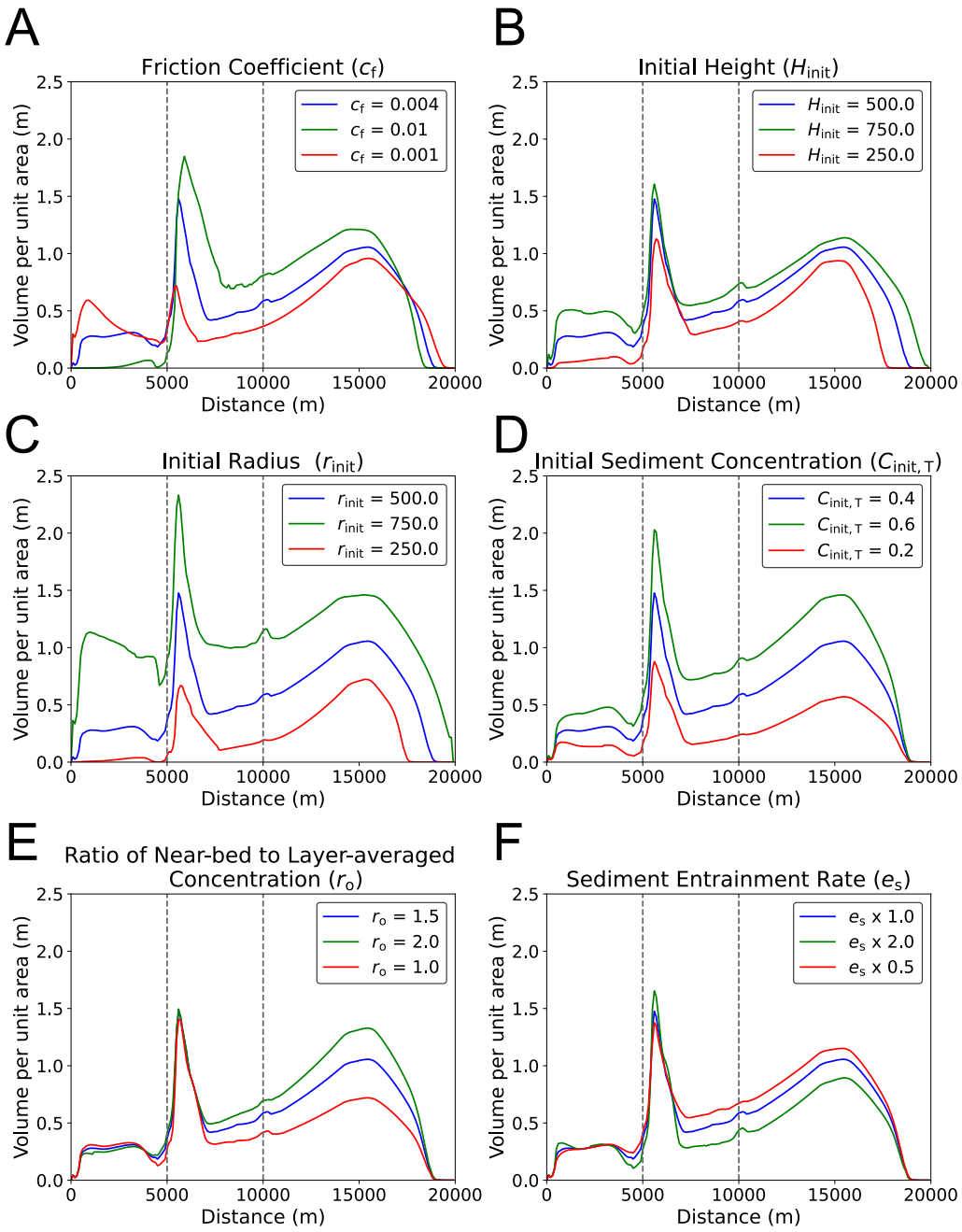

Figure 3.11: Sensitivity tests of deposit profile of numerical turbidites to change in initial flow conditions and closure parameters along C-C' with h_r set to 50 m (Table 3.3). The gray dotted line on left indicates the center of the ridge. The gray dotted line on right indicates the canyon-basin break. A. Dependency on initation region height H_{init}. B. Dependency on initiation region radius r_{init}. C. Dependency on initiation region total sediment volumetric concentration $C_{T,0}$. D. Dependency on friction coefficient c_f. E. Dependency on the ratio of near-bed to layer-averaged concentration r_o. F. Dependency on sediment entrainment rate e_s.

Sensitivity Tests of Forward Model Using Different Ridge Height

The numerical simulation with initial regions parameters H_{init} (m), r_{init} (m), and $C_{\text{init,T}}$ set to 500 m, 500 m, and 0.4. The $C_{\text{init,i}}$ was 0.1 for each of the four grain-size classes. Cases of artificial topography with ridge width w_{r} of 500 m and ridge height h_{r} between 25 m and 175 m were tested. Figure 3.12 shows the deposit profiles of flow in the northern region of the basin before hitting the ridge, where we see a relatively small change in deposit thickness occurs as ridge height changes for ridge height h_{r} over 50 m. Figure 3.13 shows that a change in ridge height greatly affects the deposit thickness in the southern region of the basin after hitting the ridge. Deposit thickness was tiny for h_{r} = 75 m and dropped to near zero for values above it. A significant decrease in deposit thickness can be observed in the southern basin as h_{r} increased from 25 m to 50 m and then to 75 m. The difference between the amount of change in deposit thickness north and south of the ridge is also obvious from Figure 3.14.

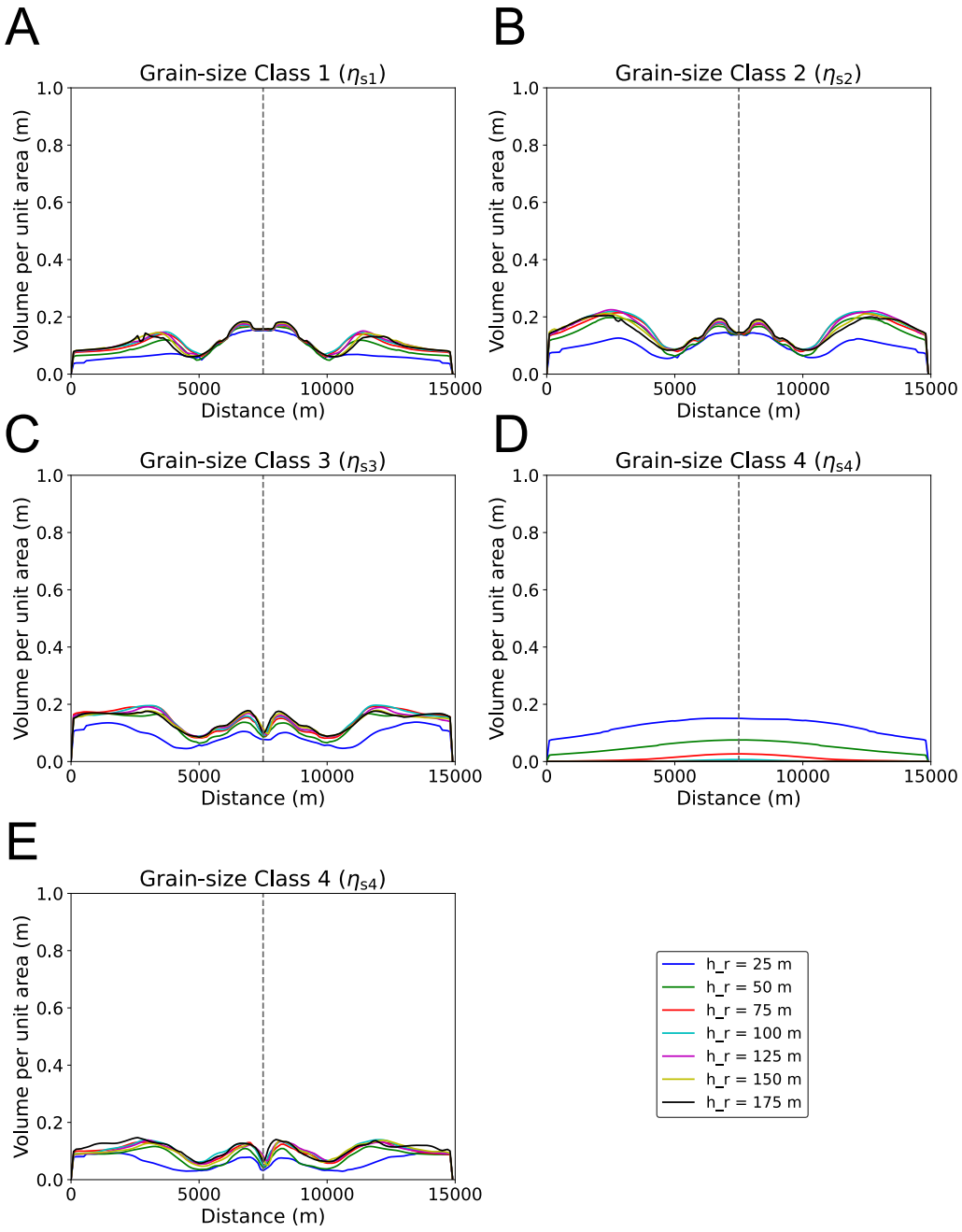

Figure 3.12: Deposit profiles of numerical turbidites at different topographical ridge height along line A-A'. The gray dotted line indicates the center of the channel outlet into basin. A. Time evolution of deposit profile η_{sT}. B. Time evolution deposit profile of grain-size class 1 η_{s1}. C. Time evolution of deposit profile of grain-size class 2 η_{s2}. D. Time evolution of deposit profile of grain-size class 3 η_{s3}. E. Time evolution of deposit profile of grain-size class 4 η_{s4}.

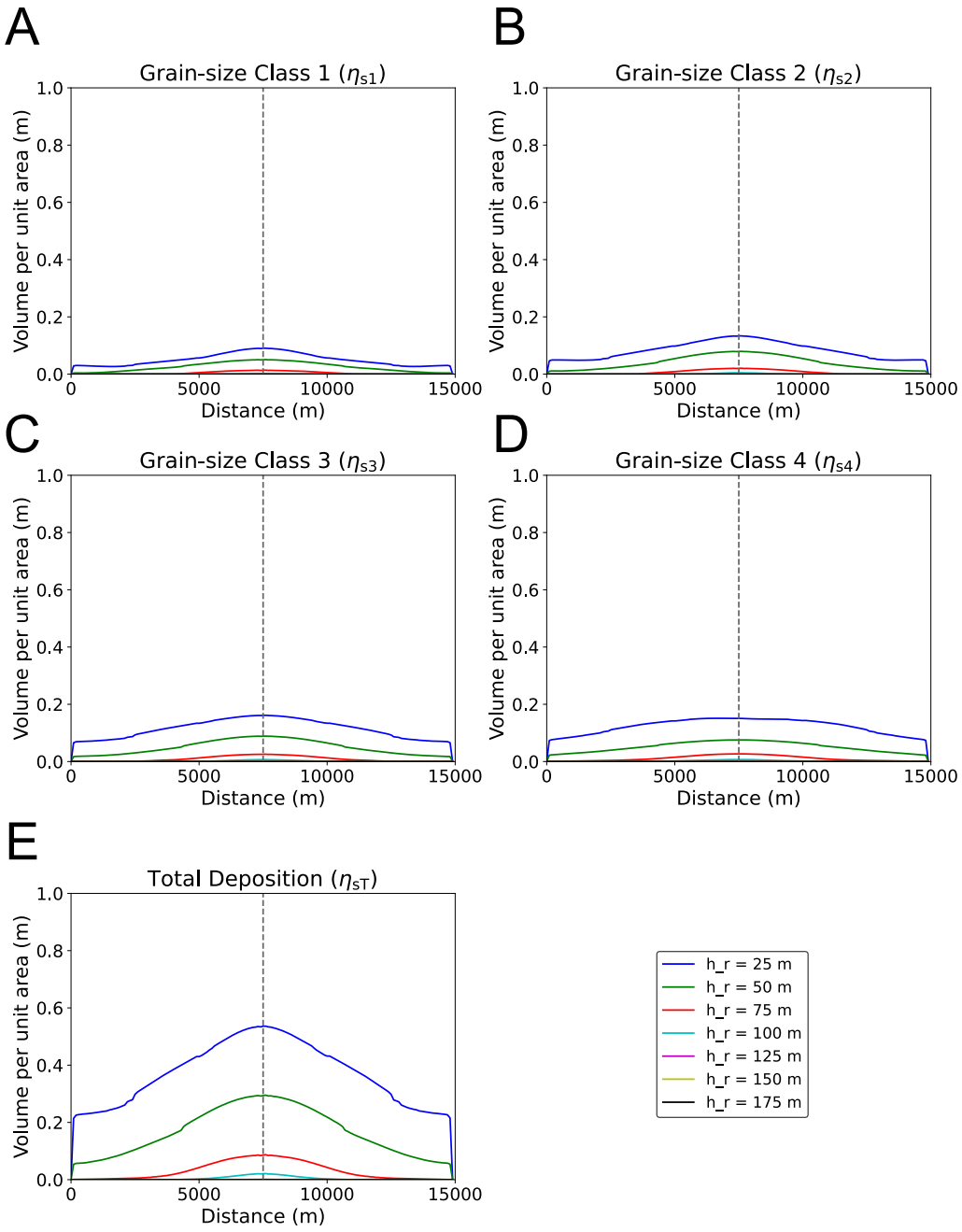

Figure 3.13: Deposit profiles of numerical turbidites at different topographical ridge height along line B-B'. The gray dotted line indicates the center of the channel outlet into basin. A. Time evolution of deposit profile η_{sT}. B. Time evolution deposit profile of grain-size class 1 η_{s1}. C. Time evolution of deposit profile of grain-size class 2 η_{s2}. D. Time evolution of deposit profile of grain-size class 3 η_{s3}. E. Time evolution of deposit profile of grain-size class 4 η_{s4}.

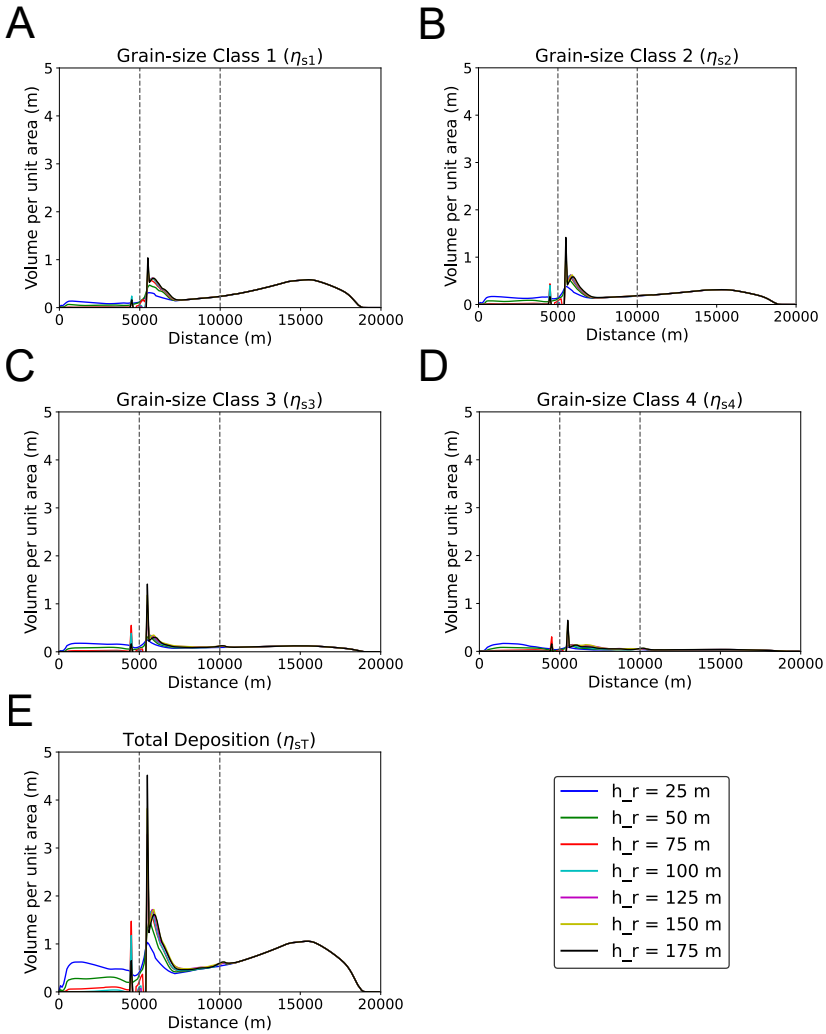

Figure 3.14: Deposit profiles of numerical turbidites at different topographical ridge height along line C-C'. The gray dotted line on left indicates the center of the ridge. The gray dotted line on right indicates the canyon-basin break. A. Time evolution of deposit profile η_{sT}. B. Time evolution deposit profile of grain-size class 1 η_{s1}. C. Time evolution of deposit profile of grain-size class 2 η_{s2}. D. Time evolution of deposit profile of grain-size class 3 η_{s3}. E. Time evolution of deposit profile of grain-size class 4 η_{s4}.

3.5.2 Inverse analysis of Artificial Datasets

The training of the DNN model ended with validation loss of 0.0063 for training datasets of ridge height h_r = 25 m, and 0.0067 for training datasets of h_r = 50 m. Figures 3.15A and 3.16A shows that overlearning did not occur, as no deviation was observed between the resulting values of the loss functions for the training and validation datasets. Overall, the reconstructed values mostly matched with the original values, with a few outliers (Figures 3.15B-G, and 3.16B-G).

The ranges of misfit ($2s$) were reasonable for all parameters, which had $2s/C_v^*$ values under 36.2% for h_r = 25 m case (Table 3.4) and under 29.3% other than H_{init} (48.6%) for h_r = 50 m case (Table 3.5). For the h_r = 25 m case, $C_{init,1}$, $C_{init,2}$, and $C_{init,3}$ have zero within the 95% CI of B , but not for H_{init}, r_{init}, and $C_{init,4}$. CI range was below zero for H_{init} and $C_{init,4}$ and above zero for r_{init}. For the h_r = 50 m case, $C_{init,2}$, $C_{init,3}$, and $C_{init,4}$ have zero within the 95% CI of B , but not for H_{init}, r_{init}, and $C_{init,1}$. CI range was below zero for H_{init} and r_{init} and above zero for $C_{init,4}$.

Table 3.4: Sample standard deviation and bias of the inversion result for numerical datasets of Anno Formation with h_r set to 25 m.

Parameters	s	C_v^*	$2s/C_v^*$	B	CI of B
H_{init} (m/s)	70.4	525	0.268	-14.5	(-27.1, -3.61)
r_{init} (m)	40.0	500	0.160	6.80	(0.596, 13.5)
$C_{init,1}$	0.0185	0.1025	0.362	-0.00315	(-0.00640, 0.000382)
$C_{init,2}$	0.0115	0.1025	0.224	0.000747	(-0.00123, 0.00299)
$C_{init,3}$	0.0110	0.1025	0.216	-0.00186	(-0.00450, 0.000145)
$C_{init,4}$	0.0135	0.1025	0.263	-0.00417	(-0.00708, -0.00213)

3.5.3 Inverse analysis of Outcrop Datasets

Field Survey

In this study, field survey was conducted for sedimentary successions near the tuff key bed An-55, which was mainly composed of scoria tuff and pumice tuff. An-55 and adjacent sedimentary successions were mainly exposed near the central part of Boso Peninsula and

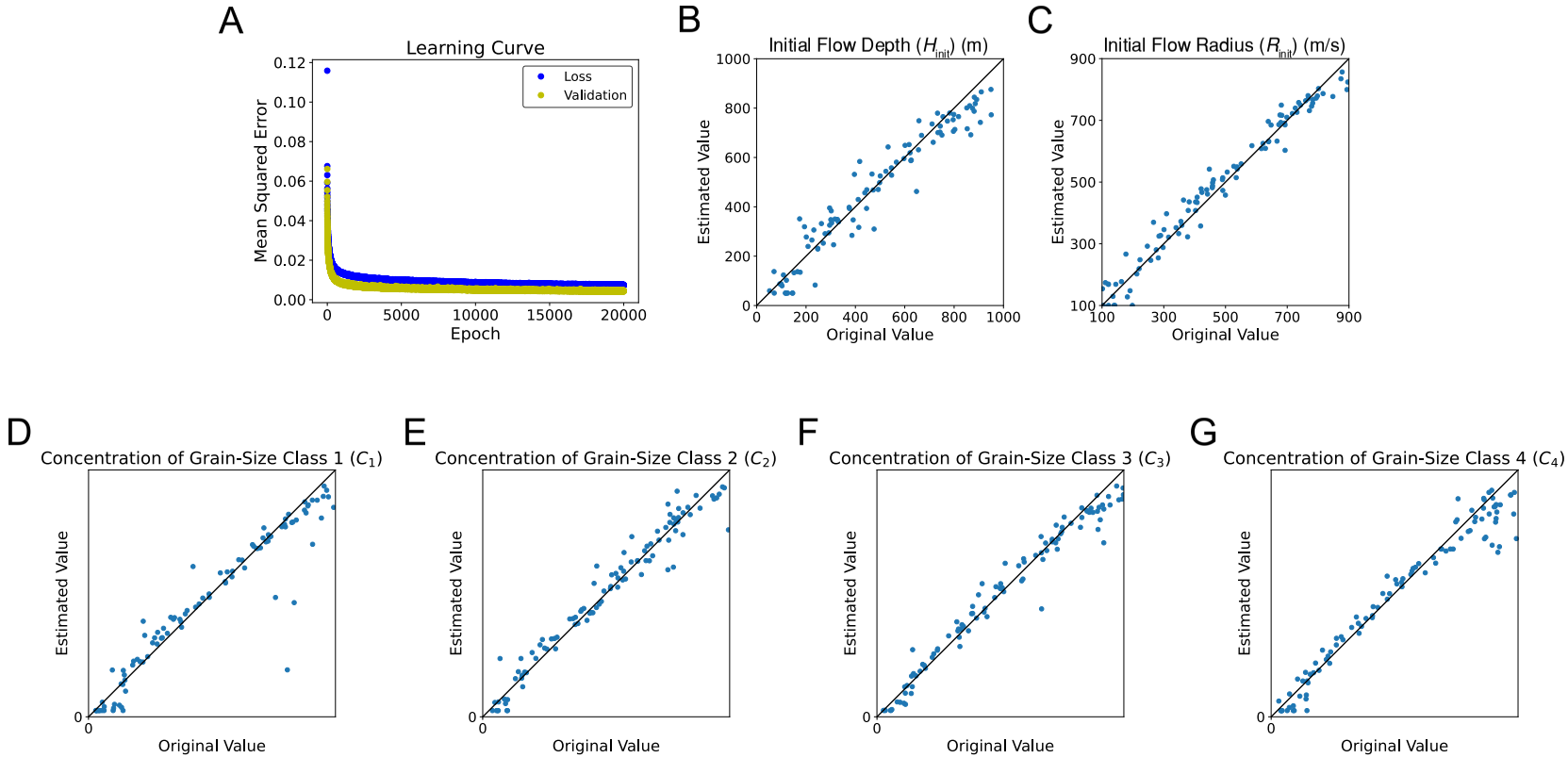

Figure 3.15: Results of inverse analysis of artificial datasets of turbidite from Anno Formation with h_r set to 25 m. The black diagonal line in each graph is where values on the x-axis (the true values) equal to the values on the y-axis (the estimated values). If a point lies on this line, the reconstructed value matches the true value perfectly. A. Learning curve. B. Estimates of H_{init}. C. Estimates ofr_{init}. D. Estimates of $C_{init,1}$. E. Estimates of $C_{init,2}$. F. Estimates of $C_{init,3}$. G. Estimates of $C_{init,4}$.

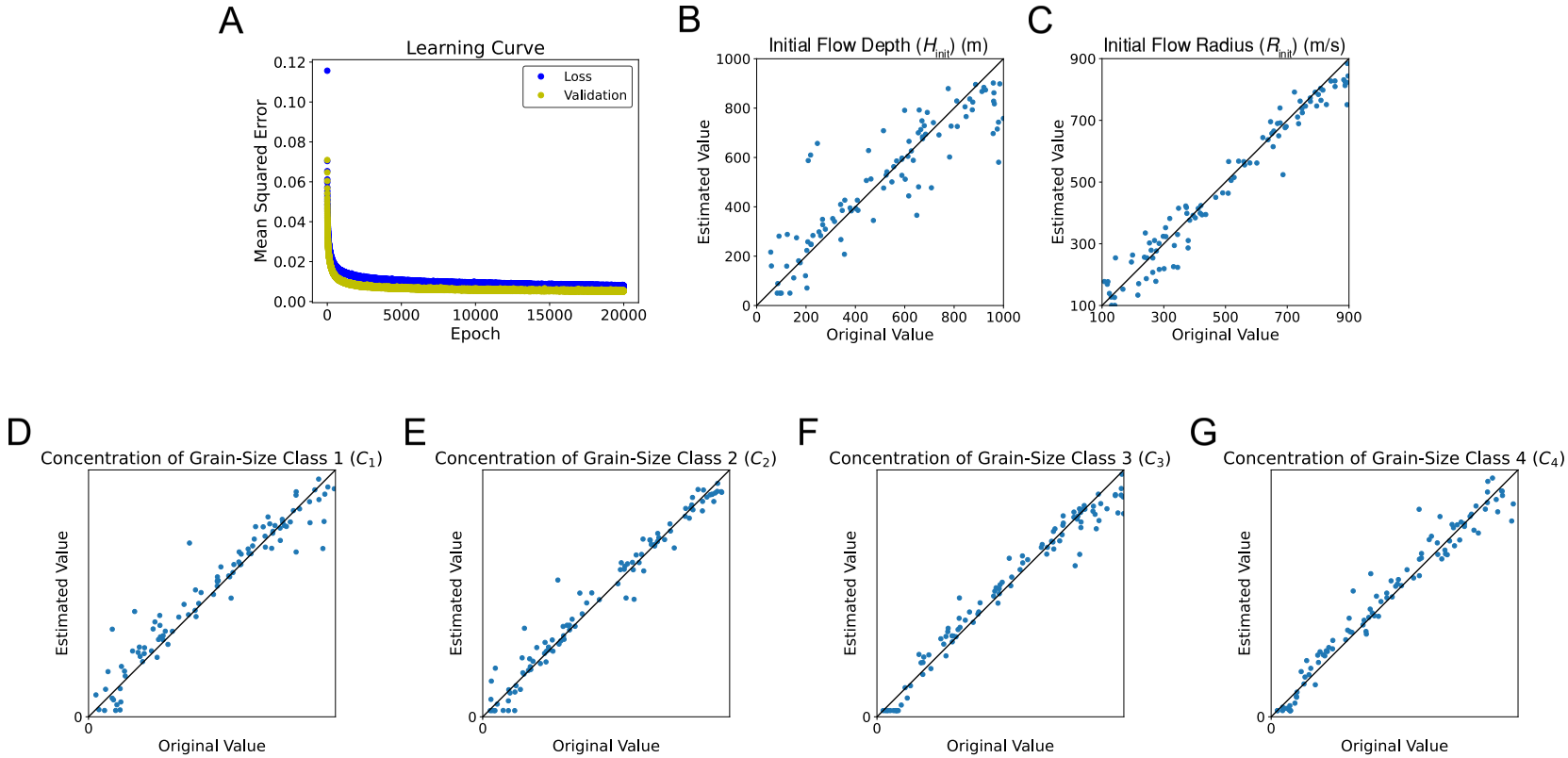

Figure 3.16: Results of inverse analysis of artificial datasets of turbidite from Anno Formation with h_r set to 50 m. The black diagonal line in each graph is where values on the x-axis (the true values) equal to the values on the y-axis (the estimated values). If a point lies on this line, the reconstructed value matches the true value perfectly. A. Learning curve. B. Estimates of H_{init}. C. Estimates ofr_{init}. D. Estimates of $C_{init,1}$. E. Estimates of $C_{init,2}$. F. Estimates of $C_{init,3}$. G. Estimates of $C_{init,4}$.

Table 3.5: Sample standard deviation and bias of the inversion result for numerical datasets of Anno Formation with h_r set to 50 m.

Parameters	s	C_v^*	$2s/C_v^*$	B	CI of B
H_{init} (m/s)	127.0	525	0.486	-6.31	(-29.2, 15.3)
r_{init} (m)	49.3	500	0.197	-11.2	(-19.7, -1.74)
$C_{\text{init},1}$	0.0150	0.1025	0.293	0.00286	(0.0000801, 0.00577)
$C_{\text{init},2}$	0.0107	0.1025	0.208	0.00119	(-0.000597, 0.00341)
$C_{\text{init},3}$	0.0114	0.1025	0.222	-0.00117	(-0.00327, 0.000779)
$C_{\text{init},4}$	0.0116	0.1025	0.227	0.00189	(-0.000417, 0.00474)

can be found in a wide area to the east and west of the central region. The depositional environment of An-55 was an elongated basin extending in the east-west direction under a channel-lobe transition zone to lobe setting as described in Section 3.2. A ridge along the Kiyosumi anticline and a rise in the south rim of the basin during deposition was identified by *Tokuhashi* [1982], which was the basis of the shape of the artificial basin created for the numerical simulations. The paleocurrent direction observed during the field survey was mainly toward the southeast in the eastern part of the Boso Peninsula and toward the west in the southern part of the Boso Peninsula, the same as the paleocurrent direction identified by *Tokuhashi* [1982]. An-55 observed at the outcrops observed was over 50 cm in thickness, much thicker than other tuff beds observed in the region surveyed, and had an upward grading structure, making it easy to trace as a marker bed. Turbidites deposited close to An-55 ranged from a few centimeters to around 60 cm in thickness. There was a maximum of 24 turbidite units observed at one outcrop. The thickness of hemipelagic mud units in between turbidites was relatively constant over the area surveyed, making them effective reference layers for tracing a single turbidite bed over the region surveyed.

The target turbidite layer q_t was observed and sampled at 9 outcrops that spread in a 10 km range in this study. The location of the outcrops are stated in Table 3.2. Columnar sections of the sampled outcrops are shown in Figures 3.17 and 3.18, where Figure 3.17 contains outcrops north of the Kiyosumi anticline axis and Figure 3.18 contains outcrops south of the anticline axis. As shown in the columnar sections, the thickness of q_t varies

greatly at different locations, with the thinnest unit at 6.1 cm (outcrop no. 4) and the thickest unit at 44.0 cm (outcrop no. 14n). Turbidity layer q_t was chosen as the target for inverse analysis because it was close to the bottom of key bed An-55 and was relatively well exposed over a large area. Turbidite q_t was also thicker than other turbidites immediately above and below it, meaning it was likely to be more well preserved than the thinner beds, which could contain intervals with no obvious deposition and would be harder to correlate continuously over a long distance.

At the 9 outcrops observed, convolute lamination, ripple lamination, and sometimes parallel lamination was observed in units identified as q_t (Figures 3.19A), which made the evidence for the correlation between different outcrops very persuasive. The type of lamination observed in q_t differs at different outcrops, and at some locations, more than one type of lamination was observed. Partially laminated and partially structureless outcrops of q_t was also observed (Figure 3.19B). The shape of q_t units observed were tabular in form and had a flat boundary both at the top and the bottom, indicating no erosion or deformation happened after its deposition and the flow that deposited q_t was not erosional, a mechanism not yet incorporated in the forward model. In terms of grain size, q_t mainly consisted of particles the size of fine to very fine sand, which made it suitable for grain-size analysis and numerical simulation.

Results of Inverse Analysis of Outcrop Datasets

The reconstructed initial regions parameters H_{init} (m), r_{init} (m), and $C_{\mathrm{init,T}}$, were 938.6 m, 100.3 m, and 0.8212. $C_{\mathrm{init,1}}$, $C_{\mathrm{init,2}}$, $C_{\mathrm{init,3}}$, and $C_{\mathrm{init,4}}$ were 0.005064, 0.1648, 0.2153, and 0.4361. The reconstructed parameters were inputted in to the forward model and the calculated time evolutions of flow depth H for ridge height h_{r} = 25 m and h_{r} = 50 m are shown in Figures 3.20 and 3.21 in a three-dimensional view. In both cases, it is shown that the flow first entered the northern part of the basin, then spread out in the northern part of the basin as it slowly went over the ridge and overflowed into the southern part of the basin.

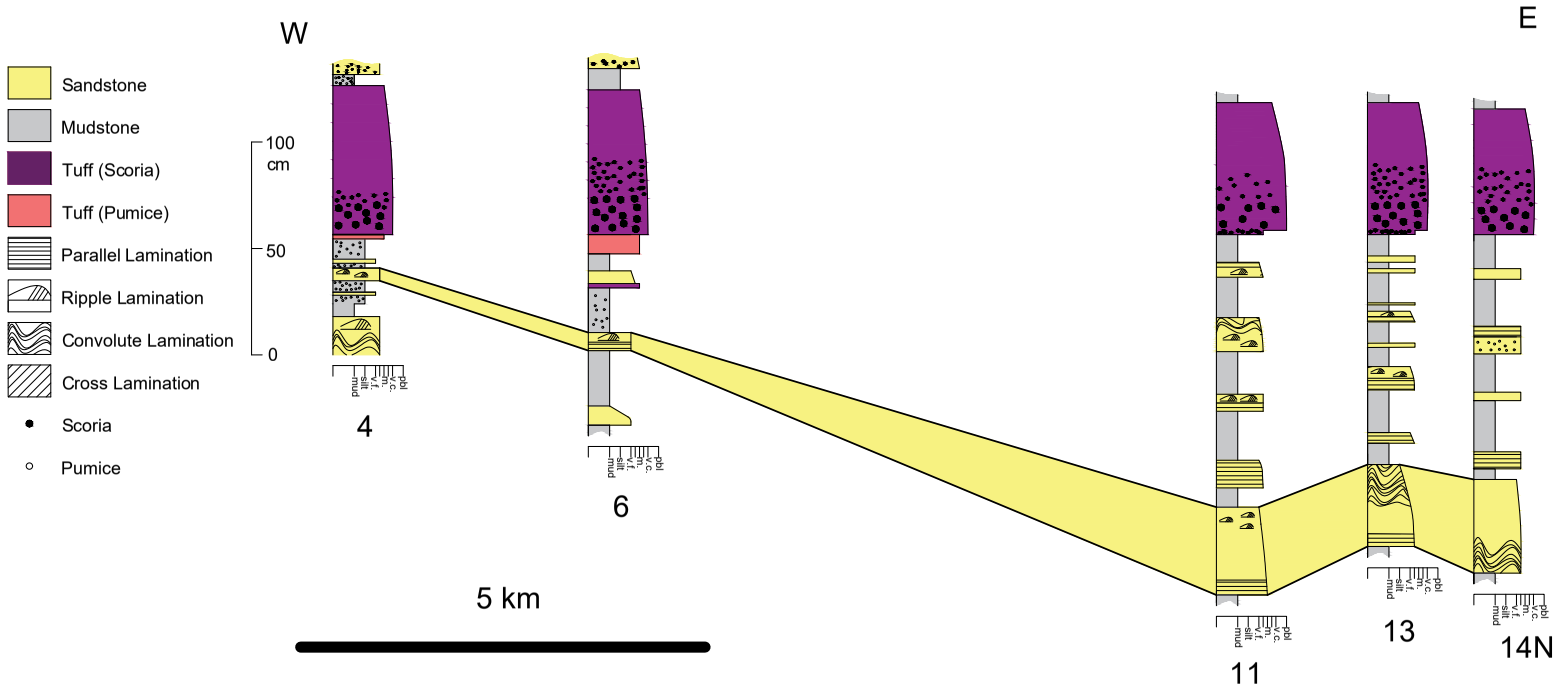

Figure 3.17: Columnar sections of outcrops north of the Kiyosumi Anticline (4, 6, 11, 13,14n)

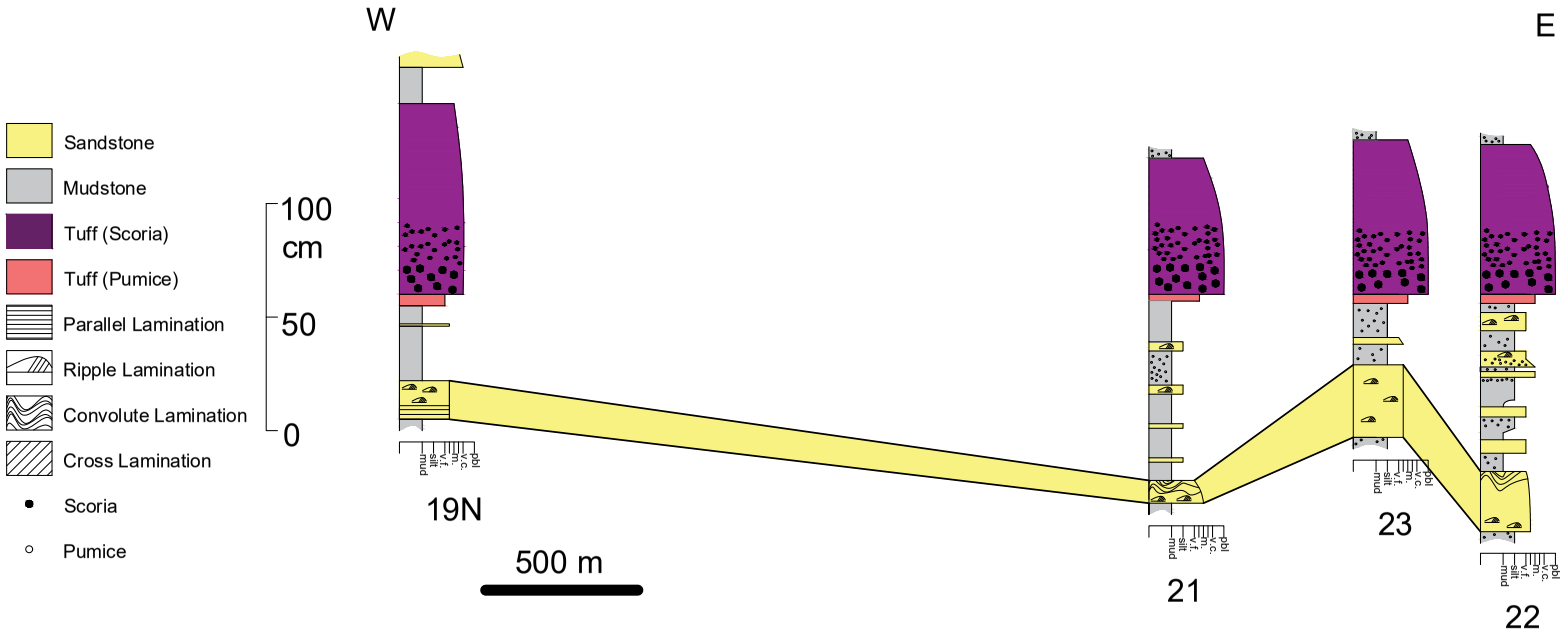

Figure 3.18: Columnar sections of outcrops south of the Kiyosumi Anticline (19n, 21, 22, 23)

A

B

Figure 3.19: A. Convolute lamination at outcrop 23. B. Structureless sandstone at outcrop 6.

Reflected flows were observed in both cases. In the northern part of the basin, the flow was partially reflected by the ridge, then again reflected off the slope around the canyon region. In the southern part of the basin, flow reflected off the southern rim of the basin and after hitting the ridge again reflected toward the southern rim.

Comparing the time evolution of flow depth in the southern part of basin Figures 3.23A and 3.26A, and Figures 3.22A and 3.27, it is obvious that flow depth was greater when entering the southern part of basin for h_r = 25 m and stayed greater for the h_r = 25 m case than the h_r = 50 m case as time went on. The total sediment concentration C_T and total deposition η_{sT} were also higher in the southern part of basin when h_r = 25 m (Figures 3.23C, D and 3.26C, D, Figures 3.24C, D and 3.27C, D). Flow characteristics in the northern part of basin was mostly similar for both h_r = 25 m and h_r = 50 m cases, with one significant difference being C_T at 500.0 s after the initiation of flow. Figures 3.22C and 3.25C, and Figures 3.24C and 3.27C show that C_T at 500.0 s was higher for the h_r = 25 m case than the h_r = 50 m case.

A scatter plot of reconstructed and measured η_{s1}, η_{s2}, η_{s3}, and η_{s4} at each outcrop location are shown in Figures 3.28 and 3.29, where a tendency of underestimation was observed in the reconstructed values for both cases, with the h_r = 50 m case showing a more precise reconstruction than h_r = 25 m case. Root mean squared error J for the h_r = 25 m case was 0.002417 and was 0.001904 for the h_r = 50 m case. The smaller J value for the h_r = 50 m case proves the observation from Figures 3.28 and 3.29 that h_r = 50 m had a more precise reconstruction.

Figures 3.30 and 3.31 presents the deposit thickness and grain size distribution of outcrops along the north and south side of the Kiyosumi Anticline (Figures 3.17 and 3.18), respectively. Figure 3.31 shows that reconstructed deposit profile in the southern part of basin matched relatively well with the measured values, while deviation was observed in the northern part of basin (Figure 3.30). The deviation in the northern part of basin occurred mainly at locations close to the channel (Figure 3.30).

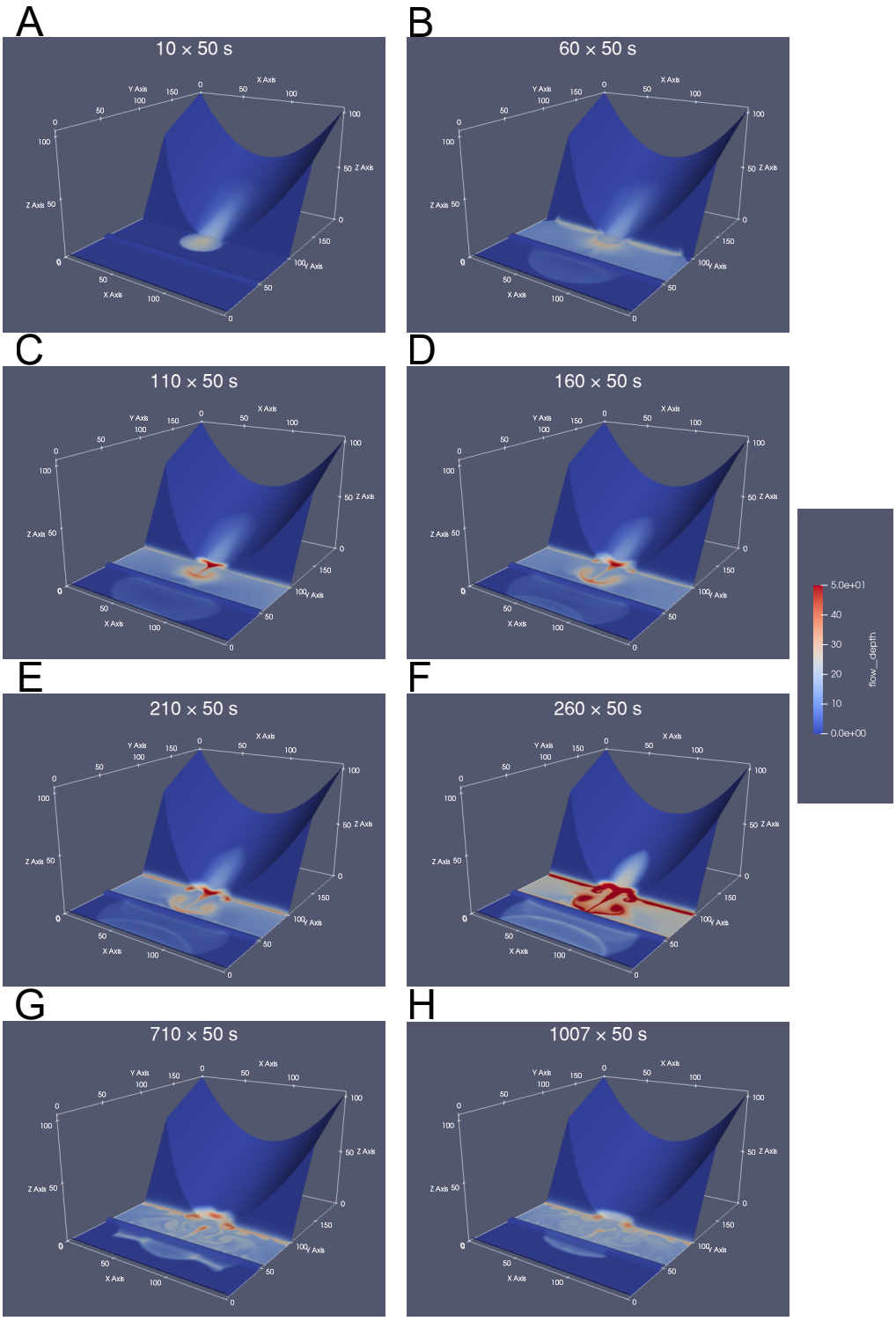

Figure 3.20: Time evolution of flow depth H over time for reconstructing the outcrop deposis with h_r set to 25 m.

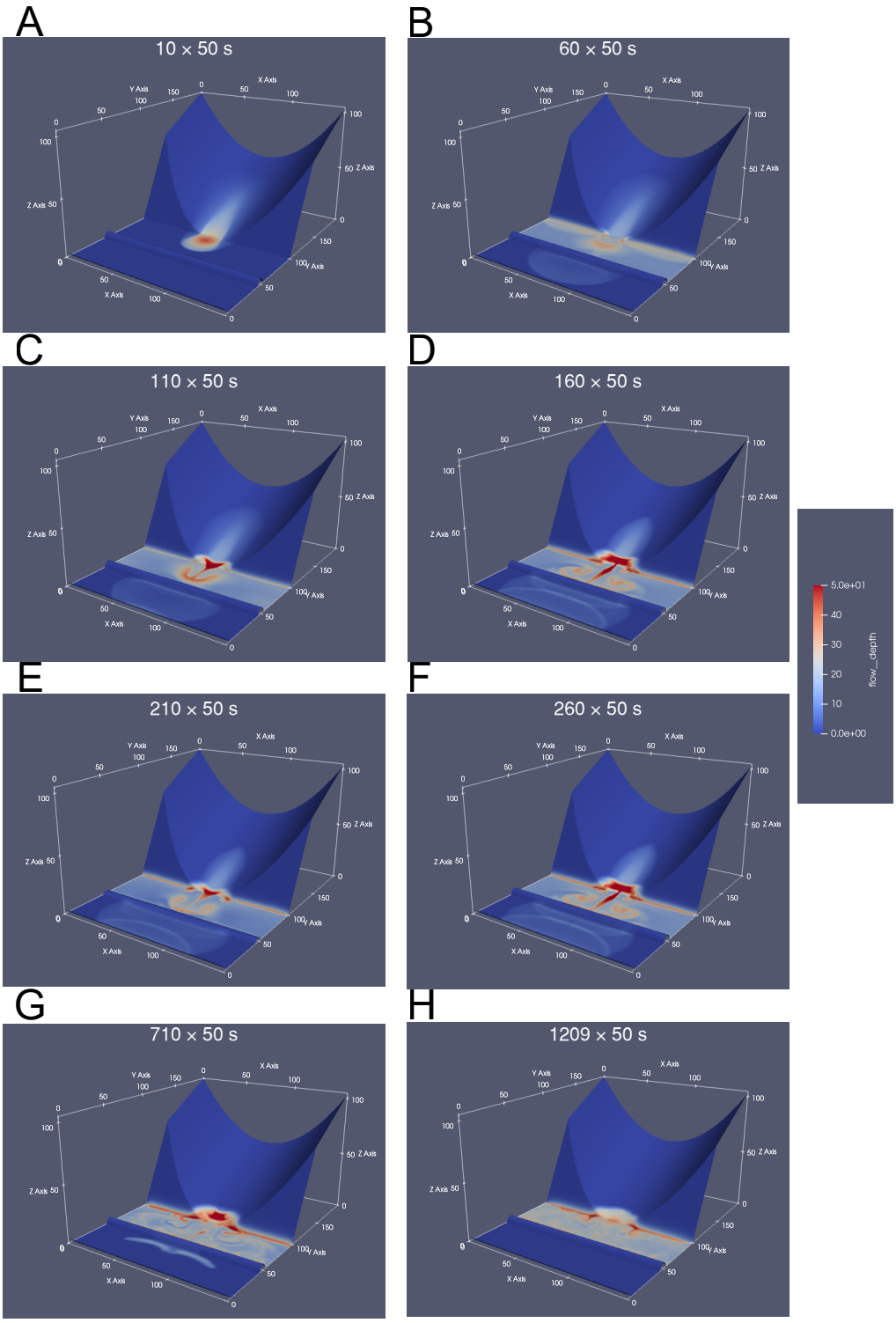

Figure 3.21: Time evolution of flow depth H over time for reconstructing the outcrop deposis with h_r set to 50 m.

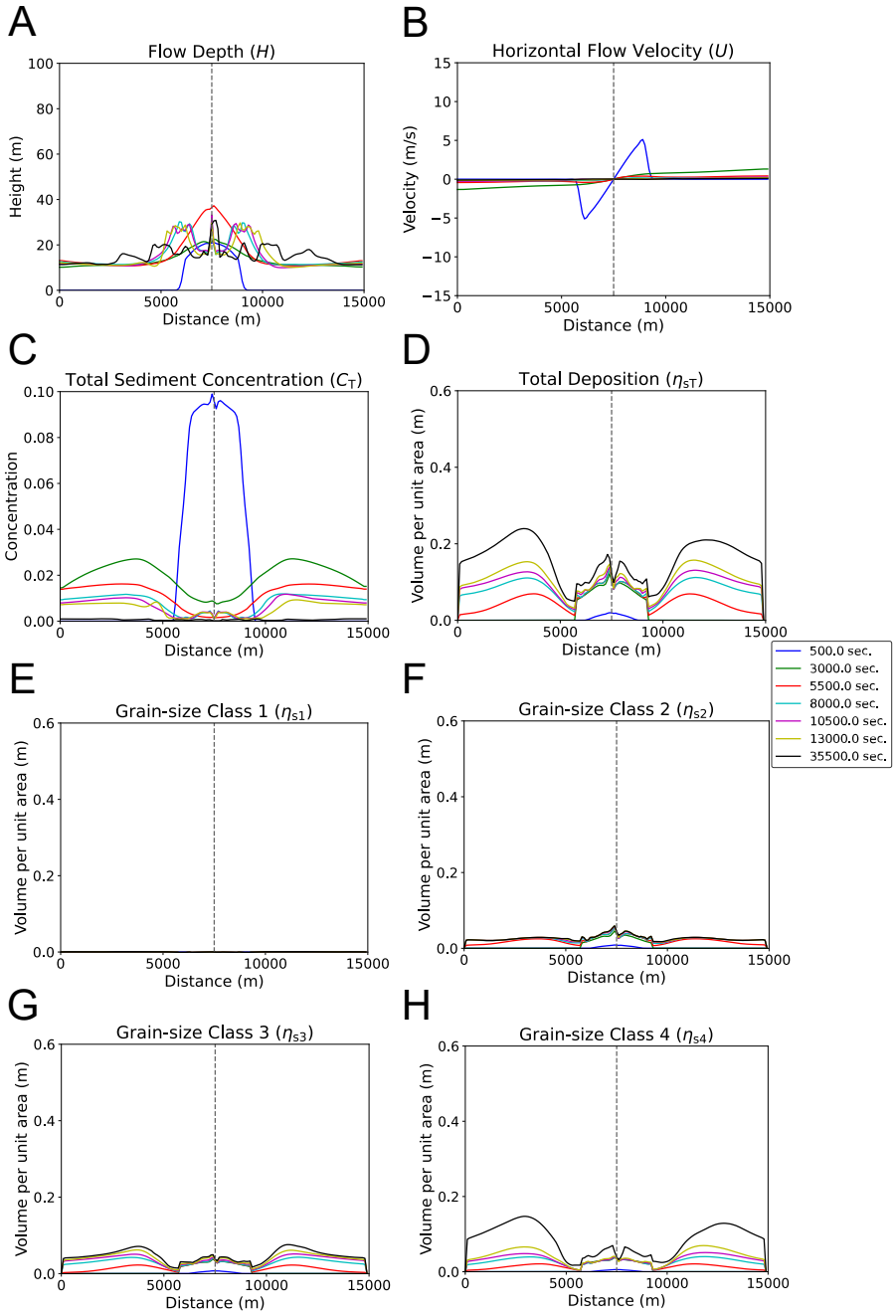

Figure 3.22: Time evolution of reconstruction calculation along A-A' with h_r set to 25 m. The gray dotted line indicates the center of the canyon outlet. A. Time evolution of flow depth H. B. Time evolution of horizontal flow velocity U. C. Time evolution of total sediment volumetric concentration C_T. D. Time evolution of total deposit thickness η_{sT}. E. Time evolution of deposit thickness of grain-size class 1 η_{s1}. F. Time evolution of deposit thickness of grain-size class 2 η_{s2}. G. Time evolution of deposit thickness of grain-size class 3 η_{s3}. H. Time evolution of deposit thickness of grain-size class 4 η_{s4}.

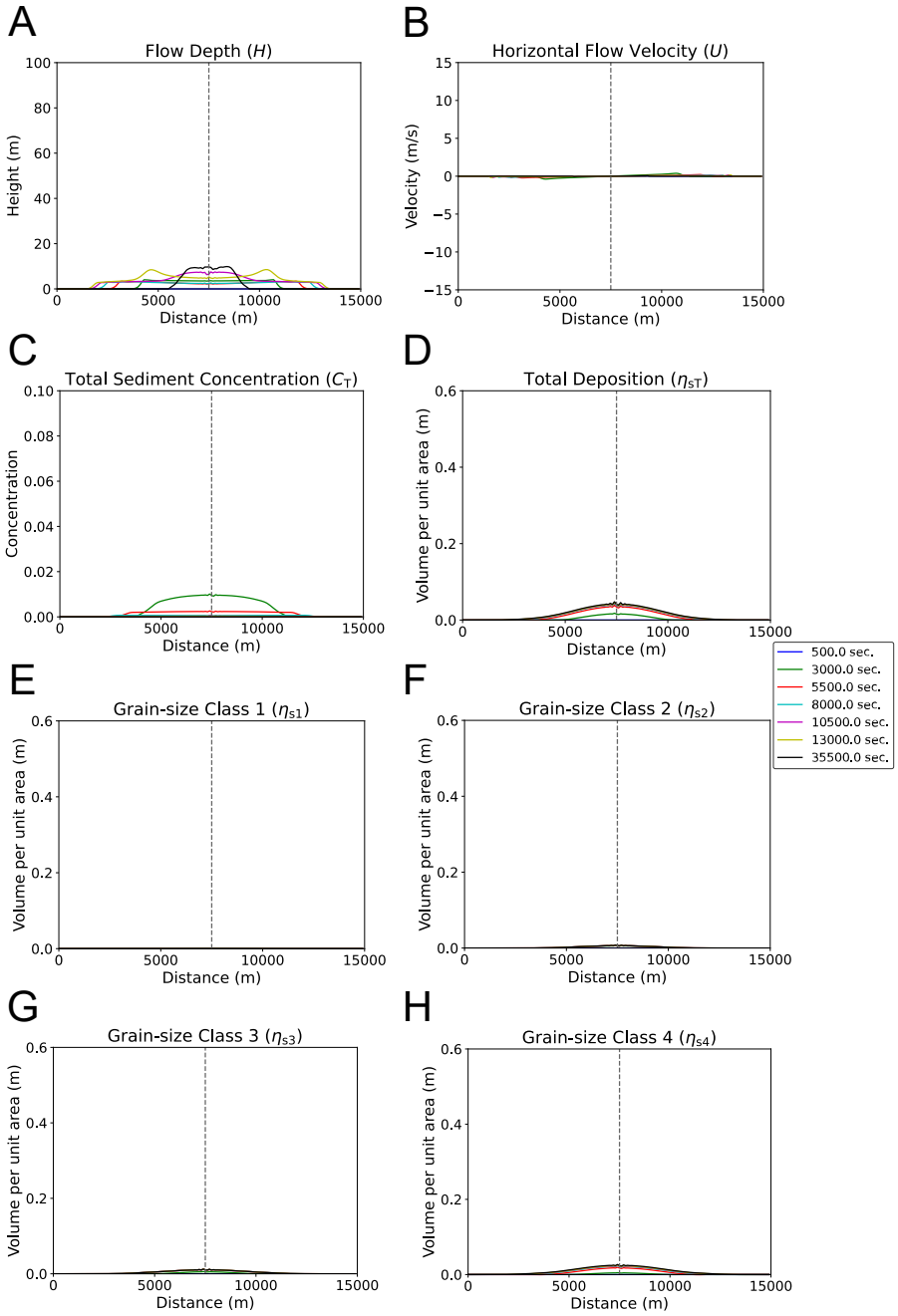

Figure 3.23: Time evolution of reconstruction calculation along B-B' with h_r set to 25 m. The gray dotted line indicates the center of the canyon outlet. A. Time evolution of flow depth H. B. Time evolution of horizontal flow velocity U. C. Time evolution of total sediment volumetric concentration C_T. D. Time evolution of total deposit thickness η_{sT}. E. Time evolution of deposit thickness of grain-size class 1 η_{s1}. F. Time evolution of deposit thickness of grain-size class 2 η_{s2}. G. Time evolution of deposit thickness of grain-size class 3 η_{s3}. H. Time evolution of deposit thickness of grain-size class 4 η_{s4}.

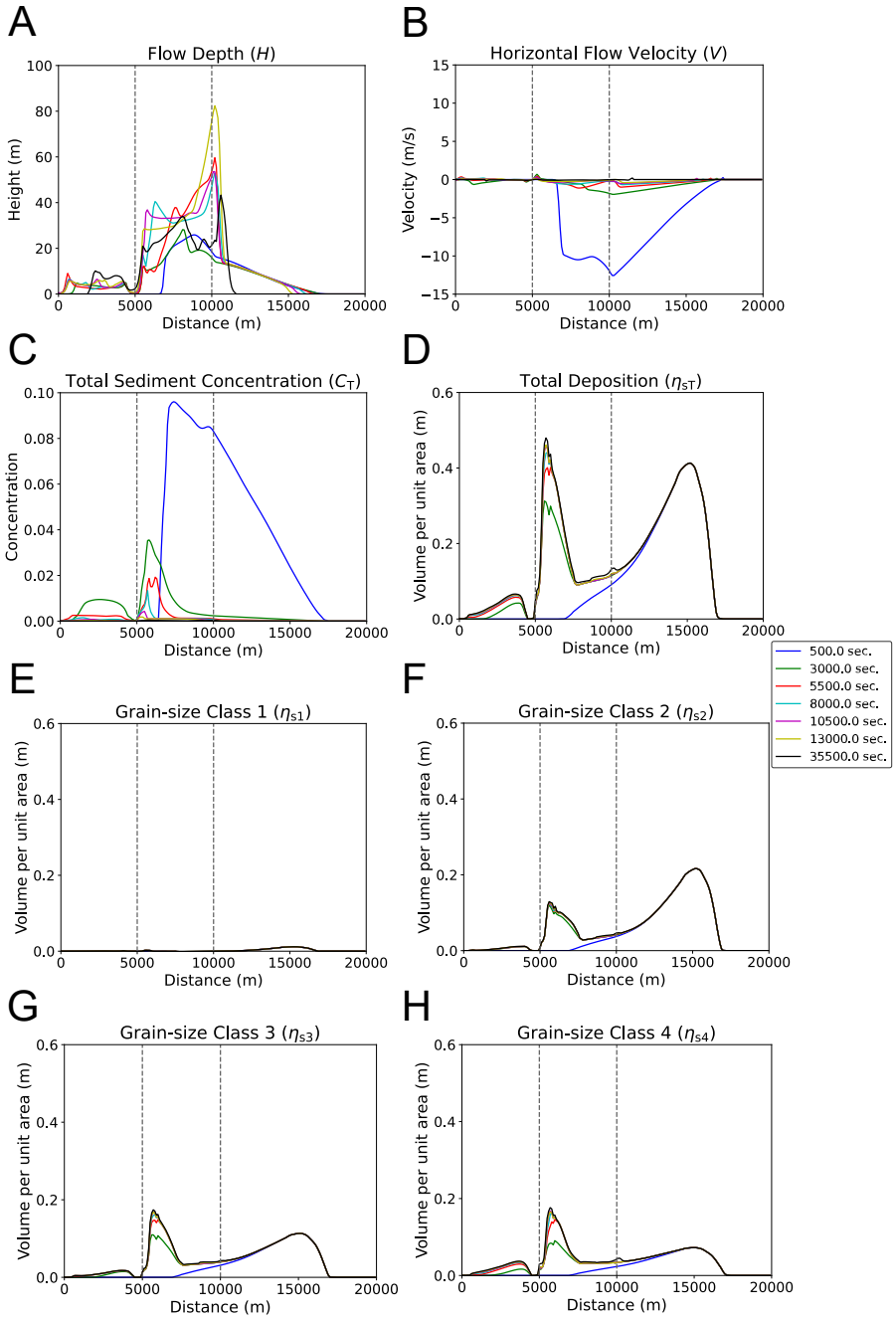

Figure 3.24: Time evolution of reconstruction calculation along C-C' with h_r set to 25 m. The gray dotted line on left indicates the center of the ridge. The gray dotted line on right indicates the canyon-basin break. A. Time evolution of flow depth H. B. Time evolution of horizontal flow velocity U. C. Time evolution of total sediment volumetric concentration C_T. D. Time evolution of total deposit thickness η_{sT}. E. Time evolution of deposit thickness of grain-size class 1 η_{s1}. F. Time evolution of deposit thickness of grain-size class 2 η_{s2}. G. Time evolution of deposit thickness of grain-size class 3 η_{s3}. H. Time evolution of deposit thickness of grain-size class 4 η_{s4}.

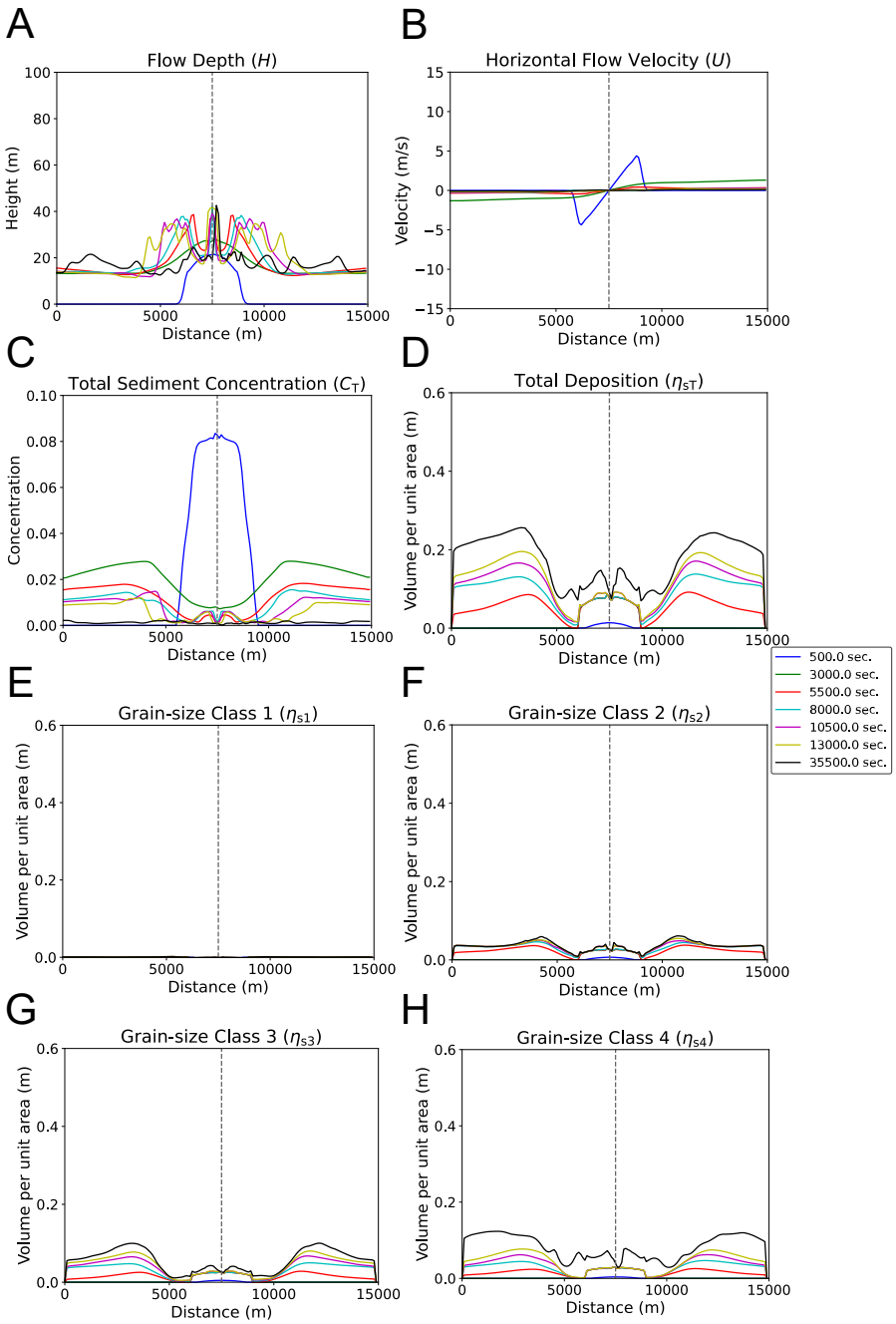

Figure 3.25: Time evolution of reconstruction calculation along A-A' with h_r set to 50 m. The gray dotted line indicates the center of the canyon outlet. A. Time evolution of flow depth H. B. Time evolution of horizontal flow velocity U. C. Time evolution of total sediment volumetric concentration C_T. D. Time evolution of total deposit thickness η_{sT}. E. Time evolution of deposit thickness of grain-size class 1 η_{s1}. F. Time evolution of deposit thickness of grain-size class 2 η_{s2}. G. Time evolution of deposit thickness of grain-size class 3 η_{s3}. H. Time evolution of deposit thickness of grain-size class 4 η_{s4}.

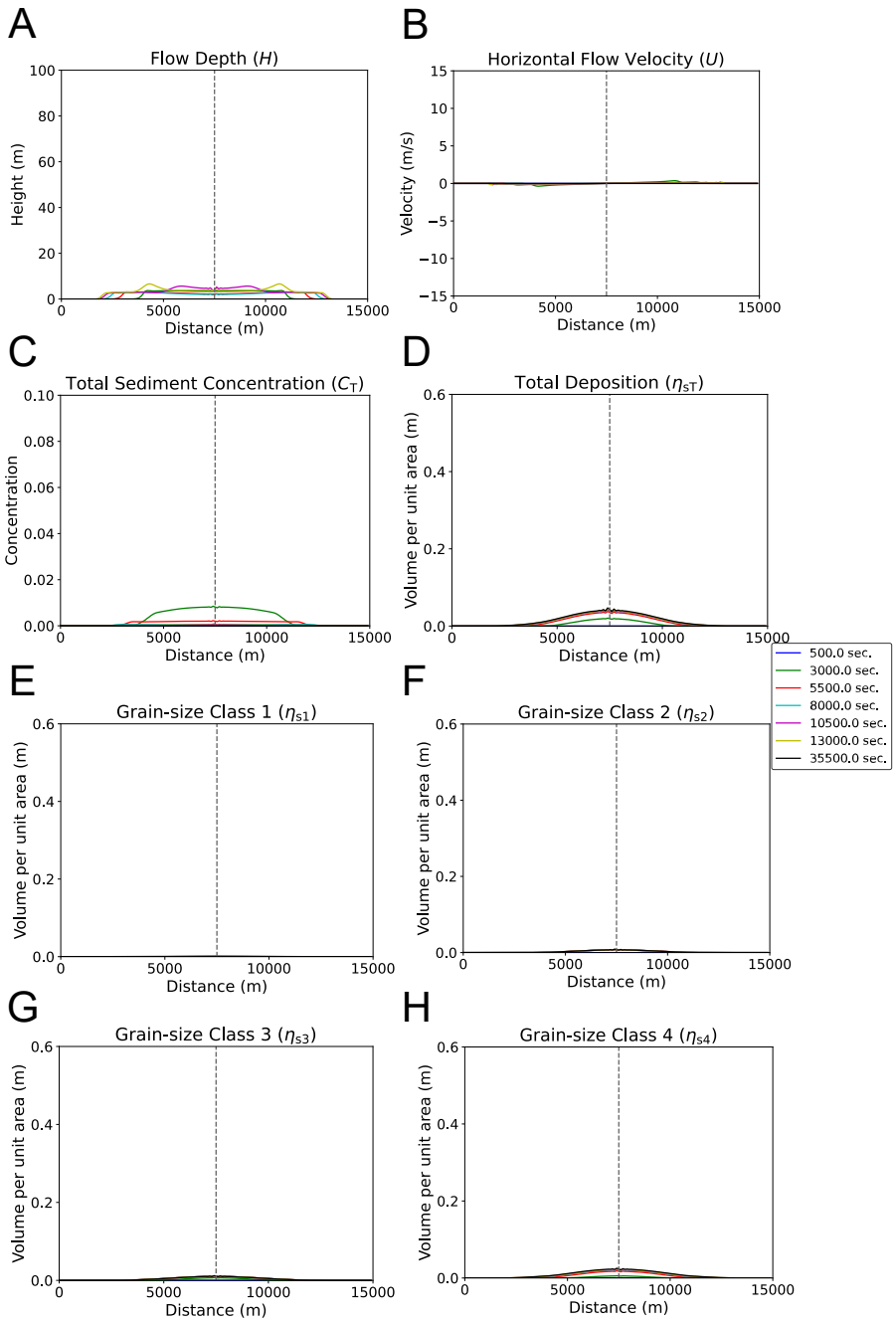

Figure 3.26: Time evolution of reconstruction calculation along B-B' with h_r set to 50 m. The gray dotted line indicates the center of the canyon outlet. A. Time evolution of flow depth H. B. Time evolution of horizontal flow velocity U. C. Time evolution of total sediment volumetric concentration C_T. D. Time evolution of total deposit thickness η_{sT}. E. Time evolution of deposit thickness of grain-size class 1 η_{s1}. F. Time evolution of deposit thickness of grain-size class 2 η_{s2}. G. Time evolution of deposit thickness of grain-size class 3 η_{s3}. H. Time evolution of deposit thickness of grain-size class 4 η_{s4}.

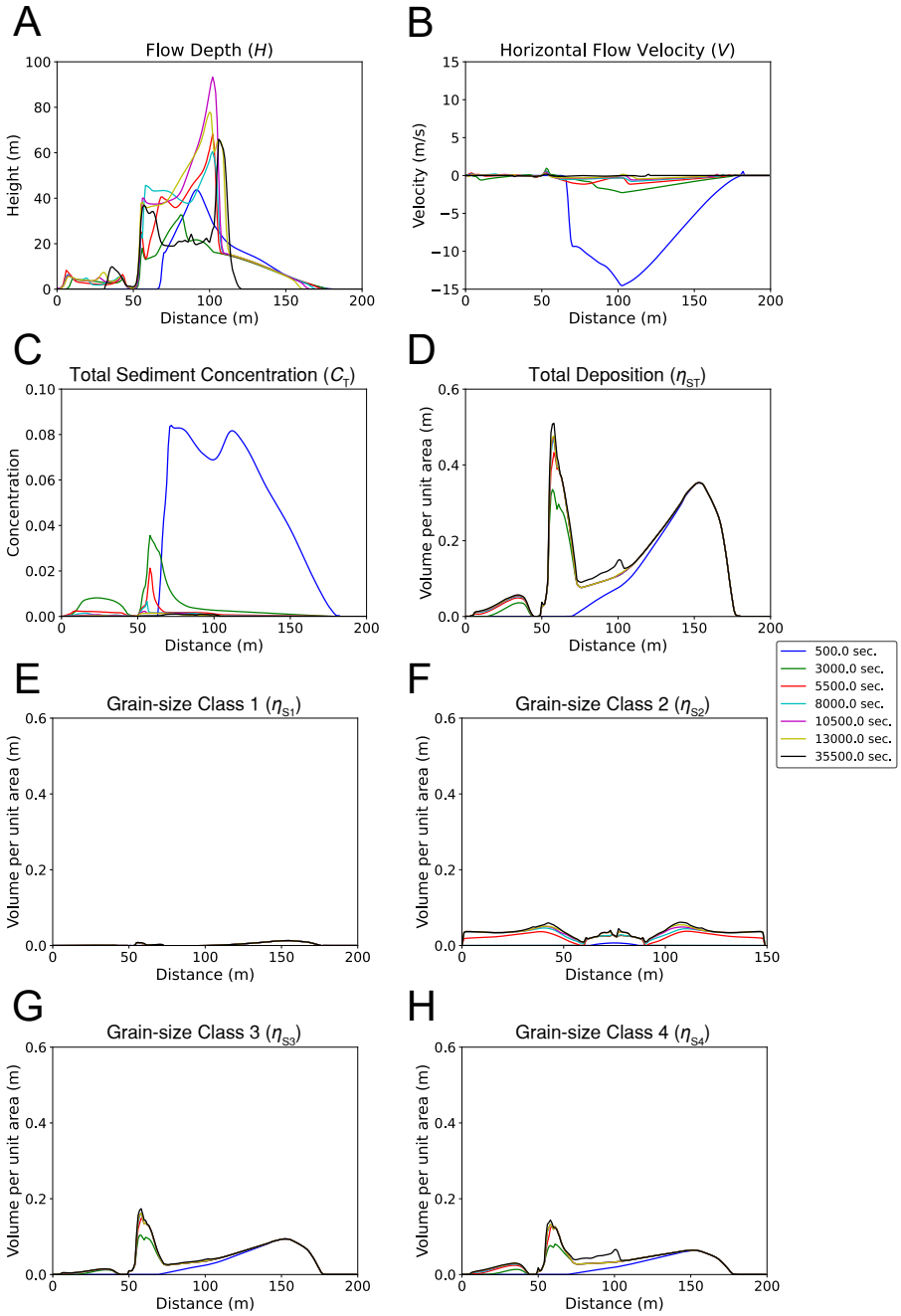

Figure 3.27: Time evolution of reconstruction calculation along C-C' with h_r set to 50 m. The gray dotted line on left indicates the center of the ridge. The gray dotted line on right indicates the canyon-basin break. A. Time evolution of flow depth H. B. Time evolution of horizontal flow velocity U. C. Time evolution of total sediment volumetric concentration C_T. D. Time evolution of total deposit thickness η_{sT}. E. Time evolution of deposit thickness of grain-size class 1 η_{s1}. F. Time evolution of deposit thickness of grain-size class 2 η_{s2}. G. Time evolution of deposit thickness of grain-size class 3 η_{s3}. H. Time evolution of deposit thickness of grain-size class 4 η_{s4}.

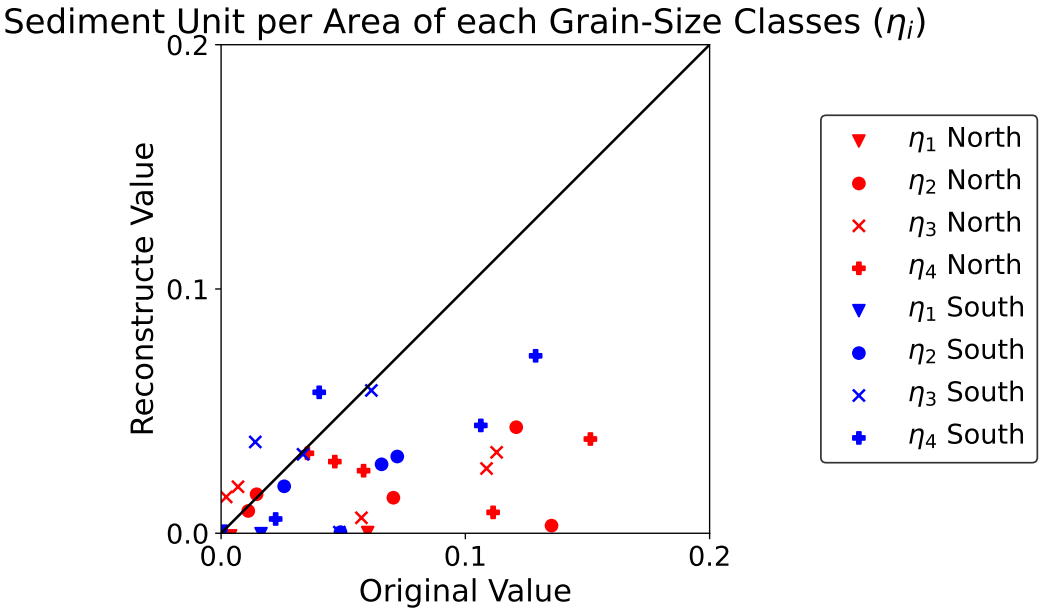

Figure 3.28: Scatter plot of reconstructed vs measured deposit thickness η_{s1}, η_{s2}, η_{s3}, and η_{s4} at each outcrop locations with h_r set to 25 m.

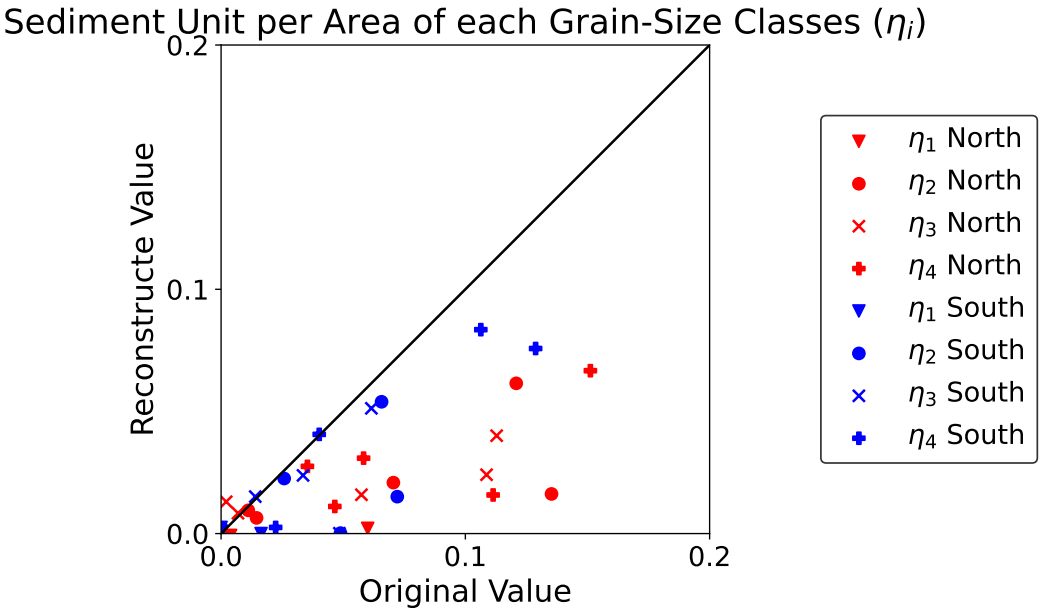

Figure 3.29: Scatter plot of reconstructed vs measured deposit thickness η_{s1}, η_{s2}, η_{s3}, and η_{s4} at each outcrop locations with h_r set to 50 m.

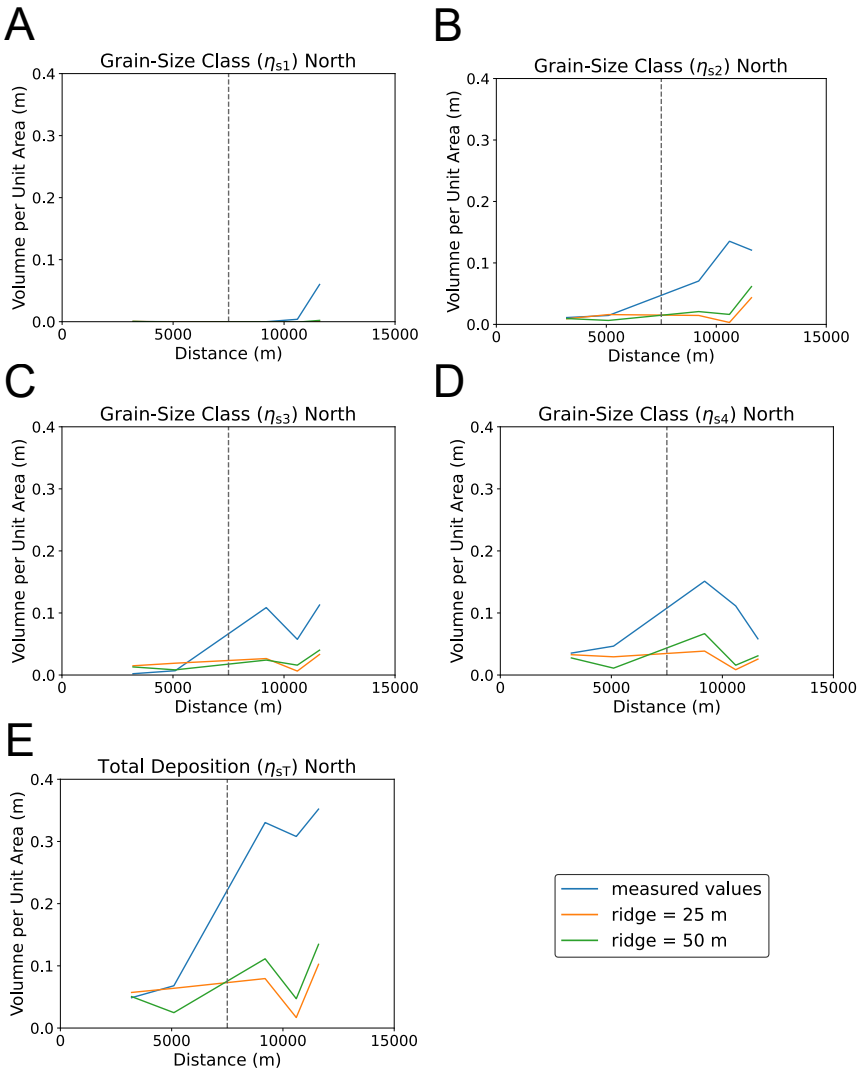

Figure 3.30: Reconstructed deposit thickness north of the ridge for measured and h_r set to 25 m and h_r set to 50 m. The gray dotted line indicates the center of the canyon outlet. A. Reconstructed deposit profile η_{s1}. B. Reconstructed deposit profile η_{s2}. C. Reconstructed deposit profile η_{s3}. D. Reconstructed deposit profile η_{s4}. E. Reconstructed deposit profile η_{sT}.

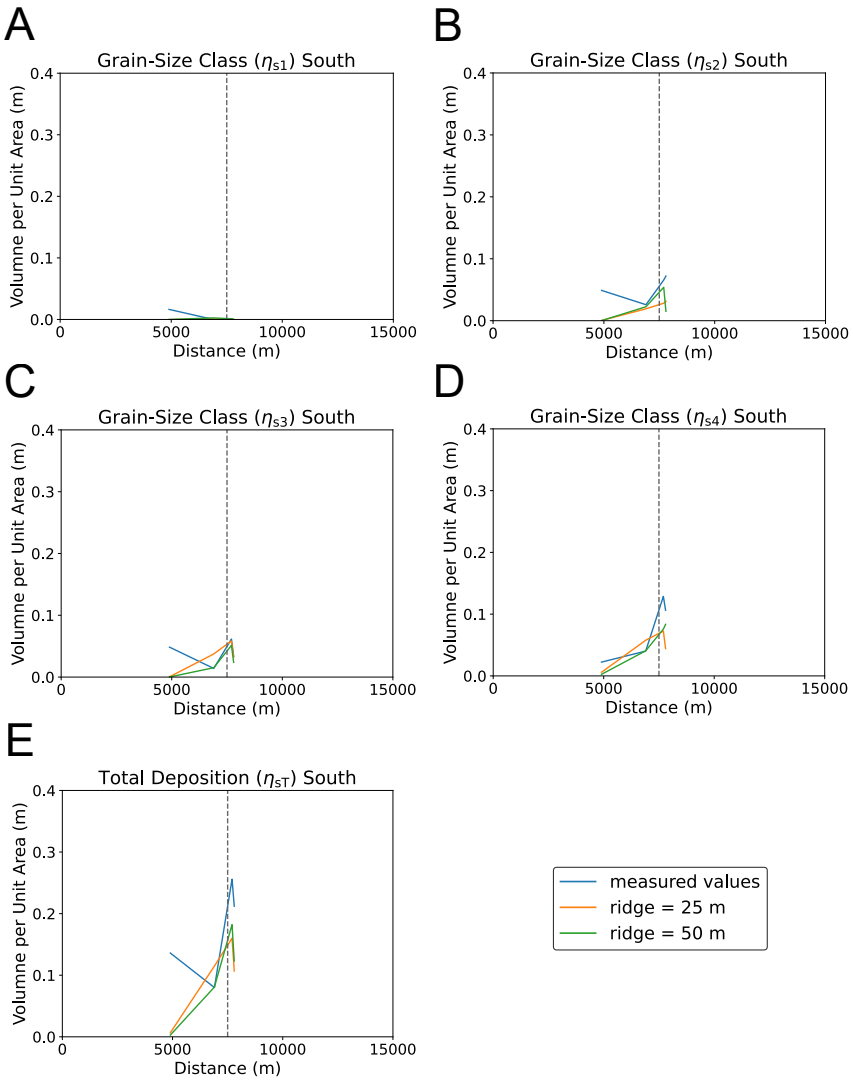

Figure 3.31: Reconstructed deposit thickness south of the ridge for measured and h_r set to 25 m and h_r set to 50 m. The gray dotted line indicates the center of the canyon outlet. A. Reconstructed deposit profile η_{s1}. B. Reconstructed deposit profile η_{s2}. C. Reconstructed deposit profile η_{s3}. D. Reconstructed deposit profile η_{s4}. E. Reconstructed deposit profile η_{sT}.

3.6 Discussion

3.6.1 Inverse Analysis of Artificial Datasets

The ability of the DNN model to reconstruct the hydraulic conditions of turbidity currents from the characteristics of turbidites deposited in the current basin setting was verified in this study. The small values of bias B and sample standard deviation s imply that the initial conditions of the turbidity currents tested in this case were reasonably reconstructed (Tables 3.4 and 3.5). Correlations between the actual and reconstructed values were observed for all parameters. Some outliers were observed for the reconstructed parameters, but most of the reconstructed values were close to the perfect reconstruction line. The range of misfit ($2s$) of all parameters was below 36.2% of the matching representative value for ridge height h_r = 25 m case, and below 29.3% for h_r = 25 m case other than H_{ini} (48.6%) (Tables 3.4 and 3.5). As relatively greater degree of scattering can also be observed for H_{init} of h_r = 50 m case in Figure 3.16B.

Concerning the estimation bias, zero was included in the 95% CI of bias for most of the parameters, proving that the reconstructed values were not significantly biased with respect to the original values. Even among parameters where statistically significant biases were detected, their deviations were minor compared with the representative values of the parameters (Tables 3.4 and 3.5). For example, the estimation bias B for H_{init} had a negative value and the range of the CI of B was below zero for both h_r = 25 m and h_r = 50 m cases (Tables 3.4 and 3.5), indicating a tendency of underestimation for H_{init} overall. However, the bias for H_{init} was only 2.76% of the representative value of this parameter (525 m) for the h_r = 25 m case and 1.20% for the h_r = 50 m case.

Based on the reasons mentioned above, the DNN inverse model together with the two-dimensional forward model proved to be suitable for estimating the paleo-hydraulic conditions of turbidity current that deposited the target turbidite q_t in the Anno Formation. Correlation between reconstructed parameters and original values did not show any signifi-

cant bias, implying that the inverse model developed in this study served as a high precision, high accuracy estimator of flow conditions in this case.

3.6.2 Inverse Analysis of Outcrop Datasets

Examining the reconstruction when applied to actual outcrop samples, the ridge height h_r = 50 m case performed better than the h_r = 25 m case, since more values lay close to the line of perfect reconstruction for the h_r = 50 m case shown in Figure 3.29 than for the h_r = 25 m case shown in Figure 3.28. The root mean squared error J of the two cases, which was 0.002417 for the h_r = 25 m case and a smaller value 0.001904 for the h_r = 50 m case. For both cases, even though the reconstructions of deposit thickness were not entirely accurate in Figures 3.29 and 3.15, the reconstructed deposit thickness was very close to the measured values in the southern part of the basin (Figure 3.31). For the northern part of the basin, the reconstructed deposit thickness was not as accurate as the southern part, but does follow the same trend as the measured values from west to east (Figure 3.30). Reconstructions of values away from the locations close to the channel outlet were relatively accurate, while values at the locations close to the channel outlet were largely underestimated. This might be due to limitation of the lock-exchange initiation setting, because unlike continous flow, flow velocity and flow depth decrease very quickly in a lock-exchange setting. This caused the flow to drop a large portion of sediment in the channel before entering the basin, leaving deposit thickness in basin realtively thin. To accurately reconstruct the thickness of measured values directly downstream the channel outlet, a initiation criteria sustaining a realtively high flow velocity and flow depth as the flow enters the basin, such as a continous flow, may be required.

Looking at the time evolution of calculation for the better reconstructed h_r = 50 m case in Figure 3.27, even though flow parameters near the initiation region in channel were very high under the current lock-exchange setting, the parameters did decrease as it went down the channel and came within a reasonable range as it entered the basin. Total flow

concentration (Figure 3.27C) was initially around 0.08 as it entered the basin but soon dropped to below 0.02 before reaching the ridge, which was a reasonable value for turbidity currents [*Konsoer et al.*, 2013]. Peak flow velocity was around 15 m/s around the head as the flow entered the basin, which was higher than the transit velocity of 4.8 to 5.3 m/s measured for Monterey Canyon [*Paull et al.*, 2018] and the peak velocity 1.5 m/s measured for Congo Canyon [*Azpiroz-Zabala et al.*, 2017b], but was too far from the 10 m/s in [*Konsoer et al.*, 2013]. Flow depth in the northern part of basin (Figure 3.25A) was around 15 m as it first entered the basin, and 1 m after crosing to the southern part of basin (Figure 3.26). The value in the northern part of basin was realistic in comparison to the estimate for natural flow in *Konsoer et al.* [2013]. The value in the southern part of basin was relatively small in comparison to natural flow, especially considering the flow depth of turbidity currents measured in the Monterey Canyon [*Paull et al.*, 2018], which started with flow depth of $<$ 10 m and evolved to $>$ 30 m. Even higher, turbidity current measured in the Congo Canyon reached around 60 m in flow depth [*Azpiroz-Zabala et al.*, 2017b].

Overall, although the reconstructed deposit thickness at the outcrops were not entirely accurate, the recontructed time evolution of flow and the eventual deposit profile north and south of the ridge does provide valueable insights into the fact that a flow velocity much higher than the current reconstructed flow velocity in order to recontructed the measured deposit thickness directly downstream the channel outlet. Considering the peak flow velocity as it entered the basin was already relatively high in comparison to the measured values at the Congo Canyon and the Monterey Canyon, the value was not above the flow velocity of 19 m/s estimated for the turbidite-forming turbidity current triggered by the 1929 Grand Banks earhtquake [*Piper et al.*, 1988]. To future improvement the accuracy of reconstruction for this model, a continous flow initiation condition can be implemented to resolving the difficulties identified in the current lock-exchange initiating condition.

3.7 Conclusion

In this study, the inverse analysis using the DNN model was applied to actual turbidite sampled from outcrops of the Anno Formation, located in Chiba, Japan. Numerical simulation and reconstruction by the inverse model were conducted in an artificial basin that has a ridge in the center, dividing the basin into the northern and the southern part. The reconstruction of artificial datasets was high in precision judging by the standard deviation and bias of the reconstructed parameters. In terms of the application of the DNN model to the actual outcrop data sampled, the deposit thickness was well reconstructed for the southern part of the basin, but underestimation was observed for the northern part of the basin, especially toward the center of the basin, close to the outlet of the channel.

The forward and inverse modeling were conducted for two cases, one with ridge height $h_r = 25$ m and another with $h_r = 50$ m. The inverse analysis result proved $h_r = 50$ a better setting for the reconstruction, since the root mean squared error J of the reconstructed deposit thickness for all grain-size classes was lower for the $h_r = 50$ m case. The flow conditions of the reconstructed flow as it enters the basin were compared with measured values from previous direct measurements of turbidity currents, and the reconstructed values were well within the reasonable range.

Overall, the DNN model exhibited good performance for the inversion of artificial datasets and part of the deposit thickness of the sampled outcrop data, demonstrating the success of the DNN model in exploring the functional relationship between the parameters describing the initiation region of flow and the resulting deposits. The result of application to sampled outcrop data indicates that the DNN model was competent in performing inverse analysis on turbidites from outcrop samples, but a continuous flow initiation setting may be more suitable for application in this case, which should be the next goal in advancing the model. Improving the accuracy of the DNN model for application to field datasets will be the next goal.

Appendix

Measured and reconstructed grain size distributions at each sampled outcrop are shown in Figures 3.32A-I.

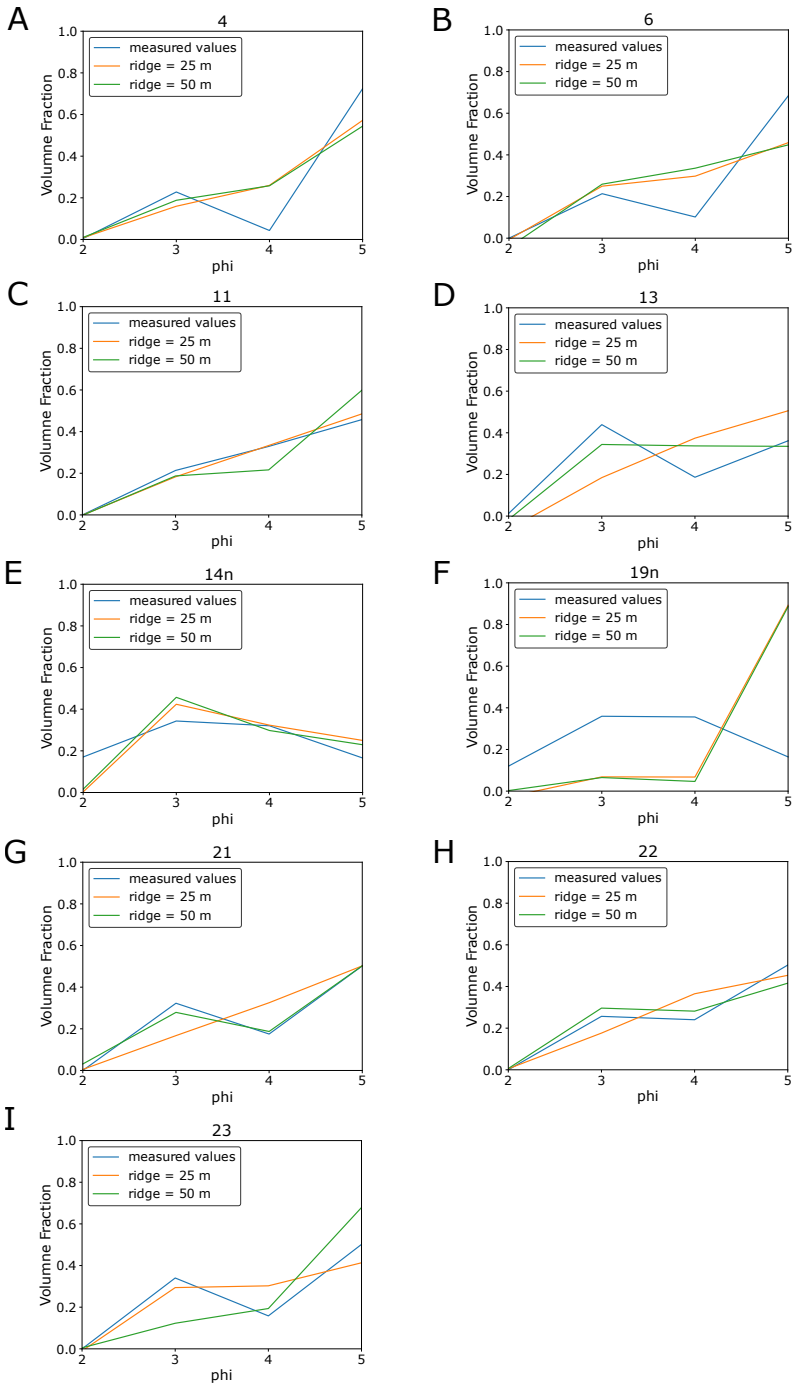

Figure 3.32: A. Grain size distribution at Outcrop Number 4. B. Grain size distribution at Outcrop Number 6. C. Grain size distribution at Outcrop Number 11. D. Grain size distribution at Outcrop Number 13. E. Grain size distribution at Outcrop Number 14n. F. Grain size distribution at Outcrop Number 19n. G. Grain size distribution at Outcrop Number 21. H. Grain size distribution at Outcrop Number 22. I. Grain size distribution at Outcrop Number 23.

Chapter 4

Preliminary Test of Two-Dimensional Inverse Modeling of Turbidity Currents in Japan Trench

4.1 Introduction

Earthquakes and tsunamis are catastrophic geohazards that bring destruction to cities and sometimes countries. The 2011 Mw 9.0 Tohoku-Oki earthquake left especially strong traces in Japan. Other than the 2011 Tohoku-Oki earthquake, historical record shows that the Jogan earthquake (AD896) happened just around 1100 years before the Tohoku-Oki earthquake [*Minoura and Nakaya*, 1991; *Sawai et al.*, 2012]. The recurrence interval of mega-earthquake occurrence has long been a topic of focus due to its close association with the risk assessment of natural hazards. The historical records and tsunami deposits in terrestrial regions are valuable sources of information for estimating the recurrence intervals of the past mega-earthquakes. However, both of these records face the challenge of preservation over a long period. The historical record can only go as far back as around 1500 years in the past, while tsunami deposits on land are very susceptible to erosion and deformation.

To solve the problems faced with the two methods above, *Goldfinger et al.* [2003] proposed the use of seismo-turbidite as an indicator of earthquakes. Seismo-turbidite are deposits of turbidity currents induced by the seismic activities and can be identified as a potential marker for seismic events in sedimentary records. It was found in the previous study

that ground-shaking by earthquakes had been identified as causes of large-scale remobilization of sediment [*Oguri et al.*, 2013; *Kioka et al.*, 2019]. In addition, tsunamis can entrain basal sediment on the continental shelf, suspending them to generate turbidity currents. Indeed, Arai et al. (2013) reported that the turbidity current occurred three hours after the 2011 Tohoku-Oki Earthquake and transported the ocean bottom pressuremetry settled on the 1000-m deep seafloor. The result from coring the area around the Japan Trench by *Ikehara et al.* [2016] showed an interval of around 1500 years between the sedimentary records of mega-earthquakes by seismo-turbidites, which matched with the historical documents of the Jogan earthquake.

Even though seismo-turbidites proved to be a good indicator of earthquake records in sedimentary successions, there is one major problem that needs to be resolved. That is how to determine the scale of the seismic event that deposited the seismo-turbidite. The goal of hazard prevention is to identify the frequency of events that may affect human activities on land, not any seismic activity. Since earthquakes of greater magnitude cause greater amount of shaking, turbidity currents triggered by these events are likely to be higher in flow velocities, flow depths, or flow concentrations. Thus, in order to identify an event of magnitude high enough to pose a severe threat to human society, it is necessary to reconstruct these flow properties of turbidity currents from the deposit characteristics.

To resolve the problem mentioned, this study proposes the inverse modeling of seismo-turbidites. An inverse model for turbidity currents proposed by *Naruse and Nakao* [2021] was tested with flume experiments and had been applied to tsunami deposits. The results were successful in previous studies by *Mitra et al.* [2020] and *Cai and Naruse* [2021], indicating it an optimistic for application to the seismo-turbidites deposited in the Japan Trench. As mentioned above, Japan Trench has a relatively accurate historical record of past mega-earthquakes *Usami* [1987], a factor essential in determining the age of past mega-events. Thus, it is the ideal study area as the first location for testing the performance of the DNN model on seismo-turbidites deposited in nature.

This chapter shows a preliminary test with artificial datasets of cores at the study sites of IODP Expedition 386 in a Japan Trench topographic setting. For studying the frequency of mega-earthquakes from sedimentary records, IODP Expedition 386 Japan Trench Seismology was established to core the Japan Trench area. In this study, we used 2D numerical simulation and the submarine topography of the region to examine the behavior of turbidity currents resulting from the large area of submarine failure.Then, DNN inverse analysis was tested to determine whether it can reconstruct the location and the scale of the initiation region of turbidity currents resulting from mega earthquakes. In the future, the hope is to conduct an inverse analysis of the actual cores taken by IODP Expedition 386 to understand the hazard risks in this region.

4.2 Topographic Settings and the Study Sites

The Japan Trench is an active subduction margin offshore of the Tohoku area of Japan, where the Pacific Plate subducts below the Okhotsk Plate at a rate of 8.0 to 8.6 cm/yr toward the NW direction [*DeMets et al.*, 2010]. Horst-graben structures are observed for the subducting Pacific Plate. Forearc basins are not observed along the Japan Trench, but tectonic subsidence occurs along the trench due to subduction erosion [*von Huene and Lallemand*, 1990]. Gently sloped upper slope terrace and some isolated basins formed as a result of tectonic subsidence [*Arai et al.*, 2013]. The average slope angle of the lower slope was reported to be around 5 degrees by *von Huene and Lallemand* [1990]. A few canyon systems are identified in the northern part of Japan Trench, but no canyons were observed to connect to the trench floor near the central part of Japan Trench offshore Sendai. The water depth of Japan Trench increases from north to south, starting with 6800 m toward the north and greater than 7500 m moving toward the central and southern region [*Ikehara et al.*, 2016].

IODP Expedition 386 Japan Trench Seismology aims to identify the deposits of Mega-

earthquakes that happened in the past. 18 primary sites and 13 alternate sites were proposed for coring for this purpose. Both the primary and alternate sites are shown in Figure 4.1. In this study, the preliminary testing of inverse modeling at Japan Trench was conducted using the artificial deposits sampled from these points.

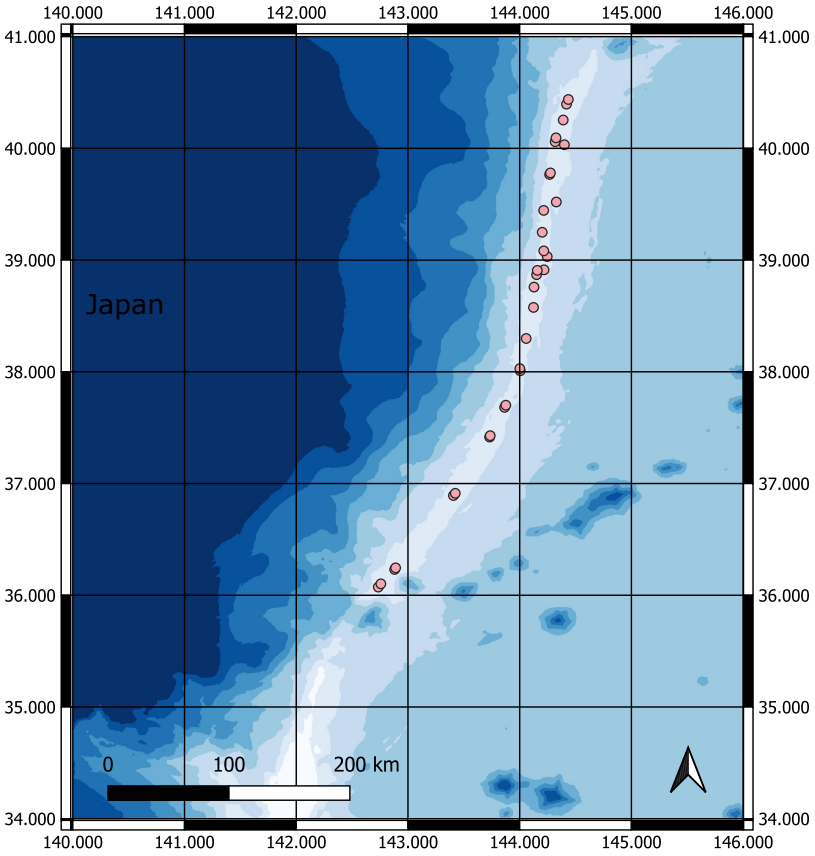

Figure 4.1: Map of Japan Trench showing the change in water depth within the area of interest.

4.3 Methods

4.3.1 Numerical Modeling of Japan Trench

Implementation of Forward Model

Numerical model described in Chapter 3 Sections 3.3.1 and 3.3.2 was used for the forward modeling of this study. For implementation, the CIP-combined and unified procedure (C-CUP) method [*Yabe and Wang*, 1991], a third order accurate scheme, was used for integrating Equations 3.1, 3.2, 3.3, and 3.4. Neumann-type artificial viscosity was implemented with C-CUP for shock capturing with ν_a set to 0.75 [*Ogata and Yabe*, 1999]. Time step Δt was initialized to 0.1 for the first time step, then calculated using the following equation for later time steps:

$$\Delta t = \alpha \frac{\Delta x}{\max(\max(|U| + C_{\mathrm{s}}), \max(|V| + c_{\mathrm{s}}))}, \tag{4.1}$$

$$c_{\mathrm{s}} = \sqrt{RgC_{\mathrm{T}}H}, \tag{4.2}$$

where c_{s} is wave celerity. Parameter α is the Courant number, which was set to 0.4 in this study. To stabilize the calculation, a second order artificial viscosity was implemented using the scheme by *Jameson et al.* [1981], where the parameter κ_{a} was set to 0.05. The fractional step method was used to solve Equations 3.5 and 3.6. Interval of spatial grids is the same in x- and y-direcitons ($\Delta x = \Delta y$).

In this study, the calculation domain was rectangular with W_{topo} (m) and L_{topo} (m) as the width (lateral x-direction) and the length (longitudinal y-direction). The topography was generated from a Geotiff map with data points in UTM coordinate system and the calculation domain was chosen within the generated topographical region. The values of W_{topo} and L_{topo} were calculated from the UTM coordinates at the four corners of the calculation domain, which were 510000.0 m and 714000.0 m for this study. The number of grids in the latitudinal direction G_{x} was 250. The number of grids in the longitudinal direction G_{y} was 350. The total number of grids was G_{x} x G_{y}. The grid spacing Δx (=Δy) was calculated by

Δx=$L_{\mathrm{topo}}/G_{\mathrm{x}}$, which was calculated to be 2040.0 m. All four boundaries of the calculation domain were set to Neumann boundary condition.

A lock-exchange setting was used for the initiation of flow, where a rectangular region with width $r_{\mathrm{x,init}}$, length $r_{\mathrm{y,init}}$, height H_{init}, and concentrations of each grain size class $C_{\mathrm{init},i}$ ($C_{\mathrm{init,T}} = \sum C_{\mathrm{init},i}$) was inputted as initial conditions. The location of the rectangular initiating region within the calculation domain was also inputted as an initial condition, which was determined by W_{init} m and L_{init} m. Parameter W_{init} was the distance of the center of the rectangular initiating region from the southern edge toward the north and L_{init} was the distance from the western edge toward the east within the calculation domain.

Parameter $F_{i,0}$, the initial volume fraction of the ith grain-size class in the active layer, was set to 1/N for all grain-size classes, where N represents the number of grain-size classes. Other than the initiating region, all other grids had flow parameters initialized to zero. The wet-dry boundary condition at the head of the flow was conducted using the scheme proposed by *Yang et al.* [2016]. Threshold values of $C_T H$ and H, ε and H_{w}, was used to determine the position of the waterfront. If $C_T H \geq \varepsilon$ and $H \geq H_{\mathrm{w}}$, the grid was wet. If and $H < H_{\mathrm{w}}$ or $C_T H < \varepsilon$, the grid was dry. In this study, ε and H_{w} was set to 0.00001 and 0.001, respectively. A dry grid adjacent and downstream to a wet grid was a partial wet grid. Flow discharge M at a partial wet grid j was calculated using Homma's equation [*Yang et al.*, 2016] as follows:

$$M = C_{\mathrm{s}} H_{j-1} \sqrt{R g C_{\mathrm{T},j-1} H_{j-1}}, \tag{4.3}$$

where the discharge coefficient C_s is equal to 0.35.

The number of grain-size classes and representative grain diameter D_i for each grain-size class were determined on the basis of the grain size distribution measured from samples. In this study, the number of grain-size classes was 4 and D_i for grain-size classes 1, 2, 3, 4 were 250, 125, 62.5, and 31.3 μm, respectively. The density of the surrounding fluid ρ_{f} was set to 1000.0 kg/m^3 in this study. The submerged specific density of sediment

$R = (\rho_s - \rho_f)/\rho_f$, where ρ_s, the density of sediment particles, is 2.65 g/cm^3. The porosity of bed sediment λ_p was assumed to be 0.4. The friction coefficient c_f was set to 0.004 and the ratio of near-bed concentration to layer-averaged values r_o was set to 1.5 [*Kostic and Parker*, 2006]. Dynamic viscosity μ was 0.00101 Pa*s, an experimentally determined of μ at 20.0°C [*Rumble*, 2018]. Constant p for the calculation of e_{si} is 0.1 in this study, since the calculation will be conducted with a field scale setting [*Fildani et al.*, 2006]. In addition, the thickness of active layer L_a was set to be a constant, 0.01 m. The gravitational acceleration g was 9.81 m/s^2.

Sampling from Forward Model Simulation

Simulations were conducted on topography generated from 500 mesh bathymetry data published by the Japan Coastal Guards. The area of simulation generated was from 140.0 to 146.0 Longitude and 34.0 ∘ to 41.0 ∘ Latitude (Figure 4.1) under a UTM projection. Deposits from the forward model simulations were sampled at grids that correspond to the coring locations on the map (Figure 4.1). The coring locations are shown in Table 4.1 in Longitude and Latitude. Same as the coordinates for the area of simulation, these locations were converted to UTM coordinates and used to extract sampling data points from numerical simulations.

4.3.2 Inverse Modeling of artificial datasets of Japan Trench

In this study, inverse analysis of outcrop samples was conducted using a DNN model proposed by [*Naruse and Nakao*, 2021]. Specific implementation was done based on [*Cai and Naruse*, 2021]. As described in Chapter 2 Section 2.3, inverse analysis using DNN consists of four steps. First, artificial datasets of turbidity currents were produced using a forward model. Then, the DNN model was trained using the datasets. After that, the trained DNN model was applied to a separate artificial dataset also produced using the forward model to test its performance for the reconstruction problem proposed. Finally, after performance

Table 4.1: A list of coring sites proposed for the IODP Expeidition 386 Japan Trench Paleoseismology [*Strasser*, 2017].

Core Number	Latitude	Longitude
JTSB-01A	36.07202	142.73503
JTSB-02A	36.10118	142.75813
JTSB-03A	36.22997	142.88166
JTSB-04A	36.24424	142.89031
JTPS-05B	36.89173	143.40772
JTPS-06B	36.91171	143.42432
JTPS-07A	37.41496	143.73196
JTPS-08A	37.42749	143.73726
JTPS-09A	37.6811	143.8661
JTPS-10A	37.70031	143.87689
JTPC-01A	38.00853	144.00566
JTPC-02A	38.02804	144.00227
JTPC-03B	38.29761	144.0592
JTPC-04A	38.57586	144.12499
JTPC-05A	38.75801	144.12942
JTPC-06B	38.8692	144.15224
JTPC-07A	38.91249	144.21916
JTPC-08A	39.03126	144.24752
JTPC-09A	39.08195	144.21682
JTPC-10A	38.90768	144.15905
JTPN-01A	39.24858	144.20297
JTPN-02A	39.44436	144.2163
JTPN-03A	39.519797	144.32902
JTPN-04A	39.76647	144.2691
JTPN-05A	39.78013	144.27636
JTPN-06A	40.0594	144.31855
JTPN-07A	40.09392	144.32612
JTPN-08A	40.03244	144.4011
JTPN-09A	40.39568	144.42047
JTPN-10A	40.43742	144.43687
JTPN-11A	40.25341	144.39081

proved to be good when tested with artificial datasets, the trained inverse model was applied to the actual data measured from outcrop samples.

Production of Training Datasets

The training datasets for this study were a combination of randomly generated values for the parameters of the initiation region of flow in numerical simulations. A program in Python was written to generate sets of initial flow conditions. Each set of values generated consists of height of the initiation region H_{init}, widths for x and y coordinates of the flow initiation region $r_{\mathrm{x,init}}$, $r_{\mathrm{y,init}}$, the concentrations of each grain-size class in the initiation region $C_{\mathrm{init},i}$, and the location of the center of initiation region indicated by W_{init} and L_{init}.

The forward model calculates the deposited turbidite distribution and thickness within the artificial basin using randomly generated initial conditions. The deposited turbidite was calculated as thickness without porosity at the 12 coring locations within the calculation domain. The calculation domain was divided into G_{x} times G_{y} number of grids, where data points of deposits at grids are akin to sampled data from an actual turbidite at the coring sites. Table 4.2 illustrates the ranges of randomly generated initial conditions. These ranges were decided based on possible values that can be observed in natural scale turbidity currents. In this study, 100 training datasets were used for training and 10 datasets were used for verifying the DNN (Section 4.4.2). The number of test datasets was chosen to be the same number as that of validation datasets. The test numerical datasets for verification were generated independently from the training datasets.

DNN Inverse Model Settings

The DNN inverse model was implemented using the same structure as in [*Cai and Naruse*, 2021], but with different input nodes, output nodes, and hyperparameter settings. In this study, nodes in the input layer held deposit values, i.e., the deposit thickness for all grain-size classes at spatial grids. Nodes in the output layer held estimates of parameters to be

Table 4.2: Range of initiation region parameters generated for production of training datasets.

Parameter	Minimum	Maximum
H_{init} (m)	30.0	80.0
$r_{x,\text{init}}$ (m)	2500.0	3000.0
$r_{y,\text{init}}$ (m)	3000.0	4000.0
$C_{\text{init},i}$	0.01	0.05
W_{init} (m)	230000	250000
L_{init} (m)	390000	410000

reconstructed, which in this case are H_{init}, $r_{\text{x,init}}$, $r_{\text{y,init}}$, $C_{\text{init},i}$ and W_{init} and L_{init}. Hyperparameters dropout rate, validation split, and momentum for the DNN model were set to 0.5, 0.2, and 0.9, respectively. The learning rate was set to 0.01. The batch size was set to 32 and the number of layers was set to 3. The number of nodes in each layer was 500. Epoch was 1000. Calculations were performed using GPU NVIDIA GeForce GTX 1080 Ti.

Evaluation of Inverse Model

For the evaluation of the DNN model with artificial datasets (Section 4.4.2), the reconstruction result of each parameter was evaluated using bias (B) and sample standard deviation (s) of residuals. The calculations were performed using the following equations:

$$B = \frac{\sum x_i}{n}, \tag{4.4}$$

$$s = \sqrt{\frac{\sum (x_i - B)^2}{n-1}}, \tag{4.5}$$

where n represents the number of test datasets, and x_i denotes the residual of the specific reconstructed parameter for the ith test dataset. The value of s for each reconstructed parameter was compared with a representative value C_v^*, which is the mid-value over the range in which the specific parameter was generated (Table 4.2). The confidence interval of B was determined using the bootstrap resampling method [*Davison and Hinkley*, 1997]. Resampling of B was conducted 1000 times, and the 95% confidence interval (CI) of B was determined.

4.4 Result

4.4.1 Numerical Experiments of Japan Trench

Three cases of numerical experiments were conducted with varied locations of initiation region, which was defined by W_{init}, and L_{init} (Table 4.3). The three cases were conducted with initation area at a northern, a central and a southern location off shore Sendai. Initial regions parameters H_{init} (m), $r_{\mathrm{x,init}}$, $r_{\mathrm{y,init}}$ and $C_{\mathrm{init,i}}$ set to constant values. The time evolution of the distribution of flow height H for the Cases 1 and 2 are shown in Figures 4.2 and 4.3. As the location of iniital flow region shifted from north to south, the area of distribution of flow also shifted in the same direction.

Table 4.3: Initiation region parameters for numerical experiments of turbidity currents.

Parameter	Case 1	Case 2
H_{init} (m)	55.0	55.0
$r_{x,\mathrm{init}}$ (m)	2570	2570
$r_{y,\mathrm{init}}$ (m)	3500	3500
$C_{\mathrm{init},i}$	0.03	0.03
W_{init} (m)	230000	390000
L_{init} (m)	250000	410000

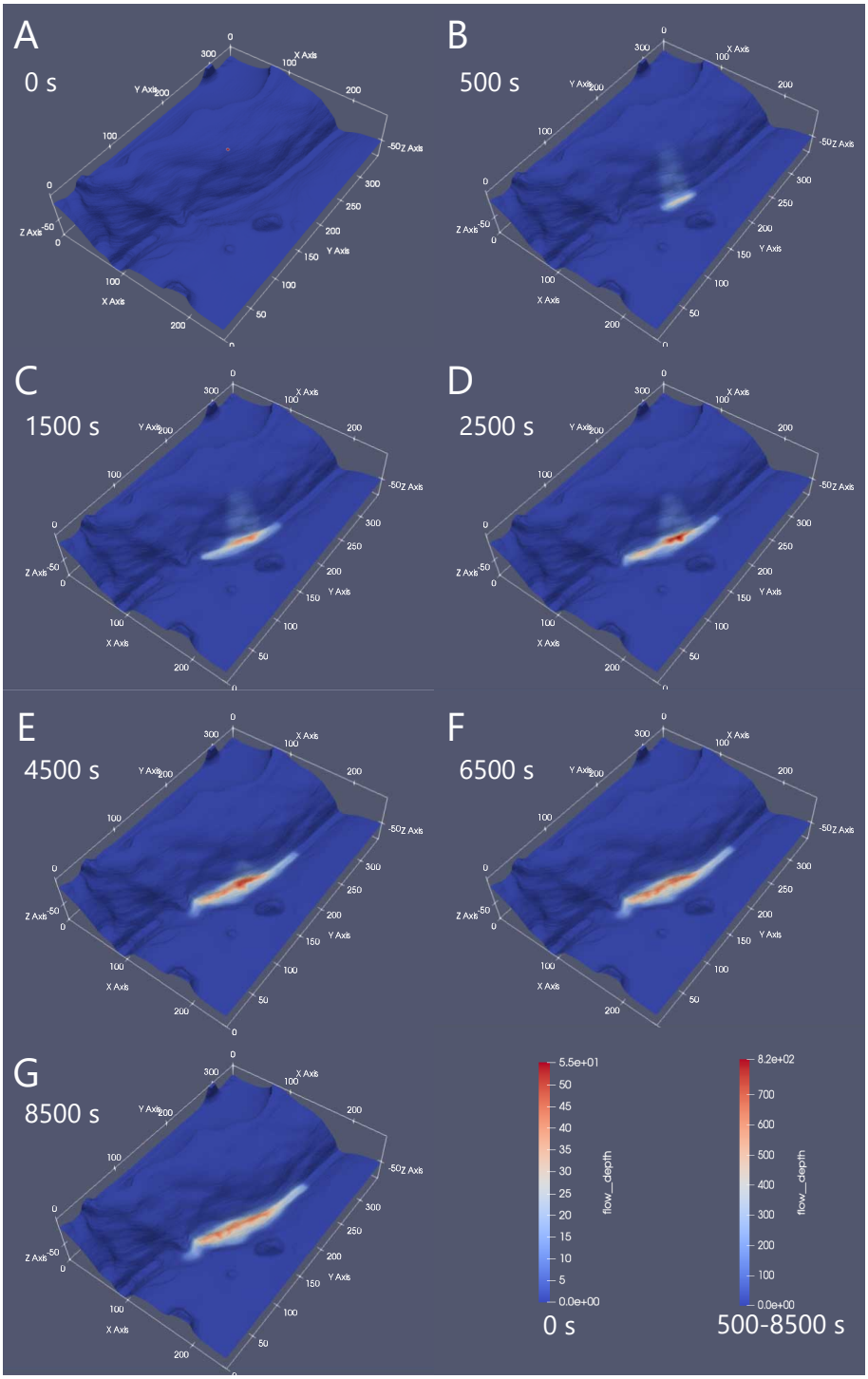

Figure 4.2: Time evolution of flow depth H over time for Case 1.

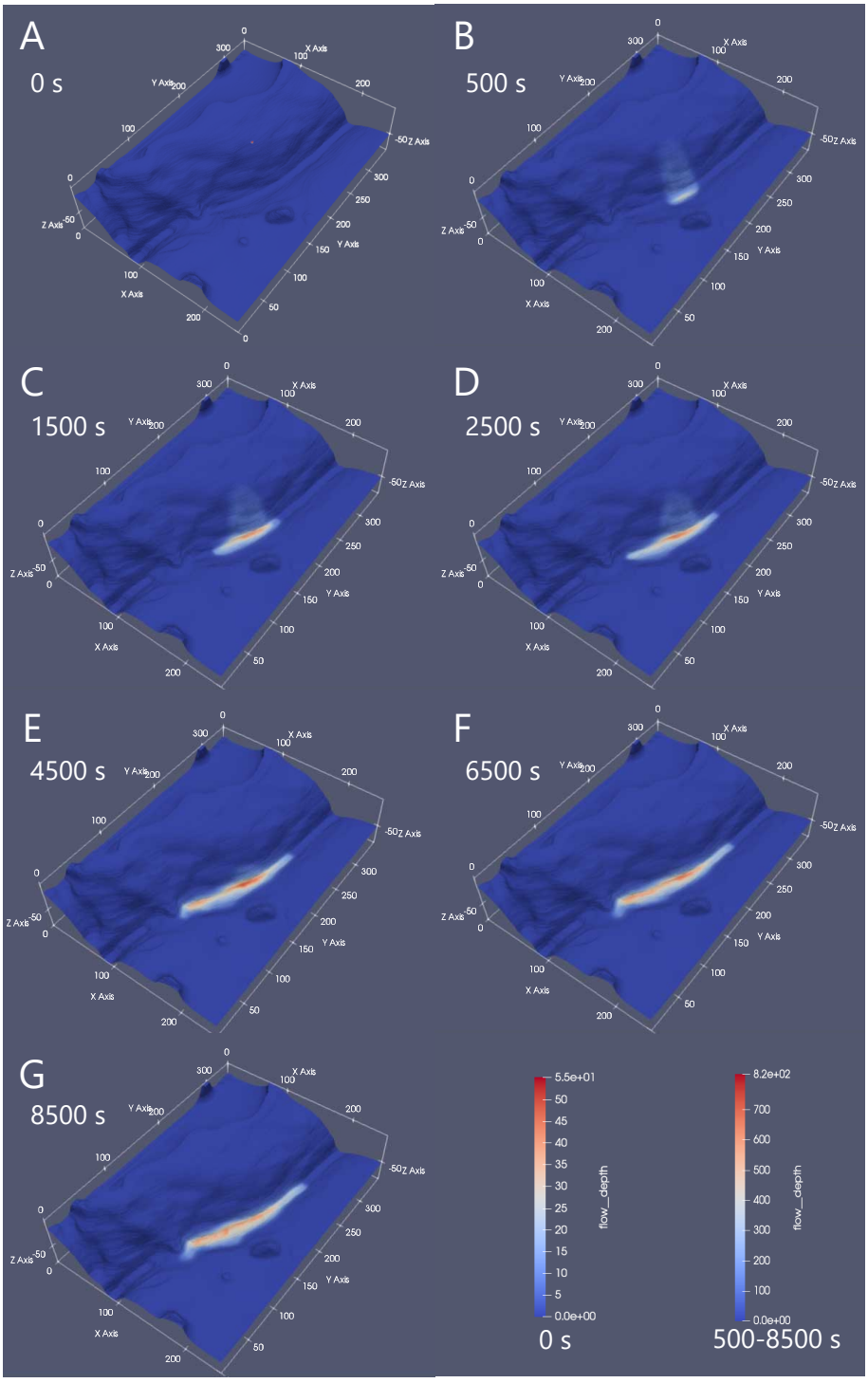

Figure 4.3: Time evolution of flow depth H over time for Case 2.

4.4.2 Inverse Modeling of Japan Trench

The training of the DNN model ended with validation loss of 0.013 for training datasets. Figures 4.4A shows that overlearning occurred after about the 600th epoch, and significant deviation was observed between the resulting values of the loss functions for the training and validation datasets. Overall, the reconstructed values matched reasonably with the original values (Figure 4.4B-J), although the geometry of the initial flow region (initial flow depth and widths for X and Y axis) was not estimated precisely. The ranges of misfit ($2s$) was relatively large, with $2s/C_v^*$ between 1.45% and 68.6% for the parameters reconstructed. Parameters indiating the initiation location, W_{init} and L_{init} had the lowest $2s/C_v^*$ values (Table 4.4). For all parameters, zero was within the 95% CI of B.

Table 4.4: Sample standard deviation and bias of the inversion result for numerical datasets of Japan Trench.

Parameters	s	C_v^*	$2s/C_v^*$	B	CI of B
H_{init} (m/s)	9.64	55	0.351	1.09	(-3.02, 5.17)
$r_{\mathrm{x,init}}$ (m)	136	2750	0.0986	-27.7	(-76.8, 4.47)
$r_{\mathrm{y,init}}$ (m)	320	3500	0.183	-108	(-215, 6.75)
$C_{\mathrm{init},1}$	0.0103	0.03	0.686	0.00221	(-0.00270, 0.00391)
$C_{\mathrm{init},2}$	0.0080972	0.03	0.540	-0.0000971	(-0.00492, 0.00458)
$C_{\mathrm{init},3}$	0.00682	0.03	0.455	0.00244	(-0.00237, 0.00513)
$C_{\mathrm{init},4}$	0.00505	0.03	0.337	-0.000169	(-0.00156, 0.00202)
W_{init} (m)	5090	240000	0.0424	-386	(-2460, 1300)
L_{init} (m)	2920	400000	0.0145	-482	(-2130, 336)

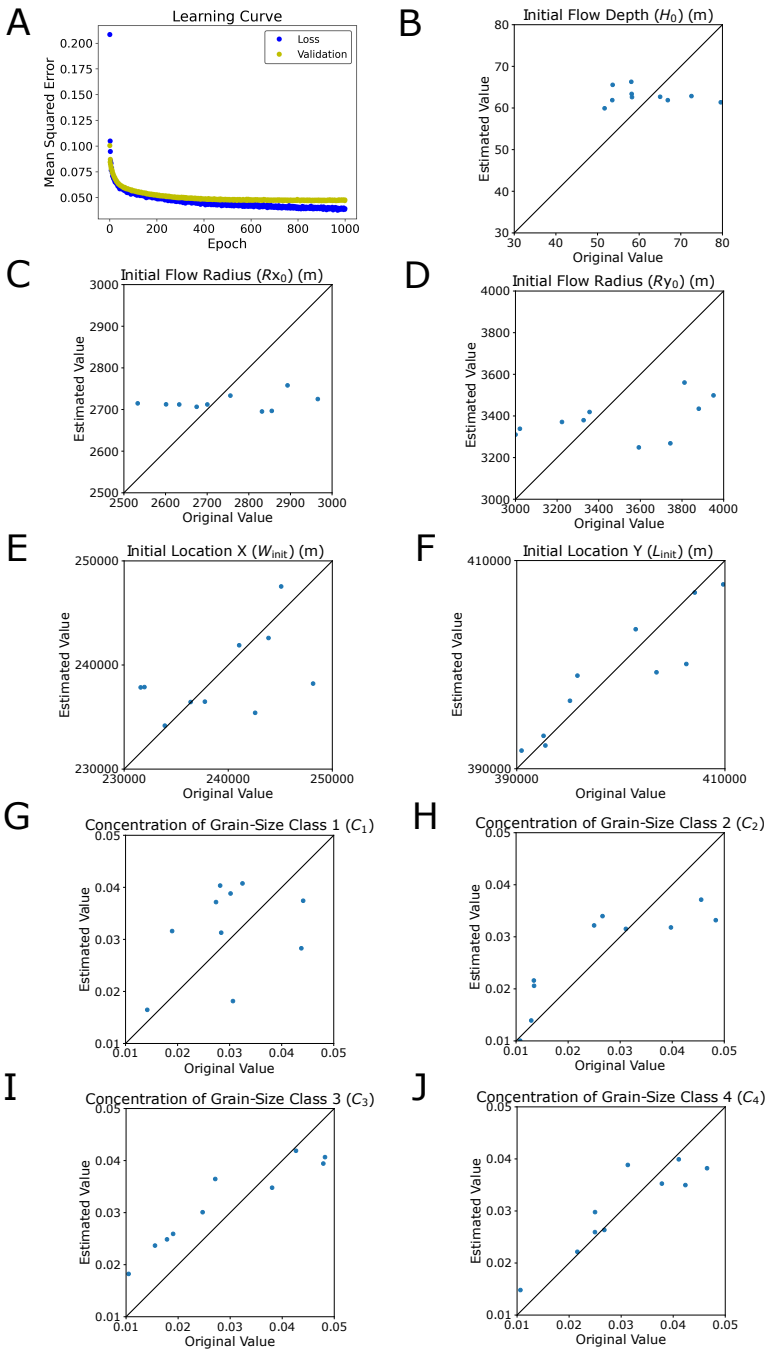

Figure 4.4: Results of inverse analysis of artificial datasets of turbidite from Japan Trench. The black diagonal line in each graph is where values on the x-axis (the true values) equal to the values on the y-axis (the estimated values). If a point lies on this line, the reconstructed value matches the true value perfectly. A. Learning curve. B. Estimates of H_{init}. C. Estimates of $r_{\mathrm{x,init}}$. D. Estimates of $r_{\mathrm{y,init}}$. E. Estimates of W_{init}. F. Estimates of L_{init}. G. Estimates of $C_{\mathrm{init},1}$. H. Estimates of $C_{\mathrm{init},2}$. I. Estimates of $C_{\mathrm{init},3}$. J. Estimates of $C_{\mathrm{init},4}$.

4.5 Discussion

As shown in Figure 4.4A, overlearning occurred during the training process of the DNN model. The reason that overlearning occurred so quickly during the training process was most probably due to the small number of training datasets. The reconstructed values were very scattered from the line of perfect reconstruction, and the s and B values indicate a less than ideal reconstruction (Table 4.4). However, even with the significant overlearning, the reconstruction of location of the initial flow region W_{init} and L_{init} are aligning with the line of perfect fit. It looks optimistic for reconstruction with an increase in training datasets (Figures 4.4E, F). The same trend can be observed from concentrations of grain-size classes 2 to 4, which also shows a possibility for reconstruction (Figures 4.4H, I, J).

Even though it now resulted in overlearning, the reconstruction of W_{init} and L_{init}, $C_{\mathrm{init},2}$, $C_{\mathrm{init},2}$, and $C_{\mathrm{init},2}$ seemed optimistic for the reconstruction with an increase in the training dataset. The DNN inverse model together with the two-dimensional forward model is potentially suitable for estimating the paleo-hydraulic conditions of turbidity current that deposited the turbidites in the Japan Trench. Even with the scattering of values, the correlation between reconstructed parameters and original values did not show any significant bias, implying that the inverse model developed in this study served as a high precision, high accuracy estimator of flow conditions in this case.

4.6 Concluding Remarks

Overall, a preliminary test of inverse analysis of artificial core data using topography near the Japan Trench was conducted. Although there are difficulties in estimating several parameters due to the lack of the number of training datasets, the results of the numerical experiments indicate that the locations of the flow initiation and sediment concentrations can be reconstructed by the inverse model with relatively good accuracy. Optimization of forwarding model implementation will be conducted in the future and more training data

will be produced. An eventual application of the method to cores obtained from IODP Expedition 386 will be the eventual goal.

Chapter 5

Conclusion and Future Prospect

5.1 Summary of Findings

The objective of this thesis is to establish the methodology for reconstructing the behavior of turbidity currents from the turbidites deposited. The objective was fulfilled through verification of the DNN inverse model using one-dimensional flume experiments (Chapter 2), application of the DNN inverse model to outcrop samples from the Anno Formation in a two-dimensional basin setting (Chapter 3), and preliminary application of the DNN inverse model to artificial core samples from a Japan Trench topography setting (Chapter 4).

In Chapter 2, the performance of the DNN inverse model proposed by *Naruse and Nakao* [2021] was verified by five sets of flume experiment datasets. The DNN inverse model was able to reconstruct the complete deposit profile and grain size distribution of the flume experiment scale turbidite within a 2.6 m range from 13 samples collected at an interval of 20 cm from the turbidite.

In Chapter 3, the verified DNN inverse model was applied to samples obtained from outcrops of a turbidite bed q_t within the Anno Formation, Boso Peninsula, Chiba, Japan. Samples were obtained from 9 outcrops of q_t spread within a 10 km range around the central Boso Peninsula. The thickness of the bed at each location and the grain size distribution of the samples were used to reconstruct the parameters describing the lock-exchange flow initiation region. The reconstructed parameters were inputted into the forward model to

reproduce the flow that deposited the target turbidite bed q_t. Within the artificial basin used in this study, a ridge divides the basin into a northern and a southern region in the middle. The thickness of q_t was well reconstructed toward the southern region, but deviates for the northern region especially directly downstream the outlet of the channel, where reconstructed deposit thickness was much thinner than the measured values.

In Chapter 4, the testing of the DNN inverse model was conducted for artificial core samples created in the Japan Trench topography setting. Inverse analysis was conducted using a DNN model trained with around 100 artificial datasets and tested with ten independent artificial datasets. The results showed overlearning due to a small number of training datasets used for training. However, even with the less than ideal training of DNN, the reconstruction still showed optimistic results for the reconstruction of the location of the initiation area and the flow concentrations for each grain-size class.

5.2 Importance of This Study

Before this study, there was no established methodology for reconstructing ancient flow behaviors from the turbidites deposited in nature. Generally, outcrops and drilling cores can only provide very limited exposure to a turbidite. A quantitative examination of an entire turbidite bed was deemed impossible. The DNN inverse model was recently proposed by *Naruse and Nakao* [2021] as a method that encourages solving this problem. This study first verified the DNN inverse model with experiments conducted under a controlled setting, then applied and evaluated the model's performance when applied to outcrop samples and artificial core datasets. The verification and application conducted in this study established the methodology of the DNN as an inverse model for turbidity currents. The method applied to the three main types of data collected for studies of turbidites, building a sturdy foundation for the future application of the DNN model to a wide range of localities and datasets.

5.3 Future Research

Future research for perfecting the methodology for reconstructing the behavior of a turbidity current from a turbidite may include three main directions. First, the reconstruction using the DNN inverse model was verified with one-dimensional flume experiments in Chapter 2, but has yet to be verified with two-dimensional flume experiments. The model was applied to two-dimensional flow in Chapter 3 and 4 and its performance were compared with estimated depositional profiles and paleo-flow conditions. However, paleo-flow conditions were only rough estimates based on evidence recovered from sediment deposited, thus not suitable strictly for the evaluation of the model. Depositional profiles from field or core studies were based on interpolation between sampling points. The reconstructed deposit profile cannot be compared directly with the true deposit profile. To have a precise evaluation of the performance of the DNN inverse model with a two-dimensional topography setting, it is necessary to conduct two-dimensional flume experiments and compare measured deposit profile and flow conditions with the reconstructed values.

A second goal in the future should be an advancement in the forward numerical model, considering both deviations in the results of Chapter 2 and Chapter 3 were partly due to imperfections in the forward model. Where one potential problem identified was the layer-averaged model adapted, which ignores the density stratification effect observed in turbidity currents in nature. For Chapter 4, calculation load presented an obstacle in quickly producing a large number of artificial training datasets necessary for improving the precision of the inverse model reconstruction. Future improvements in the numerical scheme used in forwarding model implementation would also be important for the application of the model with high topographical precision or in a wide area.

A third future direction would be improvements in the DNN inverse model. The DNN inverse model is now implemented using a basic fully connected deep neural network (DNN). Tendencies of deviation were observed for some parameters during the testing with

artificial datasets, potentially leading to deviation in reconstructed values. Instead of a fully connected DNN, DNN implemented together with convolutional neural network (CNN) may be able to process the inputs with more flexibility and produce a better reconstruction.

Notation

α_1, α_2	Parameters related to sediment entrainment
B	Bias
c_{f}	Friction coefficient
C_i	Layer-averaged volumetric concentration of suspended sediment of the ith grain-size class
CI of B	95% confidence interval of bias
C_s	Discharge coefficient
C_{T}	Layer-averaged total concentration of suspended sediment
C_v^*	The mid-value over the range in which the specific parameter was generated
D_i	Representative grain diameter of the ith grain-size class
$e_{\mathrm{s}i}$	Entrainment rate of sediment of the ith grain-size class into suspension
e_{w}	Entrainment rate of ambient water to flow
F_i	Volume fraction of the ith grain-size class in active layer
g	Gravitational acceleration
H	Flow depth
L_{a}	Active layer thickness
M	Flow discharge
R	Submerged specific density of sediment
$R_{\mathrm{f}i}$	Dimensionless particle fall velocity of the ith grain-size class
Ri	Bulk Richardson number
$Re_{\mathrm{p}i}$	Particle Reynolds number of the ith grain-size class

r_{o}	Ratio of near-bed suspended sediment concentration to the layer-averaged concentration of suspended sediment
s	Sample standard deviation
t	Time
T_{d}	Flow duration
U	Layer-averaged flow velocity
u_*	Shear velocity
ν_{t}	Horizontal eddy viscosity
w_i	Settling velocity of a sediment particle of the ith grain-size class
x	Streamwise distance
κ	Parameter related to artificial viscosity
λ_{p}	Porosity of bed sediment
μ	Dynamic viscosity of water
ν	Kinematic viscosity of water
ρ	Density of water
θ	Angle of inclination of the base slope

Acknowledgements

I would like to express my deepest gratitude to my supervisor, Dr. Hajime Naruse of the Kyoto University Earth and Planetary Sciences Department, for his invaluable guidance and continuous support throughout the course of my PhD study. His passion for research and unending curiosity inspired and motivated me during my time as a PhD student. His encouraging attitude toward my research interest supported me throughout my course of study.

I would also like to express my sincere gratitude to Dr. Takao Ubukata and Dr. Hiroshige Matsuoka of the Kyoto University Earth and Planetary Sciences Department for their insightful comments and constructive criticism of my research throughout my time as a PhD student. Their questions toward my research had been essential in widening my perspective and prompting me to expand my repertoire of knowledge.

My gratitude must also go to Dr. Yoshiro Ishihara of the Fukuoka University Department of Earth System Science, who provided most of the outcrop datasets from the Anno Formation used in this research and guided me on the Anno Formation geological background aspect of my research. I would also like to thank Yasutaka Katafuchi, a former student of Dr. Yoshiro Ishihara, for conducting field work of the Anno Formation and performing the sampling and measurements for part of the samples used in this study.

In addition, I would like to acknowledge and express my gratitude to Dr. Kazuki Kikuchi, Postdoctoral Researcher of the Kyoto University Earth and Planetary Sciences Department and Dr. Yuichi Sakai of the Utsunomiya University Department of Forest Science for their inspiring advice during various early stages of this research. The stimulating

discussions I had with them were essential in shaping my idea.

I deeply appreciate the help of Harisma Buburanda, Takumi Nagato, Riko Seoka, PhD students of Earth and Planetary Sciences Department, for their support during the writing of this thesis. I would like to thank my labmates and friends Christina Shears-Ozeki and Haruna Furui for always being a warm presence and being supportive throughout my course of study as a PhD student.

My acknowledgment also goes to the members of the Biospehre Seminar for asking challenging questions that helped me sharpen my thoughts and for their help along the way of my PhD studies.

Finally, I would like to thank my family and friends for their unwavering support and tremendous understanding during my time as a PhD student. Your love and encouragement were indispensable for my mental and physical wellbeing.

Bibliography

Abad, J. D., G. Parker, O. Sequeiros, B. Spinewine, M. Garcia, and C. Pirmez (2010), Flow Structure in Submarine Meandering Channels Created by Turbidity Currents, *Mecánica Computacional*, *29*(83), 8165–8165.

Abadi, M., A. Agarwal, P. Barham, E. Brevdo, Z. Chen, C. Citro, G. S. Corrado, A. Davis, J. Dean, M. Devin, S. Ghemawat, I. Goodfellow, A. Harp, G. Irving, M. Isard, Y. Jia, R. Jozefowicz, L. Kaiser, M. Kudlur, J. Levenberg, D. Mané, R. Monga, S. Moore, D. Murray, C. Olah, M. Schuster, J. Shlens, B. Steiner, I. Sutskever, K. Talwar, P. Tucker, V. Vanhoucke, V. Vasudevan, F. Viégas, O. Vinyals, P. Warden, M. Wattenberg, M. Wicke, Y. Yu, and X. Zheng (2015), TensorFlow: Large-scale machine learning on heterogeneous systems, software available from tensorflow.org.

Altinakar, M., W. Graf, and E. Hopfinger (1996), Flow structure in turbidity currents, *Journal of Hydraulic Research*, *34*(5), 713–718, doi:10.1080/00221689609498467.

Arai, K., H. Naruse, R. Miura, K. Kawamura, R. Hino, Y. Ito, D. Inazu, M. Yokokawa, N. Izumi, M. Murayama, and T. Kasaya (2013), Tsunami-generated turbidity current of the 2011 Tohoku-Oki earthquake, *Geology*, *41*(11), 1195–1198.

Azpiroz-Zabala, M., M. J. B. Cartigny, P. J. Talling, D. R. Parsons, E. J. Sumner, M. A. Clare, S. M. Simmons, C. Cooper, and E. L. Pope (2017a), Newly recognized turbidity current structure can explain prolonged flushing of submarine canyons, *Science Advances*, *3*(10), doi:10.1126/sciadv.1700200.

Azpiroz-Zabala, M., M. J. B. Cartigny, P. J. Talling, D. R. Parsons, E. J. Sumner, M. A. Clare, S. M. Simmons, C. Cooper, and E. L. Pope (2017b), Newly recognized turbidity current structure can explain prolonged flushing of submarine canyons, *Science Advances*, *3*(10), e1700,200, doi:10.1126/sciadv.1700200.

Baas, J. H., R. L. Van Dam, and J. E. A. Storms (2000), Duration of deposition from decelerating high-density turbidity currents, *Sedimentary Geology*, *136*(1), 71–88.

Bagnold, R. A. (1954), Experiments on a gravity-free dispersion of large solid spheres in a Newtonian fluid under shear, *Proceedings of the Royal Society of London. Series A. Mathematical and Physical Sciences*, *225*(1160), 49–63, doi:10.1098/rspa.1954.0186.

Biegert, E., B. Vowinckel, R. Ouillon, and E. Meiburg (2017), High-resolution simulations of turbidity currents, *Progress in Earth and Planetary Science*, *4*(1), 33.

Bottou, L. (2010), Large-scale machine learning with stochastic gradient descent, in *Proceedings of COMPSTAT'2010*, edited by Y. Lechevallier and G. Saporta, pp. 177–186, Physica-Verlag HD, Heidelberg.

Bouma, A. H. (1962), *Sedimentology of Some Flysch Deposits: A Graphic Approach to Facies Interpretation*, 168 pp., Elsevier.

Cai, Z., and H. Naruse (2021), Inverse analysis of experimental scale turbidity currents using deep learning neural networks, *Journal of Geophysical Research: Earth Surface*, *126*(8), e2021JF006,276, doi:https://doi.org/10.1029/2021JF006276.

Cantero, M. I., S. Balachandar, and M. H. Garcia (2007), High-resolution simulations of cylindrical density currents, *Journal of Fluid Mechanics*, *590*, 437–469.

Cantero, M. I., S. Balachandar, A. Cantelli, C. Pirmez, and G. Parker (2009), Turbidity current with a roof: Direct numerical simulation of self-stratified turbulent channel flow driven by suspended sediment, *Journal of Geophysical Research: Oceans*, *114*(C3).

Chikita, K. (1989), A field study on turbidity currents initiated from spring runoffs, *Water Resources Research*, *25*(2), 257–271, doi:10.1029/WR025i002p00257.

Choi, S.-U. (1999), Layer-averaged modeling of two-dimensional turbidity currents with a dissipative-Galerkin finite element method Part II: Sensitivity analysis and experimental verification, *Journal of Hydraulic Research*, *37*(2), 257–271.

Choi, S.-U., and M. H. Garcia (1995), Modeling of one-dimensional turbidity currents with a dissipative-Galerkin finite element method, *Journal of Hydraulic Research*, *33*(5), 623–648.

Cooper, C., J. Wood, J. Imran, A. Islam, P. Wright, R. Faria, A. Tati, Z. Casey, and R. T. Casey (2016), Designing for Turbidity Currents in the Congo Canyon, Paper presented at the Offshore Technology Conference, Houston, Texas, USA, doi:10.4043/26919-MS.

Daly, R. A. (1936), Origin of submarine canyons, *American Journal of Science*, *31*(186), 401–420.

Davison, A. C., and D. V. Hinkley (1997), *Bootstrap Methods and their Application*, Cambridge University Press, doi:10.1017/CBO9780511802843.

de Leeuw, J., J. T. Eggenhuisen, and M. J. B. Cartigny (2016), Morphodynamics of submarine channel inception revealed by new experimental approach, *Nature Communications*, *7*(1), 10,886.

DeMets, C., R. G. Gordon, and D. F. Argus (2010), Geologically current plate motions, *Geophysical Journal International*, *181*(1), 1–80.

Dietrich, W. E. (1982), Settling velocity of natural particles, *Water Resources Research*, *18*(6), 1615–1626, doi:10.1029/WR018i006p01615.

Dorrell, R., and A. J. Hogg (2010), Sedimentation of bidisperse suspensions, *International Journal of Multiphase Flow*, *36*(6), 481–490.

Dorrell, R. M., A. J. Hogg, E. J. Sumner, and P. J. Talling (2011), The structure of the deposit produced by sedimentation of polydisperse suspensions, *Journal of Geophysical Research: Earth Surface*, *116*(F1).

Dorrell, R. M., S. E. Darby, J. Peakall, E. J. Sumner, D. R. Parsons, and R. B. Wynn (2014), The critical role of stratification in submarine channels: Implications for channelization and long runout of flows, *Journal of Geophysical Research: Oceans*, *119*(4), 2620–2641, doi:10.1002/2014JC009807.

Dorrell, R. M., J. Peakall, E. J. Sumner, D. R. Parsons, S. E. Darby, R. B. Wynn, E. Özsoy, and D. Tezcan (2016), Flow dynamics and mixing processes in hydraulic jump arrays: Implications for channel-lobe transition zones, *Marine Geology*, *381*, 181–193, doi: https://doi.org/10.1016/j.margeo.2016.09.009.

Dorrell, R. M., L. A. Amy, J. Peakall, and W. D. McCaffrey (2018), Particle size distribution controls the threshold between net sediment erosion and deposition in suspended load dominated flows, *Geophysical Research Letters*, *45*(3), 1443–1452.

Einstein, H. A., and R. B. Krone (1962), Experiments to determine modes of cohesive sediment transport in salt water, *Journal of Geophysical Research (1896-1977)*, *67*(4), 1451–1461.

Falcini, F., M. Marini, S. Milli, and M. Moscatelli (2009), An inverse problem to infer paleoflow conditions from turbidites, *Journal of Geophysical Research: Oceans*, *114*.

Fildani, A., W. R. Normark, S. Kostic, and G. Parker (2006), Channel formation by flow stripping: large-scale scour features along the Monterey East Channel and their relation to sediment waves, *Sedimentology*, *53*(6), 1265–1287.

Fukushima, Y., G. Parker, and H. M. Pantin (1985), Prediction of ignitive turbidity currents in Scripps submarine canyon, *Marine Geology*, *67*(1), 55–81.

Garcia, M., and G. Parker (1989), Experiments on Hydraulic Jumps in Turbidity Currents Near a Canyon-Fan Transition, *Science*, *245*(4916), 393–396.

Garcia, M., and G. Parker (1991), Entrainment of bed sediment into suspension, *Journal of Hydraulic Engineering*, *117*(4), 414–435.

Garcia, M., and G. Parker (1993), Experiments on the entrainment of sediment into suspension by a dense bottom current, *Journal of Geophysical Research*, *98*(C3), 4793–4807.

García, M. H. (1993), Hydraulic jumps in sedimen-driven bottom currents, *Journal of Hydraulic Engineering*, *119*(10), 1094–1117.

Gibbs, R. J. (1974), A settling tube system for sand-size analysis, *Journal of Sedimentary Petrology*, *44*(2), 583–588.

Gilbert, G. K. (1914), The transportation of debris by running water, *U.S. Geological Survey, Professional Paper*, *86*.

Goldfinger, C., C. Hans Nelson, and J. Johnson (2003), Deep-water turbidites as Holocene earthquake proxies: the Cascadia subduction zone and Northern San Andreas Fault systems, *Annals of Geophysics*, *46*(5).

Gunawan, H. P. (2015), Numerical simulation of shallow water equations and related models, Theses, Université Paris-Est.

Heerema, C. J., P. J. Talling, M. J. Cartigny, C. K. Paull, L. Bailey, S. M. Simmons, D. R. Parsons, M. A. Clare, R. Gwiazda, E. Lundsten, K. Anderson, K. L. Maier, J. P. Xu, E. J. Sumner, K. Rosenberger, J. Gales, M. McGann, L. Carter, and E. Pope (2020), What determines the downstream evolution of turbidity currents?, *Earth and Planetary Science Letters*, *532*, 116,023.

Hiscott, R. N. (1994), Loss of capacity, not competence, as the fundamental process governing deposition from turbidity currents, *Journal of Sedimentary Research*, *64*(2a), 209–214, doi:10.2110/jsr.64.209.

Huppert, H. E. (1998), Quantitative modelling of granular suspension flows, *Philosophical Transactions of the Royal Society of London. Series A: Mathematical, Physical and Engineering Sciences*, *356*, 2471–2496.

Ikehara, K., T. Kanamatsu, Y. Nagahashi, M. Strasser, H. Fink, K. Usami, T. Irino, and G. Wefer (2016), Documenting large earthquakes similar to the 2011 Tohoku-oki earthquake from sediments deposited in the Japan Trench over the past 1500 years, *Earth and Planetary Science Letters*, *445*, 48–56, doi:https://doi.org/10.1016/j.epsl.2016.04.009.

Imran, J., G. Parker, and P. Harff (2002), Experiments on incipient channelization of submarine fans, *Journal of Hydraulic Research*, *40*(1), 21–32.

Ishihara, Y., and S. Tokuhashi (2001), The geology of the area in and around the Seiwa Prefectural Forest Park, Chiba Prefecture, central Japan, with special reference to the stratigraphy and structure of the Kiyosumi and Anno formations, Neogene Awa Group (in Japanese), *Bulletin of the Geological Survey of Japan*, *52*(9), 383–404, doi:10.9795/bullgsj.52.383.

Ishihara, Y., and S. Tokuhashi (2005), Depositional process of the Pliocene Anno Formation, the uppermost part of the Awa Group, Boso Peninsula, central Japan-A case study on a turbidite depositional system of a forearc-basin filling- (in Japanese), *The Journal of the Geological Society of Japan*, *111*(5), 269–285, doi:10.5575/geosoc.111.269.

Jameson, A., W. Schmidt, and E. Turkel (1981), Numerical solution of the Euler equations by finite volume methods using Runge Kutta time stepping schemes, in *14th Fluid and Plasma Dynamics Conference*, American Institute of Aeronautics and Astronautics, doi:10.2514/6.1981-1259.

Johnson, D. W. (1939), *The Origin of Submarine Canyons: A Critical Review of Hypotheses*, 126 pp., Columbia University Press.

Keevil, G. M., J. Peakall, J. L. Best, and K. J. Amos (2006), Flow structure in sinuous submarine channels: Velocity and turbulence structure of an experimental submarine channel, *Marine Geology*, *229*(3), 241–257.

Kioka, A., T. Schwestermann, J. Moernaut, K. Ikehara, T. Kanamatsu, T. I. Eglinton, and M. Strasser (2019), Event Stratigraphy in a Hadal Oceanic Trench: The Japan Trench as Sedimentary Archive Recording Recurrent Giant Subduction Zone Earthquakes and Their Role in Organic Carbon Export to the Deep Sea, *Frontiers in Earth Science*, *7*, doi:10.3389/feart.2019.00319.

Kneller, B., M. M. Nasr-Azadani, S. Radhakrishnan, and E. Meiburg (2016), Long-range sediment transport in the world's oceans by stably stratified turbidity currents, *Journal of Geophysical Research: Oceans*, *121*(12), 8608–8620.

Komar, P. D., and Z. Li (1986), Pivoting analyses of the selective entrainment of sediments by shape and size with application to gravel threshold, *Sedimentology*, *33*(3), 425–436.

Konsoer, K., J. Zinger, and G. Parker (2013), Bankfull hydraulic geometry of submarine channels created by turbidity currents: Relations between bankfull channel characteristics and formative flow discharge, *Journal of Geophysical Research: Earth Surface*, *118*(1), 216–228.

Kostic, S., and G. Parker (2006), The response of turbidity currents to a canyon–fan transition: Internal hydraulic jumps and depositional signatures, *Journal of Hydraulic Research*, *44*(5), 631–653, doi:10.1080/00221686.2006.9521713.

Krizhevsky, A., I. Sutskever, and G. E. Hinton (2012), Imagenet classification with deep convolutional neural networks, in *Advances in Neural Information Processing Systems*

25, edited by F. Pereira, C. J. C. Burges, L. Bottou, and K. Q. Weinberger, pp. 1097–1105, Curran Associates, Inc.

Kubo, Y., F. Masuda, S. Tokuhashi, and T. Sakai (1998), Spatial variation in paleocurrent velocities estimated from a turbidite bed of the Mio-Pliocene Kiyosumi Formation in Boso Peninsula, Japan, *The Journal of the Geological Society of Japan*, *104*(6), 359–364, doi:10.5575/geosoc.104.359.

Kuenen, P. H. (1966), Experimental turbidite lamination in a circular flume, *The Journal of Geology*, *74*(5), 523–545.

Kuenen, P. H., and H. W. Menard (1952), Turbidity currents, graded and non-graded deposits, *Journal of Sedimentary Research*, *22*(2), 83–96, doi:10.1306/D42694CC-2B26-11D7-8648000102C1865D.

Kuenen, P. H., and C. I. Migliorini (1950), Turbidity currents as a cause of graded bedding, *The Journal of Geology*, *58*(2), 91–127.

Lai, Y. G., J. Huang, and K. Wu (2015), Reservoir Turbidity Current Modeling with a Two-Dimensional Layer-Averaged Model, *Journal of Hydraulic Engineering*, *141*(12), 04015,029.

Laval, A., M. Cremer, P. Beghin, and C. Ravenne (1988), Density surges: two-dimensional experiments, *Sedimentology*, *35*(1), 73–84.

Lesshafft, L., E. Meiburg, B. Kneller, and A. Marsden (2011), Towards inverse modeling of turbidity currents: The inverse lock-exchange problem, *Computers and Geosciences*, *37*(4), 521–529, doi:https://doi.org/10.1016/j.cageo.2010.09.015.

Liang, S., and R. Srikant (2016), Why deep neural networks for function approximation?, *CoRR*, *abs/1610.04161*.

Lüthi, S. (1981), Some new aspects of two-dimensional turbidity currents*, *Sedimentology*, *28*(1), 97–105.

McIntosh, A. (2016), The jackknife estimation method.

Meiburg, E., S. Radhakrishnan, and M. Nasr-Azadani (2015), Modeling Gravity and Turbidity Currents: Computational Approaches and Challenges, *Applied Mechanics Reviews*, *67*(4), doi:10.1115/1.4031040.

Middleton, G. V. (1966a), Experiments on Density and Turbidity Currents: I. Motion of the Head, *Canadian Journal of Earth Sciences*, *3*(4), 523–546, doi:10.1139/e66-038.

Middleton, G. V. (1966b), Experiments on Density and Turbidity Currents: II. Uniform Flow and Density Currents, *Canadian Journal of Earth Sciences*, *3*(5), 627–637, doi:10.1139/e66-044.

Minoura, K., and S. Nakaya (1991), Traces of Tsunami Preserved in Inter-Tidal Lacustrine and Marsh Deposits: Some Examples from Northeast Japan, *The Journal of Geology*, *99*(2), 265–287, doi:10.1086/629488.

Miramontes, E., J. T. Eggenhuisen, R. S. Jacinto, G. Poneti, F. Pohl, A. Normandeau, D. C. Campbell, and F. J. Hernández-Molina (2020), Channel-levee evolution in combined contour current-turbidity current flows from flume-tank experiments, *Geology*, *48*(4), 353–357.

Mitra, R., H. Naruse, and T. Abe (2020), Estimation of tsunami characteristics from deposits: Inverse modeling using a deep-learning neural network, *Journal of Geophysical Research: Earth Surface*, *125*(9), e2020JF005,583.

Mitra, R., H. Naruse, and S. Fujino (2021), Reconstruction of flow conditions from 2004 Indian Ocean tsunami deposits at the Phra Thong island using a deep neural network inverse model, *Natural Hazards and Earth System Sciences*, *21*(5), 1667–1683.

Nakao, K., H. Naruse, and S. Tokuhashi (2020), Inverse analysis to reconstruct hydraulic conditions of non-steady turbidity currents: Application to an ancient turbidite of the Kiyosumi Formation of the Awa Group, Boso Peninsula, central Japan, *EarthArXiv*.

Naruse, H. (2005), Usage and advantages of an application program "STube" for settling tube grain-size analysis (in Japanese), *Journal of the Sedimentological Society of Japan*, *62*(62), 55–61.

Naruse, H. (2019), Inverse modeling of turbidity currents using 2d shallow-water model and neural network toward understanding of development processes of submarine fans, in *2019 AGU Fall Meeting*.

Naruse, H., and K. Nakao (2021), Inverse modeling of turbidity currents using an artificial neural network approach: verification for field application, *Earth Surface Dynamics*, *9*(5), 1091–1109, doi:10.5194/esurf-9-1091-2021.

Naruse, H., and C. Olariu (2008), Hydraulic conditions of turbidity currents estimated by inverse analysis (in Japanese), in *Fourth International Conference on Scour and Erosion*, pp. 591–593, Japanese Geotechnical Society.

Nielsen, M. A. (2015), *Neural Networks and Deep Learning*, 216 pp., Determination Press.

Ogata, Y., and T. Yabe (1999), Shock capturing with improved numerical viscosity in primitive Euler representation, *Computer Physics Communications*, *119*(2), 179–193, doi: https://doi.org/10.1016/S0010-4655(99)00188-5.

Oguri, K., K. Kawamura, A. Sakaguchi, T. Toyofuku, T. Kasaya, M. Murayama, K. Fujikura, R. N. Glud, and H. Kitazato (2013), Hadal disturbance in the Japan Trench induced by the 2011 Tohoku-Oki Earthquake, *Scientific Reports*, *3*(1), 1915, doi: 10.1038/srep01915.

Parker, G., Y. Fukushima, and H. M. Pantin (1986), Self-accelerating turbidity currents, *Journal of Fluid Mechanics*, *171*, 145–181, doi:10.1017/S0022112086001404.

Parker, G., M. Garcia, Y. Fukushima, and W. Yu (1987), Experiments on turbidity currents over an erodible bed, *Journal of Hydraulic Research*, *25*(1), 123–147.

Parkinson, S. D., S. W. Funke, J. Hill, M. D. Piggott, and P. A. Allison (2017), Application of the adjoint approach to optimise the initial conditions of a turbidity current with the AdjointTurbidity 1.0 model, *Geoscientific Model Development*, *10*(3), 1051–1068.

Paull, C. K., P. J. Talling, K. L. Maier, D. Parsons, J. Xu, D. W. Caress, R. Gwiazda, E. M. Lundsten, K. Anderson, J. P. Barry, M. Chaffey, T. O'Reilly, K. J. Rosenberger, J. A. Gales, B. Kieft, M. McGann, S. M. Simmons, M. McCann, E. J. Sumner, M. A. Clare, and M. J. Cartigny (2018), Powerful turbidity currents driven by dense basal layers, *Nature Communications*, *9*(1), 4114.

Piper, D. J. W., A. N. Shor, and J. E. Hughes Clarke (1988), The 1929 "Grand Banks" earthquake, slump, and turbidity current, in *Sedimentologic Consequences of Convulsive Geologic Events*, Geological Society of America, doi:10.1130/SPE229-p77.

Pirmez, C., and J. Imran (2003), Reconstruction of turbidity currents in amazon channel, *Marine and Petroleum Geology*, *20*(6), 823–849, turbidites: Models and Problems.

Pradhan, B., S. Lee, and M. F. Buchroithner (2010), A GIS-based back-propagation neural network model and its cross-application and validation for landslide susceptibility analyses, *Computers, Environment and Urban Systems*, *34*(3), 216–235.

Riddell, J. F. (1969), A laboratory study of suspension-effect density currents, *Canadian Journal of Earth Sciences*, *6*(2), 231–246, doi:10.1139/e69-022.

Rogers, S. J., J. H. Fang, C. L. Karr, and D. A. Stanley (1992), Determination of lithology from well logs using a neural network, *AAPG Bulletin*, *76*(5), 731–739.

Rowland, J. C., G. E. Hilley, and A. Fildani (2010), A Test of Initiation of Submarine Leveed Channels by Deposition Alone, *Journal of Sedimentary Research*, *80*(8), 710–727.

Ruder, S. (2016), An overview of gradient descent optimization algorithms, *CoRR*, *abs/1609.04747*.

Rumble, J. R. (2018), *CRC Handbook of Chemistry and Physics, 99th Edition*, 1550 pp., CRC Press.

Saito, S. (1991), Relationship between Subduction Styles and Morphology of Forearc Basins (in Japanese), *Journal of Geography*, *100*(4), 616–627.

Sawai, Y., Y. Namegaya, Y. Okamura, K. Satake, and M. Shishikura (2012), Challenges of anticipating the 2011 Tohoku earthquake and tsunami using coastal geology, *Geophysical Research Letters*, *39*(21).

Schmidhuber, J. (2015), Deep learning in neural networks: An overview, *Neural Networks*, *61*, 85–117, doi:https://doi.org/10.1016/j.neunet.2014.09.003.

Sequeiros, O. E., H. Naruse, N. Endo, M. H. Garcia, and G. Parker (2009), Experimental study on self-accelerating turbidity currents, *Journal of Geophysical Research: Oceans*, *114*(C5).

Sequeiros, O. E., B. Spinewine, R. T. Beaubouef, T. Sun, M. H. García, and G. Parker (2010), Characteristics of velocity and excess density profiles of saline underflows and turbidity currents flowing over a mobile bed, *Journal of Hydraulic Engineering*, *136*(7), 412–433, doi:10.1061/(ASCE)HY.1943-7900.0000200.

Simmons, S. M., M. Azpiroz-Zabala, M. J. B. Cartigny, M. A. Clare, C. Cooper, D. R. Parsons, E. L. Pope, E. J. Sumner, and P. J. Talling (2020), Novel acoustic method provides first detailed measurements of sediment concentration structure within submarine

turbidity currents, *Journal of Geophysical Research: Oceans*, *125*(5), e2019JC015,904, doi:10.1029/2019JC015904.

Strasser, M. (2017), Japan Trench Paleoseismology, IODP Proposal.

Straub, K. M., D. Mohrig, B. McElroy, J. Buttles, and C. Pirmez (2008), Interactions between turbidity currents and topography in aggrading sinuous submarine channels: A laboratory study, *GSA Bulletin*, *120*(3-4), 368–385.

Talling, P. J., L. A. Amy, and R. B. Wynn (2007), New insight into the evolution of large-volume turbidity currents: Comparison of turbidite shape and previous modelling results, *Sedimentology*, *54*(4), 737–769.

Talling, P. J., D. G. Masson, E. J. Sumner, and G. Malgesini (2012), Subaqueous sediment density flows: Depositional processes and deposit types, *Sedimentology*, *59*(7), 1937–2003.

Talling, P. J., C. K. Paull, and D. J. Piper (2013), How are subaqueous sediment density flows triggered, what is their internal structure and how does it evolve? Direct observations from monitoring of active flows, *Earth-Science Reviews*, *125*, 244–287.

Talling, P. J., J. Allin, D. A. Armitage, R. W. C. Arnott, M. J. B. Cartigny, M. A. Clare, F. Felletti, J. A. Covault, S. Girardclos, E. Hansen, P. R. Hill, R. N. Hiscott, A. J. Hogg, J. H. Clarke, Z. R. Jobe, G. Malgesini, A. Mozzato, H. Naruse, S. Parkinson, F. J. Peel, D. J. W. Piper, E. Pope, G. Postma, P. Rowley, A. Sguazzini, C. J. Stevenson, E. J. Sumner, Z. Sylvester, C. Watts, and J. Xu (2015), Key future directions for research on turbidity currents and their deposits, *Journal of Sedimentary Research*, *85*(2), 153–169.

Tokuhashi, S. (1982), Tabidaito no hanashi (1) furisshugata sadeigosou no taipu to taiseki kannkyo (The story of turbidite (1) Classification and depositional environment of flysh

type interbedded sandstone and mudstone units) (in Japanese), *Chishitsu News*, *344*, 42–50.

Tokuhashi, S. (1988), Extent and Form of Individual Turbidite Sandstone Beds in Ancient Submarine Fan Sediments (in Japanese), *Sekiyu Gakkaishi*, *31*(1), 12–29, doi: 10.1627/jpi1958.31.12.

Tokuhashi, S., and T. Iwawaki (1975), Areal sedimentary analysis of flysch-type alternations, *Earth Science (Chikyu Kagaku)*, *29*(6), 262–274.

Tokuhashi, S., T. Danhara, and H. Iwano (2000), Fission track ages of eight tuffs in the upper part of the Awa Group, Boso Peninsula, central Japan (in Japanese), *The Journal of the Geological Society of Japan*, *106*(8), 560–573, doi:10.5575/geosoc.106.560.

Traer, M. M., A. Fildani, O. Fringer, T. McHargue, and G. E. Hilley (2018), Turbidity current dynamics: 1. model formulation and identification of flow equilibrium conditions resulting from flow stripping and overspill, *Journal of Geophysical Research: Earth Surface*, *123*(3), 501–519.

Usami, T. (1987), *Descriptive catalogue of disaster earthquakes in Japan rev. ed.*, University of Tokyo Press.

van Rijn, L. C. (1984a), Sediment Transport, Part I: Bed Load Transport, *Journal of Hydraulic Engineering*, *110*(10), 1431–1456.

van Rijn, L. C. (1984b), Sediment Transport, Part II: Suspended Load Transport, *Journal of Hydraulic Engineering*, *110*(11), 1613–1641.

Vangriesheim, A., A. Khripounoff, and P. Crassous (2009), Turbidity events observed in situ along the Congo submarine channel, *Deep Sea Research Part II: Topical Studies in Oceanography*, *56*(23), 2208–2222.

Vestbøstad, T. M., O. M. Faltinsen, D. Kristiansen, et al. (2007), Validation Methods and Benchmark Tests for a 2-D CIP Method Applied to Marine Hydrodynamics, in *The Seventeenth International Offshore and Polar Engineering Conference*, International Society of Offshore and Polar Engineers.

von Huene, R., and S. Lallemand (1990), Tectonic erosion along the Japan and Peru convergent margins, *GSA Bulletin*, *102*(6), 704–720.

Wang, Z., and A. C. Bovik (2009), Mean squared error: Love it or leave it? a new look at signal fidelity measures, *IEEE Signal Processing Magazine*, *26*(1), 98–117, doi: 10.1109/MSP.2008.930649.

Weimer, P., and R. M. Slatt (2007), Introduction to the petroleum geology of deepwater settings, *AAPG Studies in Geology*, *57*, 149–227.

Xu, J. P., M. A. Noble, and L. K. Rosenfeld (2004), In-situ measurements of velocity structure within turbidity currents, *Geophysical Research Letters*, *31*(9).

Yabe, T., and P.-Y. Wang (1991), Unified Numerical Procedure for Compressible and Incompressible Fluid, *Journal of the Physical Society of Japan*, *60*(7), 2105–2108, doi: 10.1143/JPSJ.60.2105.

Yabe, T., F. Xiao, and T. Utsumi (2001), The constrained interpolation profile method for multiphase analysis, *Journal of Computational Physics*, *169*(2), 556–593, doi: https://doi.org/10.1006/jcph.2000.6625.

Yang, H., M. Lu, and T. Kumakura (2016), A study on the water front in shallow water equations (in Japanese), *Journal of Japan Society of Civil Engineers, Ser. B1 Hyraulic Engineering*, *72*(4), I325–I330.

Yeh, T.-h., M. Cantero, A. Cantelli, C. Pirmez, and G. Parker (2013), Turbidity current with a roof: Success and failure of RANS modeling for turbidity currents under strongly

stratified conditions, *Journal of Geophysical Research: Earth Surface*, *118*(3), 1975–1998.